論文 / 著書情報
Article / Book Information

題目(和文)	鉛含有複合ペロブスカイトリラクサーにおける誘電応答の熱力学的研究
Title(English)	Thermodynamic signature of the dielectric response in lead-based complex perovskite relaxors
著者(和文)	守屋映祐
Author(English)	yousuke moriya
出典(和文)	学位:博士(理学), 学位授与機関:東京工業大学, 報告番号:甲第5330号, 授与年月日:2003年3月26日, 学位の種別:課程博士, 審査員:
Citation(English)	Degree:Doctor (Science), Conferring organization: Tokyo Institute of Technology, Report number:甲第5330号, Conferred date:2003/3/26, Degree Type:Course doctor, Examiner:
学位種別(和文)	博士論文
Type(English)	Doctoral Thesis

Doctoral Thesis

Thermodynamic Signature of the Dielectric Response in Lead-Based Complex Perovskite Relaxors

Yosuke Moriya

Department of Electronic Chemistry,
Interdisciplinary Graduate School of Science and Engineering,
Tokyo Institute of Technology

2003

Supervisor Professor Tooru Atake

Index

Chapter 1 Introduction

Chapter 2 Experimental Apparatuses and Techniques

Chapter 3 $BaTiO_3$, $PbTiO_3$, and $PbZrO_3$

Typical Perovskite Ferro- and Antiferroelectrics

—— Features in Their Heat Capacity

Chapter 1

Introduction

1.1. Lead-based Complex Perovskite Oxides

Perovskite, $CaTiO_3$ is one of the alkaline igneous rocks, which was found by Perovski, a Russian mineralogist in 19th century. Thenceforth, compounds with the perovskite structure (Fig. 1.1) have been conventionally called "perovskite compounds" or simply "perovskites". The general formula of perovskites is ABX_3, where in general, the *A*-site and the *B*-site are occupied by different kinds of metal cation, respectively, and the *X*-site is occupied by an anion such as oxygen or halogen. The *A*-site is coordinated by twelve *X*-sites, while the *B*-site is coordinated by six *X*-sites. Thus, the *A*-sites can accommodate cations with larger ionic radius relative to the *B*-sites. Since the *B*-site is located at the center of the *X*-site octahedron, it is often called "octahedral site". This structure ideally belongs to cubic symmetry (space group $Pm\bar{3}m$), and one unit cell contains one formula unit (ABX_3). In many cases, however, perovskites undergo a structural phase transition and transform into a lower symmetry phase with decreasing temperature. For example, the room temperature phase of $CaTiO_3$ is orthorhombic phase (*Pnma*).

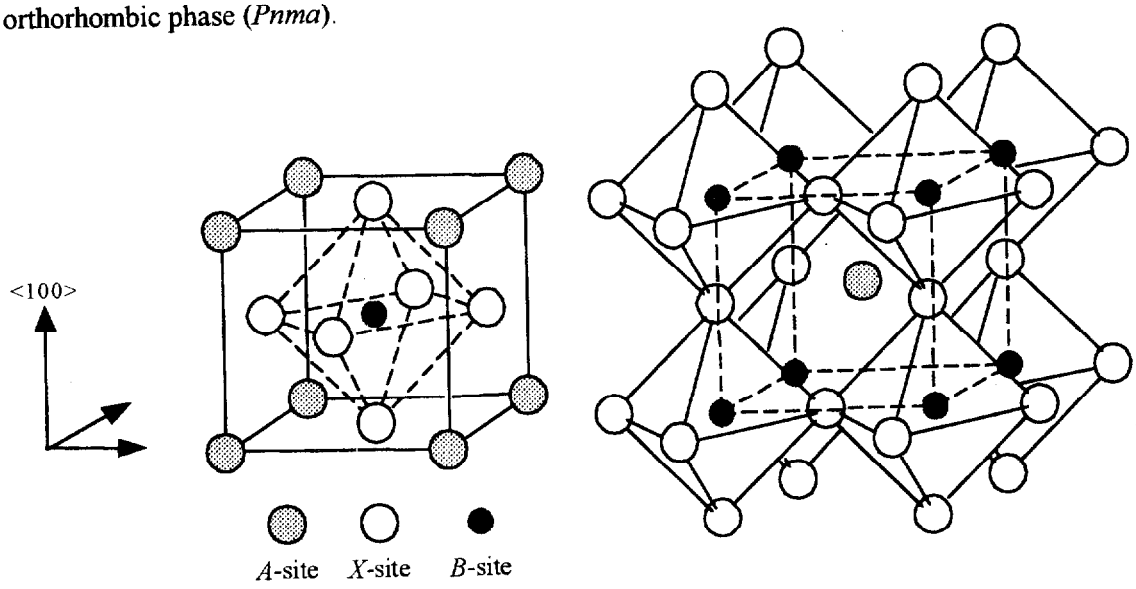

Fig.1.1. Perovskite structure. The left side shows the *B*-site centered, while the right side shows the *A*-site centered.

In many cases, the perovskite forms complex compounds, where crystallographically equivalent sites are occupied by a few kinds of metal cations with different valences and/or ionic radii. Such compounds are called "complex perovskites", and expressed by formulae such as $(A'A'')BX_3$, $A(B'B'')X_3$, and $(A'A'')(B'B'')X_3$ according to the number of ionic kinds at equivalent sites. In some complex perovskites, the ionic arrangement at equivalent sites can be ordered. For example, in $A(B'_{1/2}B''_{1/2})X_3$-type complex perovskites, 1:1 ordered arrangement of B' and B'' can be formed. In this case, it is convenient to consider alternate positions on the B-site sublattice, i.e., B^{I} and B^{II}-positions. These alternate positions form alternate layers, i.e., B^{I} and B^{II}-layers along $<111>_{cub}$ directions (the subscript 'cub' denotes indices referred to the cubic or pseudo-cubic lattice) (Fig.1.2).

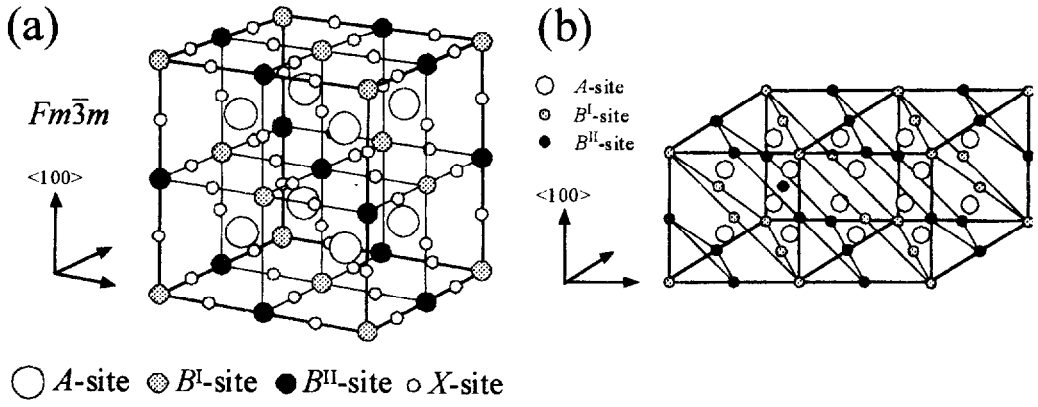

Fig. 1.2. Structure of the perovskite with 1:1 ordered arrangement on the B-site sublattice; (a) unit cell of space group $Fm\bar{3}m$, where each of the B^{I} and B^{II}-sites forms fcc structure, and the NaCl structure is realized on the B-site sublattice; (b) schematic illustration of the alternate B^{I} and B^{II}-layers along one of the four possible <111> direction, where the X-sites are omitted for clarity.

When the B^{I} and B^{II}-positions (or layers) are exclusively occupied by B' and B'' ions, respectively, the arrangement is completely ordered, i.e., the NaCl structure is realized on the B-site sublattice. Therefore, the unit cell is of the superstructure with the double period of the basic perovskite unit cell, and the space group $Pm\bar{3}m$ is replaced by $Fm\bar{3}m$. In the diffraction image, superlattice reflections caused by the unit cell doubling appear besides basic perovskite reflections. On the other hand, when the number of B' (B'') ions occupying the B^{I}-positions equals to that of B' (B'') ions occupying the B^{II}-positions, the arrangement is

disordered*. In this case, space group remains $Pm\bar{3}m$ and only basic reflections appear in a diffraction image. It should be noted that all of the complex perovskites do not always form an ordered arrangement. Depending on the ionic combination on an equivalent site, some are only disordered, some are only ordered, and others show an order-disorder phase transition on the ionic arrangement like *AB*-type alloys. As inferred from the fact that the perovskites form easily complex compounds, many perovskites can also form a solid solution (or mixed crystal) with each other. For example, $BaTiO_3$ is mixed with $BaSnO_3$ to be $(1\text{-}x)BaTiO_3\text{-}xBaSnO_3$, or $BaTi_{1-x}Sn_xO_3$, in the whole fraction range x = 0 to 1 **[1]**. As another example showing more complex mixing, there are solid solutions among complex perovskites like $(1\text{-}x)Pb(Mg_{1/3}Ta_{2/3})O_3\text{-}xPb(Sc_{1/2}Ta_{1/2})O_3$, where the *B*-site is occupied by three kinds of cation **[2]**. Including such complex and mixed perovskites, there have been a great number of perovskites so far.

Historically, the first perovskite attracting much attention is surely barium titanate, $BaTiO_3$, which was synthesized artificially as a derivative of $CaTiO_3$. The ferroelectricity of $BaTiO_3$ was discovered separately in three countries, namely Japan, U.S.A. and former U.S.S.R. at nearly the same time around 1945 in World War II. Thenceforth, perovskite oxides with high performance as a dielectric material, i.e., high dielectric constant and low dielectric loss, have been investigated meeting the demands for many technological applications, mainly a capacitor for communications. In such a situation, new perovskite and related oxides have been synthesized one after another, and some perovskite oxides have been found to show unique magnetic properties, electronic and ionic conductivity, and superconductivity, besides ferroelectricity and unique dielectric properties. Nowadays, in every field of solid state physics and chemistry, perovskites are studied quite extensively because it is easier to study by modeling owing to the simple crystal structure of the perovskite.

The $ATiO_3$-type perovskites are a group of perovskite dielectrics that have been studied quite extensively. In this group, $BaTiO_3$, $PbTiO_3$, and $CdTiO_3$ are ferroelectrics, while $CaTiO_3$ and $SrTiO_3$ are quantum paraelectrics, and the dielectric property is effectively changed by the substitution of an *A*-site cation. It is considered that such a change in the dielectric property is mainly caused by the difference in ionic radius of an *A*-site cation, and so the tolerance factor **[3]** is often referred to when the dielectric property of a new perovskite is predicted. On the other hand, ionic mass also strongly affects dielectric properties. For example, recently, it has been reported that the substitution of ^{16}O in $SrTiO_3$ by ^{18}O induced ferroelectricity in quantum

* Although the term "completely disordered" is often used in some papers related to order-disorder phase transition, this is a thermodynamically wrong expression. According to the concept of order-disorder phase transition, the state without order, namely degree of ordering $\sigma = 0$, can be called "disordered" state and all of the other states with non-zero σ are "ordered" states even if the ordering is incomplete. Since σ ranges from 0 to 1, the state with $0 < \sigma < 1$ is "partially ordered" state and the state with $\sigma = 1$ is "completely ordered" state, which can be realized only at 0 K according to the third law of thermodynamics.

paraelectric $SrTiO_3$ [4]. Only in the ferroelectrics of this group, there are interesting differences among them. $BaTiO_3$ shows successive phase transitions and the crystal changes from cubic paraelectric phase ($Pm\bar{3}m$) into tetragonal ($P4mm$), orthorhombic ($Bmm2$), and rhombohedral ($R3m$) ferroelectric phases successively at about 400, 300, and 200 K, respectively, while $PbTiO_3$ does not show successive phase transitions although it shows a ferroelectric phase transition from cubic paraelectric phase ($Pm\bar{3}m$) into tetragonal ferroelectric phase ($P4mm$) at around 760 K on cooling (these phase transition points can not be determined definitely because all of these phase transitions are of first-order). Such a difference in the phase transition behavior is predicted by first-principles calculations to be caused by the difference in covalency between Ba-O and Pb-O [5]. Recently, this prediction has been experimentally confirmed by charge-density distributions of both perovskites obtained by the MEM (maximum entropy method) using synchrotron-radiation powder diffraction data [6]. In addition, the particle size effect on the phase transition behavior has been also investigated in these conventional perovskite ferroelectrics [7]. Like this, $ATiO_3$-type perovskites are still subjects of scientific interests, and differences in the dielectric property and phase transition behavior among them are widely studied even at present.

Lead-based perovskites, $PbBO_3$ are also a very interesting group of dielectric perovskites because the dielectric property is also changed by substitution of the B-site ion, like $ATiO_3$-type perovskites. In this group, there are two representatives; one is lead titanate, $PbTiO_3$ (PT) and the other is lead zirconate, $PbZrO_3$ (PZ). PT is a typical perovskite ferroelectric material with the ferroelectric transition point at around 760 K as mentioned above. And PZ is the first-discovered antiferroelectric material with an antiferroelectric phase transition point at about 500 K [8], and the high and low temperature phases are cubic paraelectric ($Pm\bar{3}m$) and orthorhombic antiferroelectric ($Pbam$) phases, respectively. Since the antiferroelectricity was discovered in PZ, the phase transition behavior has been extensively studied by many researchers [9-13]. Early studies using a ceramic sample revealed the existence of an intermediate phase in a very narrow temperature range, which was confirmed later to be a rhombohedral ferroelectric phase [8]. In a representative case [12], this intermediate phase appears from 503 to 506 K on heating and from 505 to 500 K on cooling. However, most of these studies mentioned that the intermediate phase is strongly affected by small quantities of impurities: it was stabilized by the presence of Ba or Ti [9], and suppressed by a small quantity of Ca impurity [11]. All of early studies were performed on ceramic samples, and later studies employing single crystal samples [13] revealed that the intermediate phase was also strongly affected by flux used for the synthesis. In the case of PbO-PbF_2 flux, the intermediate phase was not observed and the antiferroelectric transition point was shifted down by about 20 K. On the other hand, in the case of PbO flux, the intermediate phase was clearly observed, and it

became clearer by using higher-purity PbO. Thus it is considered that pure PZ shows three phases; cubic paraelectric, rhombohedral ferroelectric, and orthorhombic antiferroelectric phases. However, the intermediate phase is very sensitive to small quantities of impurities, and the existence of the intermediate phase in PZ is still in controversy. These two representatives are also very important as both end members of lead zirconate titanate solid solution system, $PbZr_{1-x}Ti_xO_3$ (PZT) that is one of the indispensable applied dielectric materials. PZT has been applied quite widely to a transducer, actuator, infrared detector, and so on, using its remarkable piezo- and pyroelectricity. In addition, recently, PZT is expected to be nonvolatile memory, i.e., ferroelectric random-access memory **[14]**, as well as bismuth-layered perovskite compounds, $SrBi_2(Ta_{1-x}Nb_x)_2O_9$ **[15]**, and the applied researches for PZT thin films are becoming active. Scientifically, the detailed phase diagram of PZT has been investigated because PZT shows complex phase variation to be dependent on the fraction x. Besides PT and PZ, antiferroelectric $PbHfO_3$ is known as another lead-based perovskite oxide, but there are not so many lead-based perovskites with only one kind of a B-site cation, because the B-site cation is usually restricted to a four-valence cation according to the charge neutral condition except for the cases with the formation of defects or vacancies. However, including complex perovskites, there are a great number of lead-based perovskites because the averaged valence of B-site cations has only to be four so long as only the charge neutral condition is concerned, and there are a great number of such ionic combinations. When B-site cations are restricted to two kinds, $Pb(B'B'')O_3$ becomes $Pb(B'_{1/3}B''_{2/3})O_3$ with the combination of $B' = B^{2+}$ and $B'' = B^{5+}$, and $Pb(B'_{1/2}B''_{1/2})O_3$ with the combination of $B' = B^{3+}$ and $B'' = B^{5+}$, or $B' = B^{2+}$ and $B'' = B^{6+}$. Of course, lead-based complex perovskites are not always realized with all of such combinations because it is also necessary to take account of the tolerance factor concerning ionic radius in order to realize the perovskite structure. However, a large number of lead-based complex perovskite oxides have been actually synthesized, and their dielectric properties have been extensively investigated since the early 1950's by the research group of G. A. Smolenskii, a Russian scientist of A. F. Ioffe Physical Technical Institute in former Leningrad, U.S.S.R. (present St. Petersburg, Russia) **[16-18]**. Recently, their dielectric properties are abruptly attracting much attention. Some of them showed ferroelectricity, and some of them showed antiferroelectricity. However, strange compounds were found among them showing a quite new dielectric property that is neither normal ferroelectricity nor antiferroelectricity. At present, these compounds are called "relaxor ferroelectrics" or simply "relaxors".

1.2. Relaxor Ferroelectrics

It is said that the studies on relaxors originates from the studies on lead-based complex perovskite oxides started by Smolenskii's group. Nowadays, one of lead-based complex perovskite oxides is considered as a prototype of relaxors, i.e., lead magnesium niobate, $Pb(Mg_{1/3}Nb_{2/3})O_3$ (PMN). At the beginning, there was not the term of "relaxor" yet, and the terms of "ferroelectrics with a diffuse phase transition" **[19,20]** or "dirty ferroelectrics" **[21]** were mainly used for expressing relaxors. In fact, the definition of the relaxor itself has not been clearly provided so far, and it seems that a compound with similar dielectric behavior to PMN is called "relaxor" or "relaxor-like" compound. Thus, first, it is necessary to describe the dielectric properties of PMN in detail.

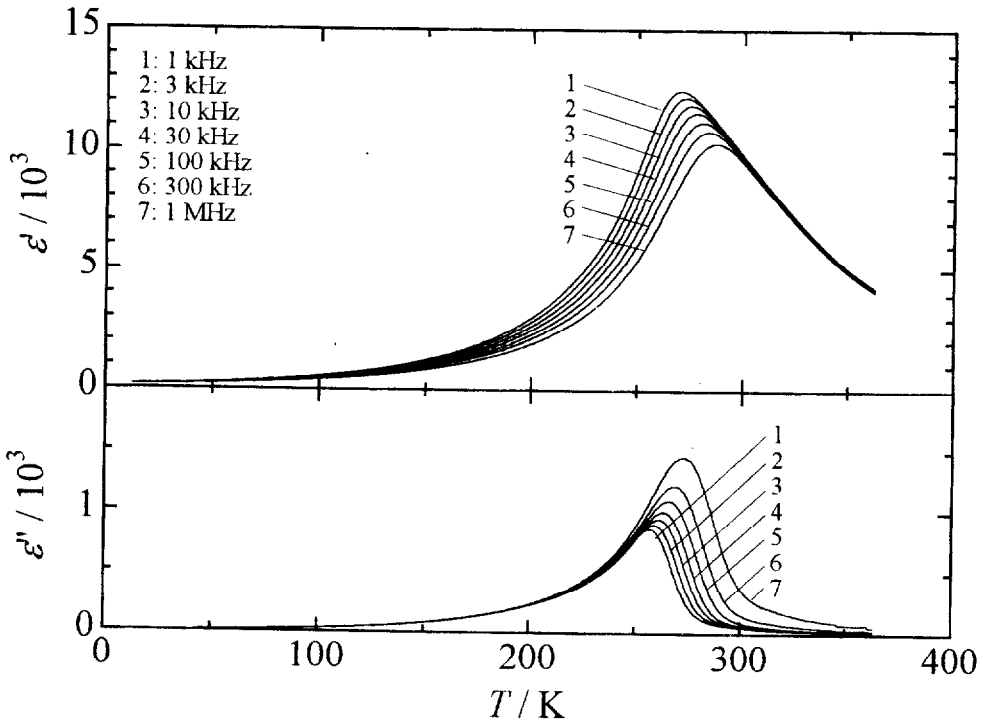

Fig. 1.3. Temperature- and frequency-dependence of the complex dielectric constant of typical relaxor ferroelectric $Pb(Mg_{1/3}Nb_{2/3})O_3$ (PMN).

The temperature- and frequency-dependence of the complex dielectric constant, namely dielectric constant ε' and dielectric loss ε'', of PMN is shown in Fig.1.3. In the temperature-dependence, the most remarkable feature is a very broad peak over a wide temperature range unlike a sharp peak observed at a ferroelectric or antiferroelectric phase transition point in usual (anti)ferroelectrics such as $BaTiO_3$. A peak in a dielectric constant

curve still reminds of the occurrence of a phase transition, and this phenomenon was called "diffuse phase transition". However, a phase transition as a macroscopic cooperative phenomenon does not occur in PMN. On the other hand, with increasing frequency, the maximum value of the dielectric constant decreases, while that of the dielectric loss increases, and the both maximums shift up to higher temperatures. Such characteristic dielectric dispersion is very similar to that observed in a glass former and some orientational glass models for PMN have been proposed **[22,23]**. These are the main features of PMN. As other features of lead-based perovskite relaxors such as PMN, the following features can be cited; a large maximum value of dielectric constant ($\sim 10^4$), a small dielectric loss tangent, the largest electro-mechano-coupling coefficient among piezoelectric crystals, and so on. In fact, most relaxors like PMN are not "ferroelectrics" to be exact, as a macroscopic spontaneous polarization is not observed in them. Nevertheless, these are called "relaxor ferroelectrics" because similar functional properties to ferroelectrics are observed to be superior to ferroelectrics.

It is said that "relaxor" was named by L. E. Cross **[24]** in the early 1980's after its characteristic dielectric relaxation. Thenceforth, a compound showing such temperature- and frequency-dependence of complex dielectric constant seem to be called relaxor even if a maximum value of dielectric constant is not so large. For example, in the case of an organic relaxor discovered recently **[25]**, the maximum value of dielectric constant is about 10^2. Since the discovery of relaxors in lead-based complex perovskites, similar dielectric behavior has been also found in La-modified PZT, $(Pb_{1-x}La_x)(Zr_{1-y}Ti_y)O_3$ (PLZT) **[24,26]**, and the compounds with the tungsten-bronze structure, $Sr_{1-x}Ba_xNb_2O_6$ (SBN) and $(Sr_{1-x}Ba_x)(Nb_{1-y}Ta_y)_2O_6$ (SBNT) **[24,27]**. Nowadays, these are considered as "typical" relaxors, and it is known that besides these compounds, similar dielectric behavior is found in Bi-doped $SrTiO_3$ **[28,29]**, Ce-doped $BaTiO_3$ **[28]**, organic system **[25,30,31]**, and so on. So long as such compounds are seen, it seems that most ferroelectrics can be a relaxor by doping or partial substitution of cations. However, the mechanism of the relaxor behavior is very complicated, and the investigation of the mechanism is obviously outstripped by the exploitation of new relaxor-like compounds. Especially, in the case of doping and substitution, properties of a material change according to concentration of a dopant or fraction of a substitutional cation, and the mechanism seems to be further complicated. On the other hand, in the case of complex compounds, the ionic ratio at equivalent sites is unchangeable due to the charge neutral condition, and the mechanism seems to be simpler than the case of doping and substitution. Thus, most studies on relaxors have been conducted on lead-based complex perovskites, especially PMN. In addition, PMN shows a maximum of the dielectric constant and large electro-mechano-coupling coefficient around room temperature, which is favorable to technological applications. This might be also one of

the reasons why PMN has been studied the most among relaxors and regarded as a prototype of relaxors. From the applied point of view, (1-x)PMN-xPT solid solution system has been more favorable because PMN-PT shows the largest dielectric constant and electro-mechano-coupling coefficient around its morphotropic phase boundary with the PT fraction x = 0.3 **[32]**. However, (1-x)$Pb(Zn_{1/3}Nb_{2/3})O_3$-$xPbTiO_3$ (PZN-PT) solid solution system shows larger electro-mechano-coupling coefficient than PMN-PT **[33]**, and recently, the subject of applied researches on relaxors is shifting from PMN-PT to PZN-PT. Nevertheless, PMN is still studied the most from scientific interests: even in PMN, the mechanism has not been clarified yet.

An interesting anecdote is told about the complexity of relaxors; Smolenskii asked Landau to explain theoretically the strange dielectric behavior of the compounds discovered by him, but Landau refused his request because the behavior was too complex to explain. At the beginning, Smolenskii **[19,20]** tried to explain their dielectric behavior with the the compositional fluctuation model: within a PMN crystal, there are microscopic regions with different transition points due to compositional fluctuation on the *B*-site sublattice, and these regions gradually undergo phase transition. Consequently, a broad anomaly is formed in the dielectric constant curve as a function of temperature. Therefore, Smolenskii **[19,20]** named this phenomenon "diffuse phase transition". In this model, however, a broad peak of the dielectric constant might be explained but a glass-like dielectric dispersion can not be explained. Thus, another model has been required to explain consistently the mechanism of such dielectric behavior. Nowadays, the model with the formation of ferroelectric nanoregions in a paraelectric matrix is generally accepted and supported from both experimental and theoretical aspects. However, the formation mechanism of ferroelectric nanoregions has been not clarified yet. In addition, it has been also unclear the reason why these ferroelectric regions can not be macroscopic ferroelectric domain undergoing phase transition and the individual size of ferroelectric regions is restricted to nanometer size. Concerning this problem, there is an interesting report on the relation between the dielectric behavior and the *B*-site cation ordering. Fig.1.4 shows the flow diagram reported by Randall *et al.* **[34]** showing the classification of lead-based complex perovskites with respect to the dielectric behavior and the *B*-site cation ordering. As seen in this flow diagram, the dielectric behavior of lead-based complex perovskites seems to be closely related to the *B*-site cation arrangement. For example, in $Pb(Fe_{1/2}Nb_{1/2})O_3$ and $Pb(Fe_{1/2}Nb_{1/2})O_3$, there is no *B*-site cation ordering, and these are normal ferroelectrics (and also antiferromagnets due to the existence of magnetic Fe^{3+} ions). In $Pb(Mg_{1/2}W_{1/2})O_3$, there is 1:1 *B*-site cation ordering, and this is a normal antiferroelecric. On the other hand, in PMN, there is short-range 1:1 *B*-site cation ordering regardless of the 1:2 occupancy of Mg and Nb on the *B*-sites, and this is a typical relaxor. It is very interesting that there is a group of lead-based

complex perovskites showing both properties of normal ferroelectric and relaxor according to the *B*-site cation ordering, which are $Pb(Sc_{1/2}Nb_{1/2})O_3$ (PSN), $Pb(Sc_{1/2}Ta_{1/2})O_3$ (PST), and $Pb(In_{1/2}Nb_{1/2})O_3$ (PIN). In these compounds, the degree of ordering, σ ($0 \le \sigma \le 1$), of the *B*-site cation arrangement can be controlled by suitable thermal treatments, which implies the existence of an order-disorder phase transition on the *B*-site cation arrangement. With $\sigma \sim 1$, these compounds show normal ferroelectric (PSN and PST) or antiferroelectric behavior (PIN), but with decreasing σ, these come to show relaxor behavior. This classification suggests that the (anti)ferroelectric phase transition behavior and the averaged size of (anti)ferroelectric regions in lead-based complex perovskites are strongly affected by the *B*-site cation ordering.

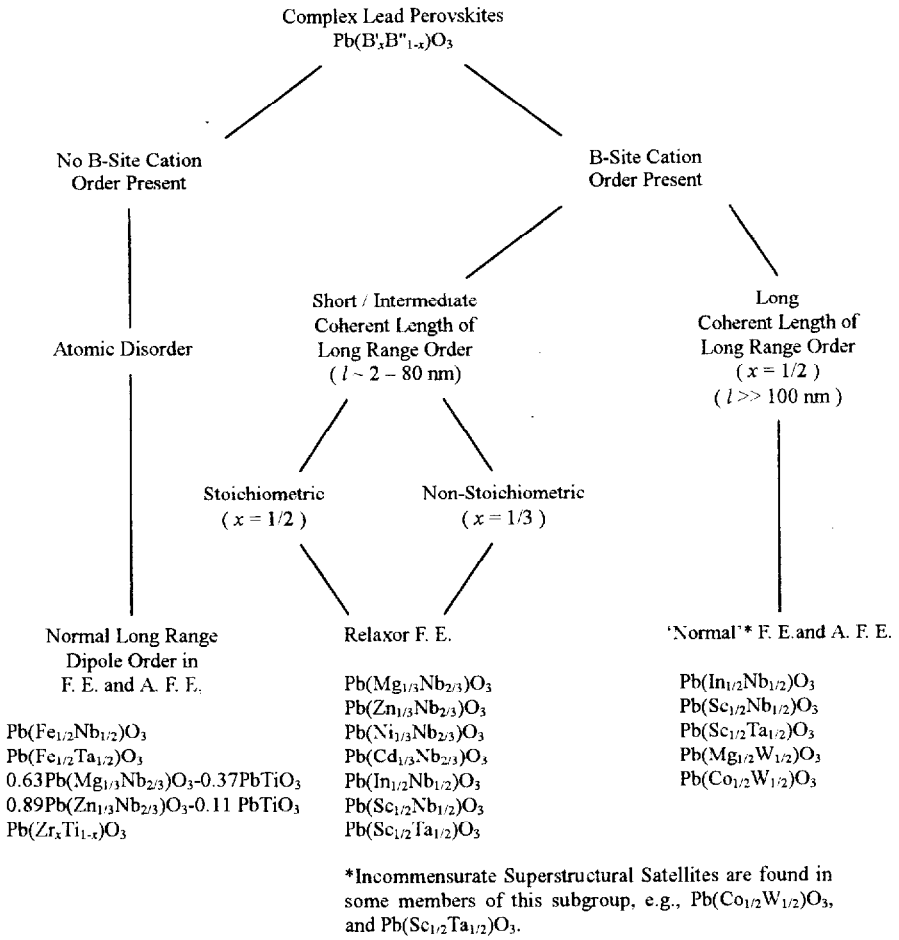

Fig. 1.3. Flow diagram showing the classification of complex lead perovskites with respect to B-site cation ordering and dielectric behavior **[34]**.

1.3. Objective

In the last decade, new experimental results on relaxors have obtained one after another, and subsequently, new physical models have been proposed to explain these experimental results consistently. In the background of such progress in the studies on relaxors, there seems to be the recent developments of techniques in structural investigations supported by large-scale experimental facilities and computational technologies, which have enabled to investigate a local structure in nanoscale to some extent. As a result, it has been clarified that the relaxor behavior can be explained to some extent assuming the structural model based on the experimental results. However, such studies have not answered the question why such a structure can be realized in relaxors. In order to answer that question, thermodynamic consideration is indispensable, because the realization of a certain state is dominated by Gibbs energy $G = H - TS$, where H and S are enthalpy and entropy, respectively: the thermodynamically most stable or metastable state, i.e., the state with a minimum Gibbs energy is usually realized, and if another state is actually realized, it is a nonequilibrium frozen state, i.e., glassy state. In addition, when some change, e.g., phase transition, occurs in a system, the value of entropy involved in the change often gives us the information about the mechanism of the change, and it is possible to determine experimentally these thermodynamic quantities only by the calorimetry. In other research fields such as magnetic properties, thermodynamic techniques, e.g., a heat capacity measurement, are widely employed as effective means of research. However, in many cases, the studies on relaxors from a macroscopic point of view are narrowed down to dielectric properties that are the most remarkable features of relaxors, and overall, the conventional studies on relaxors seem to be lacking in a thermodynamic point of view. Fundamentally, structural and thermodynamic studies should be complementary, and it is impossible to approach the nature of substances without either point of view. Thus, it is illogical to consider that it is possible to elucidate the mechanism of the relaxor behavior only by dielectric and structural investigations. On the other hand, there have been little systematic studies on the relation between the ferroelectric phase transition behavior and the *B*-site cation ordering in lead-based complex perovskites, especially from a thermodynamic point of view. It is considered that in lead-based complex perovskites, two different structural factors, i.e., ionic ordering and lattice distortion, are closely related to each other but contribute independently to the thermodynamic state of a system. Thus, the relation between the two factors is a very complicated and it seems to be very difficult to elucidate it. However, it is very meaningful to quantify the thermodynamic quantities involved in the ferroelectric phase transition with respect to the *B*-site cation ordering, and the quantification is surely helpful to understand the nature of lead-based complex perovskite relaxors.

In this study, focusing on lead-based perovskite relaxors that have been studied as a prototype of relaxors, the mechanism causing the unique dielectric response is investigated from a thermodynamic point of view mainly by heat capacity measurements. In *Chapter 2*, the explanation is given for the experimental techniques and apparatuses employed for investigations. Especially, for the heat capacity measurements by an adiabatic method, the principle, apparatus, and actual measurement procedure are interpreted in detail, because there is no commercial adiabatic calorimeter with high precision and accuracy*, and in many cases, a calorimeter is homemade, not excepting the present study. The greatest merit of the heat capacity investigation is that the heat capacity has no selection rule, and any phenomenon should be investigated in principle. It is so effective that once A. Einstein said "if you should understand the nature of a substance, but are allowed only one type of measurement to understand it, choose the heat capacity". On the other hand, it is not so easy to extract selectively individual contributions to the heat capacity: the merit is a demerit at the same time. In order to extract the contribution of interest, some theoretical approach and the experience in heat capacity investigations are required to some extent. As mentioned above, most of relaxors do not show any dramatic change in other properties than dielectric property around the dielectric peak temperature unlike usual (anti)ferroelectrics, and it is expected that it is difficult to find a singularity related to the dielectric response in their heat capacity even if it exists. Thus, before studying relaxors, it is meaningful to specify the features seen in the heat capacity of typical perovskite (anti)ferroelectrics, because the comparison with the heat capacity of typical (anti)ferroelectrics might provide a chance to extract some singularity in that of relaxors. In *Chapter 3*, for the most typical perovskite ferroelectric $BaTiO_3$ and representative lead-based perovskites $PbTiO_3$ and $PbZrO_3$, the features seen in their heat capacity are specified, and the basic concepts of heat capacity data analysis, i.e., theoretical models and methods, are interpreted in brief. In *Chapter 4*, for the typical relaxors $Pb(Mg_{1/3}Nb_{2/3})O_3$ (PMN) and $Pb(Mg_{1/3}Ta_{2/3})O_3$ (PMT), the singularities appearing in their heat capacity are extracted by comparing with that of typical perovskite (anti)ferroelectrics interpreted in *Chapter 3*. It is reported for the first time that an obvious thermodynamic signature related to the mechanism causing the unique dielectric response, which should be the formation of ferroelectric nanoregions, and anomalous large heat capacity at low temperatures. On the other hand, it can be considered that the large heat capacity at low temperatures may not originate from the nature of the relaxors but the complex perovskites. In order to verify this possibility, similar measurements are made for $Ba(Mg_{1/3}Ta_{2/3})O_3$, which is one of the barium-based complex perovskite oxides, and the large heat capacity is demonstrated to be the essential of the relaxors.

* Recently, high precision adiabatic calorimeter has become available from Torisha Co., Ltd. owing to technical cooperation with Prof. Tooru Atake, Materials and Structures Laboratory, Tokyo Institute of Technology.

In addition, for the physical models reported to explain the relaxor behavior, the validity of each model is verified from a thermodynamic point of view, based on the present experimental results. In *Chapters 5*, characteristic lead-based complex perovskite, $Pb(Sc_{1/2}Ta_{1/2})O_3$ (PST) is studied with respect to the correlation between the ferroelectric phase transition behavior and the *B*-site cation ordering. As mentioned above, this compound changes the dielectric property from ferroelectric to relaxor according to the *B*-site cation ordering, which can be controlled by suitable thermal treatments. Preliminary study is made for PST subjected to a thermal treatment under different conditions, and the variations of the phase transition behavior and dielectric property against the *B*-site cation ordering are discussed qualitatively on the basis of the results of dielectric constant measurements and heat capacity measurements by a thermal relaxation technique. Especially, ferroelectric PST has been considered as "normal" ferroelectrics so far, but in this study, it is clarified that ferroelectric PST is not "normal" but "singular" ferroelectric. Finally, in *Chapter 6*, the summary is provided through this study.

References

[1] N. S. Novosil'tsev and A. L. Khodakov, *Sov. Phys. –Tech. Phys.* 306 (1955).

[2] P. K. Davies and M. A. Akbas, *J. Phys. Chem. Solids* **61**, 159 (2000).

[3] J. B. Goodenough and J. M. Longo, Landolt-Börnstein, New Series, Group III, vol.4, Springer-Verlag, Berlin, p.126 (1970).

[4] M. Itoh, R. Wang, Y. Inaguma, T. Yamaguchi, Y.-J. Shan, and T. Nakamura, *Phys. Rev. Lett.* **82**, 3540 (1999).

[5] R. E. Cohen, *Nature* **358**, 136 (1992); *Ferroelectrics* **136**, 65 (1992).

[6] Y. Kuroiwa, S. Aoyagi, A. Sawada, J. Harada, E. Nishibori, M. Takata, and M. Sakata, *Phys. Rev. Lett.* **87**, 217601 (2001).

[7] K. Uchino, E. Sadanaga, and T. Hirose, *J. Am.Ceram. Soc.* **72**, 1555 (1989).

[8] E. Sawaguchi, H. Maniwa, and S. Hoshino, *Phys. Rev.* **83**, 1078 (1951);E. Sawaguchi, G. Shirane, and Y. Takagi, *J. Phys. Soc. Jpn.* **6**, 333 (1951).

[9] E. Sawaguchi and T. Kittaka, *J. Phys. Soc. Jpn.* **7**, 336 (1952).

[10] V. J. Tennery, *J. Electrochem. Soc.*, **112**, 1117 (1965); *J. Am. Ceram. Soc.* **49**, 483 (1966).

[11] L. Goulpeau, *Sov. Phys.-Solid State* **8**, 1970 (1967).

[12] B. A. Scott and G. Burns, *J. Am. Ceram. Soc.* **55**, 331 (1972).

[13] R. W. Whatmore and A. M. Glazer, *J. Phys. C: Solid State Phys.* **12**, 1505 (1979).

[14] J. F. Scott and C. A.-Paz de Araujo, *Science* **246**, 1400 (1989).

[15] C. A.-Paz de Araujo, J. D. Cuchiaro, L. D. McMillan, M. C. Scott, and J. F. Scott, *Nature* **374**, 627 (1995).

[16] G. A. Smolenskii, A. I. Agranovskaya, and S. N. Popov, *Sov. Phys. –Solid State* **1**, 147 (1958).

[17] G. A. Smolenskii, V. A. Isupov, and A. I. Agranovskaya, *Sov. Phys. –Solid State* **1**, 149 (1958); *ibid*, **1**, 150 (1958).

[18] G. A. Smolenskii, A. I. Agranovskaya, and V. A. Isupov, *Sov. Phys. –Solid State* **1**, 907 (1959).

[19] G. A. Smolenskii, V. A. Isupov, A. I. Agranovskaya and S. N. Popov, *Sov. Phys. –Solid State* **2**, 2584 (1961).

[20] G. A. Smolenskii, *J. Phys. Soc. Jpn.* (*Proc. 2nd Int. Meeting on Ferroelectricity*) **28**, S26 (1970); *Ferroelectrics* **53**, 129 (1984).

[21] G. Burns and A. Scott, *Solid State Commun.* **13**, 423 (1973).

[22] D. Viehland, S. J. Jang, L. E.Cross, and M. Wuttig, *J. Appl. Phys.* **68**, 2946 (1990).

[23] R. Blinc, J. Dolinšek, A. Gregorovic, B. Zalar, C. Filipic, Z. Kutnjak, A. Levstik, and R. Pirc, *Phys. Rev. Lett.* **83**, 424 (1999); *J. Phys. Chem. Solids* **61**, 177 (2000).

[24] L. E. Cross, *Ferroelectrics* **76**, 241 (1987).

[25] V. Bharti and Q. M. Zhang, *Phys. Rev.* **B63**, 184103 (2001).

[26] H. Schmitt and A. Dorr, *Ferroelectrics* **93**, 309 (1989).

[27] T. Tsurumi and Y. Hoshino, *J. Am. Ceram Soc.* **72**, 278 (1989).

[28] C.Ang, Z. Yu, P. Lunkenheimer, J. Hemberger, and A. Loidl, *Phys. Rev.* **B59**, 6670 (1999).

[29] A. Chen, Z. Yu, J. Scott, A. Loidl, R. Guo, A.S. Bhalla, and L. E. Cross, *J. Phys. Chem. Solids* **61**, 191 (2000).

[30] H. Okamoto, T, Mitani, Y. Tokura, S. Koshihara, T. Komatsu, Y. Iwasa, T. Koda, and G. Saito, *Phys. Rev.* **B43**, 8224 (1991).

[31] S. Horiuchi, R. Kumai, Y. Okimoto, and Y. Tokura, *Phys. Rev. Lett.* **85**, 5210 (2000).

[32] S.-E. Park and T. R. Shrout, *J. Appl. Phys.* **82**, 1804 (1997).

[33] J. Kuwata, K. Uchino, and S. Nomura, *Ferroelectrics* **37**, 579 (1981).

[34] C. A. Randall and A. S. Bhalla, *J. Appl. Phys.* **29**, 327 (1990).

Chapter 2

Experimental Apparatuses and Techniques

2.1. Furnace for Sample Synthesis

Most of compounds synthesized in this study include lead as a component. When the single crystals of these compounds are synthesized by a flux method, PbO and PbF_2 are used very much as flux, which are poisonous substances with high volatility at high temperatures. PbO and PbF_2 easily evaporate above their melting points, and evaporating PbO and PbF_2 corrode the surroundings seriously. Thus, special care was taken for a furnace to prevent lead pollution. The cross section of the vertical tube electric furnace used in this study is shown in Fig.2.1. A cylindrical electric heating element is placed at the center of the furnace and lagged with heat-insulating blocks. An outer alumina tube to protect the heating element is inserted into the heating element and fixed semipermanently. In addition, an inner alumina tube to protect the outer tube is inserted into the outer tube: the furnace has a double-tube structure. The other alumina tube is only for supporting a crucible. Since the inner and supporting tubes are directly exposed in an evaporating lead atmosphere, both tubes are gradually damaged by using repeatedly under such condition, and so it is necessary to renew the tubes when seriously damaged. Of course, lead is poisonous for the human body, and the tubes must be tightly closed in order to prevent an evaporating lead leak to the outside of the furnace. Thus the upper edge of the inner tube and the lower edge of the supporting tube are plugged up with heat-resistant silicorn plugs with a hole for a gas flow, and the space between the inner and supporting tubes are filled up with kaolinite wool, which is a heat-insulating material.

A platinum crucible is used in the synthesis of lead-based perovskites. However, a platinum crucible is easily damaged at high temperatures by a reducing agent such as a small amount of uncombined pure metal surviving in a metal compound and an organic compound, as the platinum is very sensitive to a reducing atmosphere. When starting powder materials are mixed using a mixing medium such as ethanol and acetone, the powder mixture should be dried well before being put in a platinum crucible. In the case using a metal oxide, it should be heated preliminarily in air at a high enough temperature to be completely oxidized before using because a metal oxide product sometimes includes an unoxidized metal ingredient. In the case of non-oxides such as PbF_2, of course it can not be heated preliminarily, but the existence of

uncombined pure metal is a serious problem. Thus an oxygen gas flow is provided to keep the inside of the furnace to be an oxidizing atmosphere whenever the furnace is working. Under an oxidizing atmosphere, a surviving metal component is oxidized in heating process without damaging a platinum crucible. For a gas flow, a hole is made at the center of both silicorn plugs. Oxygen gas is provided little by little from a gas source to the lower furnace edge and discharged from the upper furnace edge to a draft through vinyl tubes. Since discharged oxygen gas includes evaporating lead, a chemical trap with nitric acid is equipped between the furnace and the draft.

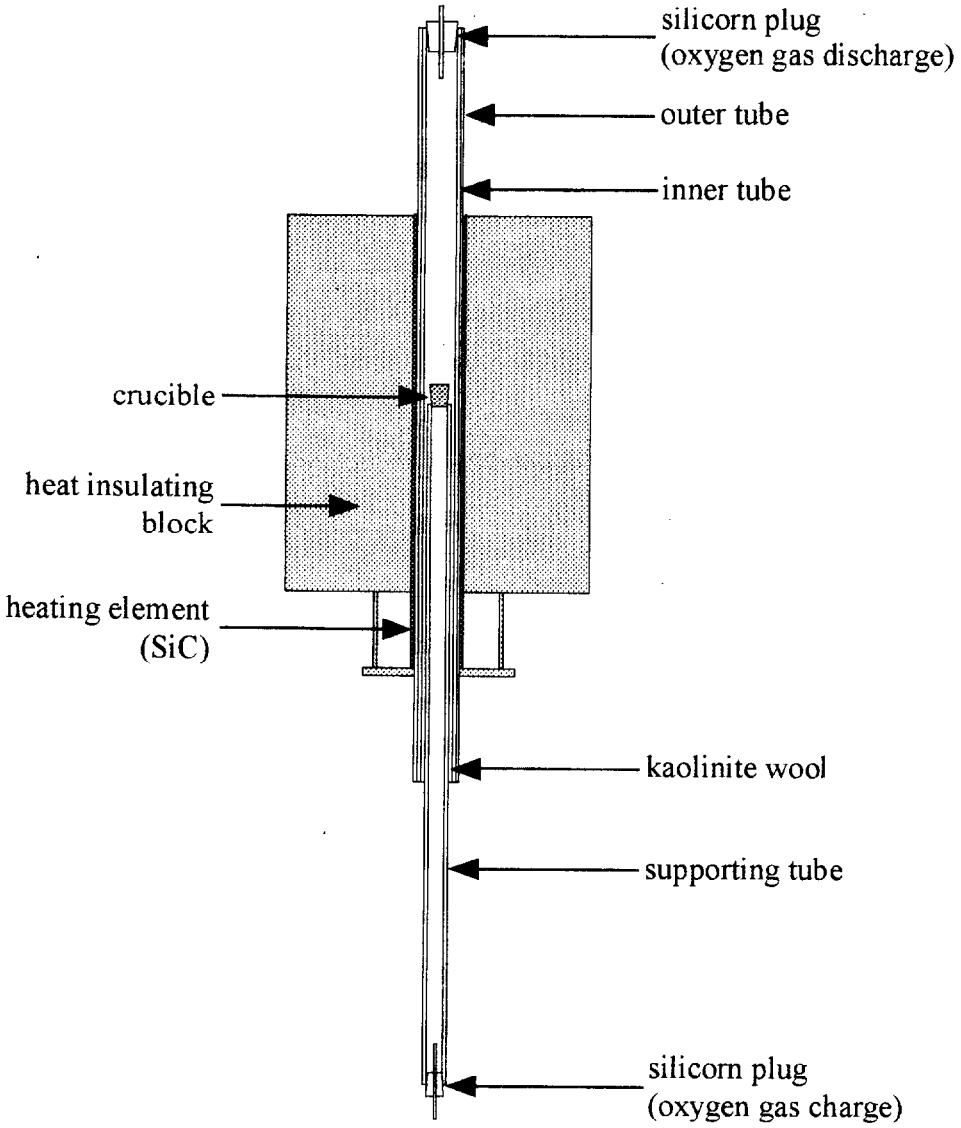

Fig. 2.1. Schematic view of the electric furnace employing for the synthesis of Pb-based perovskite oxides in this study.

2.2. Heat Capacity Measurements by an Adiabatic Method

2.2.1. Principle

An adiabatic method is the most accurate method for heat capacity measurements. Several methods are known for heat capacity measurements and each of these methods has its merits and demerits. Although a suitable method should be selected according to circumstances, concerning the accuracy of measured data there is no method as accurate as the adiabatic method. In addition, the following points can be cited as other merits of the adiabatic method: (1) any forms of sample including liquid can be objects for measurements, as a sample is directly put into a calorimeter vessel; (2) it is possible to measure the heat capacity at a first-order phase transition; and (3) a phenomenon that take a quite long time to reach a thermal equilibrium state, e.g., a glass transition, can be an object for observation, as it is possible to measure temperature over a long period after energy (Joule heat) is applied to a sample.

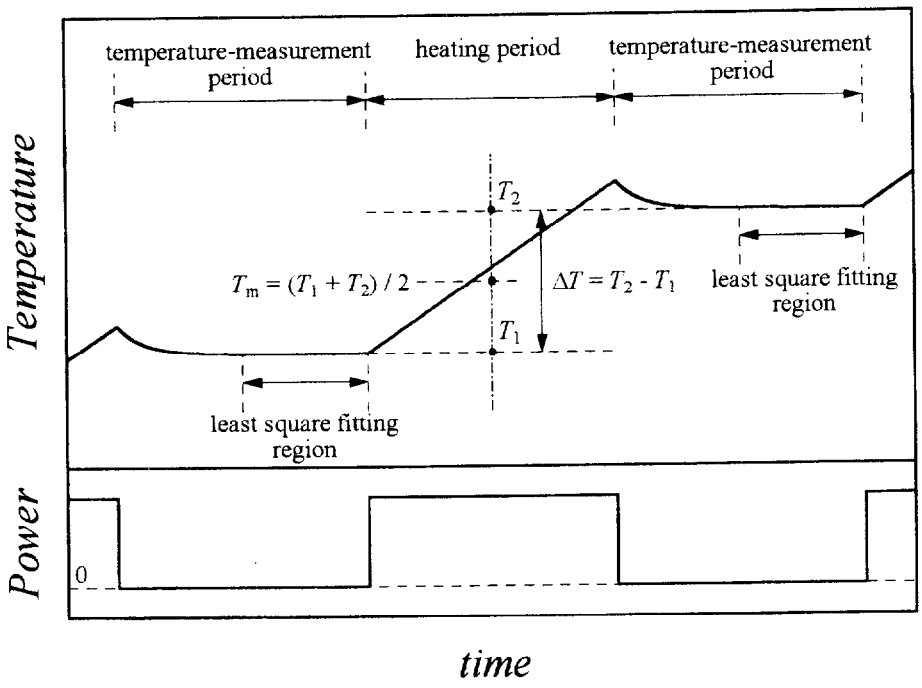

Fig. 2.2. Schematic time sequence in adiabatic calorimetry. The detail is explained in the text.

The principle of the adiabatic calorimetry is simply as follows. At first, a sample temperature T_1 is measured in a thermal equilibrium state under the adiabatic condition. Next, keeping the adiabatic condition, finite energy ΔE is applied to a sample. After that, a sample temperature T_2 is measured again. Since a sample has been under the adiabatic condition, all of the applied energy contributes to the temperature rise of a sample, $\Delta T = T_2 - T_1$. Thus, sample heat capacity $C_{\text{sample}} = \Delta E/\Delta T$ can be obtained as averaged heat capacity at an averaged temperature $T_m = (T_1 + T_2)/2$ between T_1 and T_2.

This is an ideal case, and in an actual measurement, there are of course some experimental restrictions. Fig.2.2 shows a schematic time sequence in adiabatic calorimetry. Although a measured temperature is a temperature of a thermometer mounted on a calorimeter vessel, this can be considered as a sample temperature since the system that contains a sample and a vessel is considered to reach a thermal equilibrium state finally. In a temperature-measurement period, a sample temperature is measured at 30 s intervals. Temperature data in the latest time region (usually a half of the period) are least-square fitted with a linear function, and its slope shows a temperature drift rate. Since it is quite difficult to establish a complete thermal equilibrium state experimentally, the system is considered to reach a thermal equilibrium state when a temperature drift rate is nearly constant. For an accurate measurement, it should be kept within $\pm 5 \times 10^{-5}$ K/min. At this time, assuming that a heat leak is steady, a fitting linear function is extrapolated to time points in the middle of previous and next heating periods. Temperatures at previous and next time points are T_2 and next T_1, respectively. Applied energy to the system is Joule heat generated by a heater mounted on a vessel with a thermometer. In a heating period, since a heater resistance changes slightly with increasing temperature, the heater voltage and current are measured at 30 s intervals from 15 s later of a heating start, where the current is measured as the voltage between both edges of a standard resistance inserted in the same circuit in series. Finally, applied energy is obtained as Joule heat averaged over a whole heating time by

$$\Delta E = t \cdot \sum_i V_i I_i \Big/ i , \tag{2.1}$$

where t is measured heating time, V_i and I_i are measured voltage and current, respectively, and i is the number of measurement points. Heat capacity directly measured in an actual measurement is total heat capacity of the system. Therefore, heat capacity of a sample can be obtained by subtracting that of a vessel from total heat capacity. To be exact, heat capacity of a sample can be obtained by

$$C_{\text{sample}} = \frac{\Delta E - (H_{\text{vessel}}(T_2) - H_{\text{vessel}}(T_1))}{\Delta T} , \tag{2.2}$$

where $H_{\text{vessel}}(T_1)$ and $H_{\text{vessel}}(T_2)$ are enthalpy of a vessel at temperatures T_1 and T_2, respectively.

Thus it is necessary to measure heat capacity of a vessel and derive enthalpy from measured heat capacity as a function of temperature in advance.

Since heat capacity is defined as a temperature derivative of enthalpy H, a true value of heat capacity can be obtained at a limit of $\Delta T \to 0$. In an actual measurement, however, an experimental error increases when ΔT is too small, and it is necessary to take a suitable temperature rise. On the other hand, when ΔT is too large, measured heat capacity is quite different from its true value and curvature correction must be done because heat capacity is not a linear function of temperature. For these reasons, a measurement is usually carried out with an empirical ΔT of 1 ~ 2 K except for the temperature regions where heat capacity shows a large change rate as a function of temperature, e.g., a low temperature region and a phase transition region. With this value of ΔT, the deviation from a true value can be within an experimental error and curvature correction is not needed. As clearly seen Eq.(2.2), in the case of a sample with a small amount, an experimental error increases due to small contribution of a sample to total heat capacity, and it is difficult to measure heat capacity accurately. This is the worst demerit of adiabatic calorimetry. Therefore, it is eagerly desired to miniaturize and simplify a calorimeter vessel.

2.2.2. Construction of an Adiabatic Calorimeter

There has been no commercial adiabatic calorimeter with high performance, and in many case, a homemade apparatus has been used for precise adiabatic calorimetry. In this laboratory, there have been three homemade adiabatic calorimeters, but the upper limit temperature of a measurement is usually 300 K, at most 350 K, due to the heat-resistance of materials composing these calorimeters. Scientifically, however, there are many compounds showing interesting properties above room temperature, and it is eagerly desired to construct a new adiabatic calorimeter that enable to measure heat capacity up to higher temperatures. Especially, in relaxors such as PMN, it is expected to observe an interesting thermal property in a much higher temperature region above room temperature. Thus, a new adiabatic calorimeter that is able to measure heat capacity up to 420 K was constructed in this study.

Materials

Basic techniques for the construction of an adiabatic calorimeter for low temperature calorimetry has been already established **[1]**, and cultivated in this laboratory for a long time **[2,3]**. Although a structure of an adiabatic calorimeter is quite different between for high temperature calorimetry **[4]** and for low temperature calorimetry **[1-3]**, a measurement up to

about 500 K can be carried out with an adiabatic calorimeter with a structure for low temperature calorimetry. Therefore, the selection of materials to be composing a calorimeter becomes the most important. In this laboratory, the following materials have been conventionally used as parts of a calorimeter: (1) a low melting point alloy, e.g., woods alloy for uniting metallic materials; (2) a silk-coated copper wire for an electric (and thermal) lead wire; (3) a silk-coated constantan wire for a heater of adiabatic shields and thermal station rings; (4) a silk-coated chromel-constantan (type-E) thermocouple; and (5) a nylon® wire for hanging adiabatic shields and thermal station rings (about the names of each parts, explained in the next subsection). However, it is obvious that these materials can not be used above 350 K. In the present construction, all of these materials were replaced by materials with high heat-resistance.

About a coating of wires, silk is not suitable for use at high temperatures because it is soon damaged and burned at worst. Thus, a suitable coating of wires should be selected according to a necessary quantity and the positions where each wire is used. Since a copper wire is used very much as an electric lead wire, a suitable coated copper wire should be selected that is as cheap and easy to treat as possible, i.e., mass-produced organic polymer-coated copper wires. Among them, a polyester-coated copper wire is the most widely used in every technological field, and therefore it is cheap and there is a variety of diameters. In addition, it is well suited for varnish (GE7031, General Electric Co.) used for gluing wires to metallic materials. However, the temperature index* of polyester is 155 °C (~ 428 K), and it seems to be a little insufficient for repeated using up to 420 K. Concerning heat-resistance, polyimide is the best organic polymer with the temperature index of 220 °C (~ 493 K), which is sufficient for repeated using up to 420 K and is also well suited for GE varnish. Unfortunately, however, the thinnest diameter of available polyimide-coated copper wires is 0.2 mm on inquiry, which is a little thick for an adiabatic calorimeter. Actually, a thin wire is unfavorable to an electric lead wire because the high resistivity may cause an increase of a signal-to-noise ratio. In adiabatic calorimetry, however, it is necessary in principle to suppress the thermal conduction between an adiabatic control unit and the exterior through lead wires, and a thin wire is favorable to adiabatic calorimetry. For this reason, a copper wire with the diameter of ~ 0.1 mm has been conventionally used in this laboratory. When the diameter becomes twice, the thermal conductance becomes four times through an increase of the cross section. On the other hand, the thermal conduction through a lead wire depends on not only the cross section but also the path. Thus, the gain of thermal conductance with diameter can be compensated by the loss with path. A polyimide-coated copper wire with the diameter of 0.2 mm was finally selected in the present construction.

---

* Temperature index is an index to the heat-resistance of electric insulating materials, mainly organic polymers. It is generally defined as the temperature obtained by extrapolating the Arrhenius equation to 20000 h assuming that the relation between thermal lifetime and temperature obeys the Arrhenius law.

For a heater of adiabatic shields and thermal station rings, coating with higher heat-resistance is required, as a heater is a heat source. Thus, a glass wool-coated constantan wire with the diameter of 0.18 mm and resistivity of about 17 Ω/m was selected. Glass wool is an assembly of fine glass fibers, and it is also suited for GE varnish but easily crumbles with scratch or hard tension. Thus, it is necessary to treat it carefully.

As a thermocouple with a heat-resistant coating, teflon-coated thermocouples are manufactured by Omega Enginecring, Inc. Thus, a chromel-constantan (type-E) thermocouple with each diameter of 0.13 mm was purchased and used for every component of an adiabatic control unit except for a colorimeter vessel, the thermocouple of which is specially made to be more sensitive to a little temperature difference. Teflon® [poly(tetra-fluoroethylene)] has also high heat-resistance but is not suited for any adhesives including GE varnish. Thus, it is necessary to etch the surface of teflon-coating with a fluororesin surface-etching chemical (Tetraetch®, Junkosha, Inc.) to be suited for adhesives.

For wires for hanging each component of an adiabatic control unit, a material with quite low thermal conductivity is required because these wires are joining two parts with quite different temperatures. In addition, flexibility and tensile strength are also required for the purpose. For these reasons, a nylon wire has been conventionally used, but the nylon is weak for heat. Thus, at the beginning, a stainless steel wire with the diameter of 0.1 mm was examined because it has low thermal conductivity*, high heat-resistance, flexibility and tensile strength. However, a few components of an adiabatic control unit are removable to mount a calorimeter vessel inside them, and the strong elasticity of the stainless steel wire was obstructive to putting on these components. Moreover, the stainless steel wire snapped frequently at a bent point for hanging due to elastic fatigue. Although some other alloy wires, e.g., constantan, were also examined, the situation remained the same or rather became bad. Such situations has never been seen in the case of a nylon wire, which means that an organic polymer wire is more suitable than alloy wires for the purpose. The most heat-resistant organic polymer is polyimide, but no polyimide wire was available on inquiry, and only a polyimide tube was manufactured by Chemix Co., Ltd., which is the same company that manufactures polyimide-coated copper wire. Thus, the aptitude of a polyimide tube with the internal diameter of 0.2 mm and the thickness of 0.04 mm was examined for hanging the components, and it was found to be quite suitable for the purpose. Finally, all the stainless steel wires were replaced by polyimide tubes.

* The thermal conductivity of SUS27, a typical stainless steel, is 15 $Wm^{-1}K^{-1}$ at 300 K, while that of copper is 398 $Wm^{-1}K^{-1}$.

Main Body

Fig.2.3 shows the cross section of the main body of the adiabatic calorimeter. This calorimeter was designed by Dr. Kawaji, who is an associate professor at Materials and Structures Laboratory, Tokyo Institute of Technology, when he was an associate professor at Hiroshima University. The basic design of this calorimeter is the same as that of the established calorimeters in this laboratory except that components of an adiabatic control unit are increased in order to reduce a heat leak through radiation at high temperatures.

The adiabatic control unit of the calorimeter is composed of six independent components; top and bottom adiabatic shields, inner and outer radiation shields, and inner and outer thermal station rings, shown in Fig.2.4 in enlarged scale. The top shield and the two rings are permanently fixed to the main body, as these are connected with each other by lead wires, while the bottom, inner, and outer shields are removable to mount a calorimeter vessel inside these shields. A calorimeter vessel is surrounded by the top and bottom adiabatic shields. The top shield is controlled so as not to generate a temperature difference between a vessel and itself, while the bottom shield is controlled to the top shield in the same manner. A temperature difference between the top shield and a vessel is detected with a multi-thermocouple, which is permanently fixed on the outside surface of a vessel at one edge and removable on the inside surface of the top shield at the other edge (see the next subsection). A temperature difference between the top and bottom shields is detected by a double chromel-constantan (type-E) thermocouple, which is permanently fixed on the top shield side and removable on the bottom shield side. This first unit is suspended by polyimide tubes from the inner thermal station ring and surrounded by the inner radiation shield. The inner ring is controlled to the top shield with a type-E thermocouple, but a temperature difference corresponding to the potential difference of 125 μV in the type-E thermocouple is made on purpose between them in order to ensure cooling power for the first unit. This temperature difference is made using zero-point correction for a DC amplifier that amplifies a signal of the type-E thermocouple between the inner ring and the top shield. The inner shield is controlled to the inner ring with a type-E thermocouple that is permanently fixed on the inner ring side and removable on the inner shield side. Thus, the temperature of the inner ring and shield is always a little lower than that of the first unit. This second unit is suspended by polyimide tubes from the outer thermal station ring and surrounded by the outer radiation shield. The outer ring is controlled to the inner ring so that the temperature is always lower than that of the second unit by making a temperature difference corresponding to the potential deference of 250 μV in the type-E thermocouple in the same manner as between the inner ring and the top shield. The outer shield is controlled to the outer ring with a type-E thermocouple that is permanently fixed on the outer ring side and removable on the outer shield side. This third unit is suspended by polyimide tubes from the lower part of

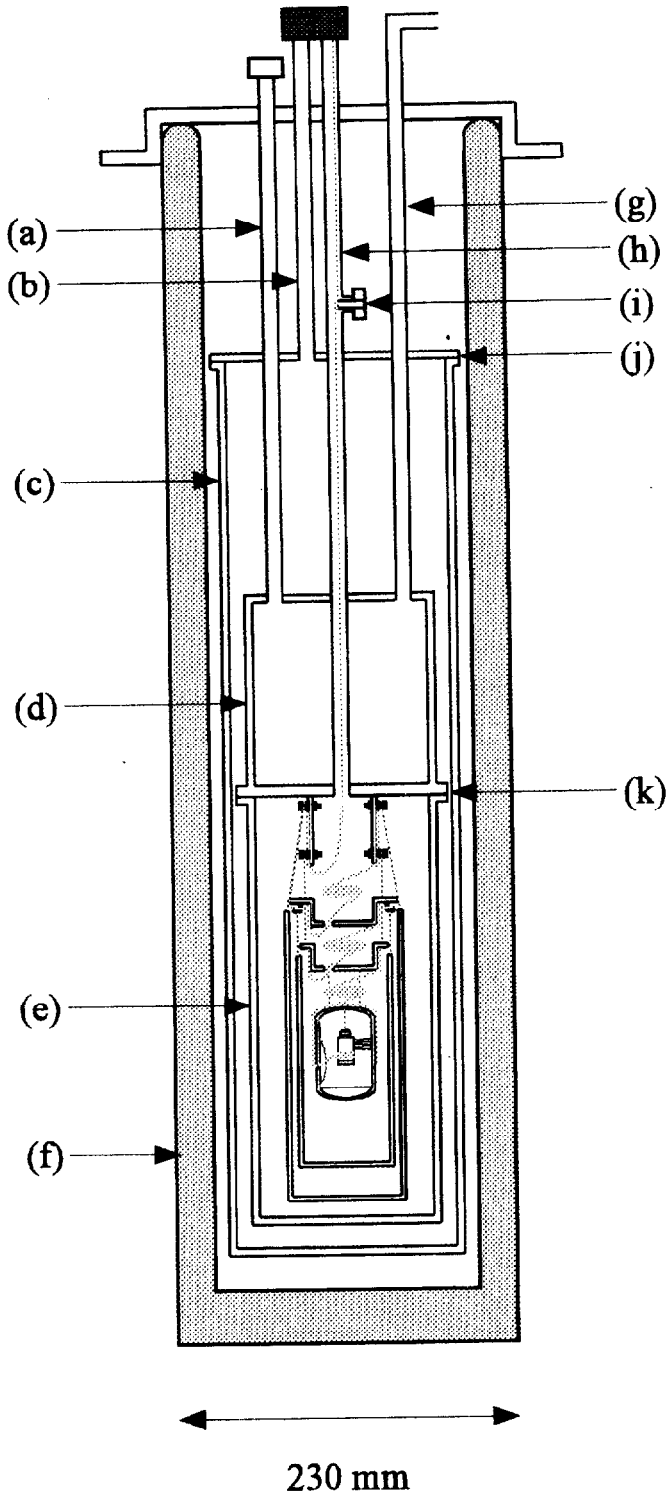

Fig. 2.3. Cross section of the main body of the adiabatic calorimeter constructed in the present study: (a) coolant charge tube, (b) outer jacket evacuation tube, (c) outer jacket, (d) coolant container, (e) inner jacket, (f) vacuum can, (g) coolant discharge tube, (h) inner jacket evacuation tube, (i) thermal anchor, (j) top flange, (k) coolant container flange.

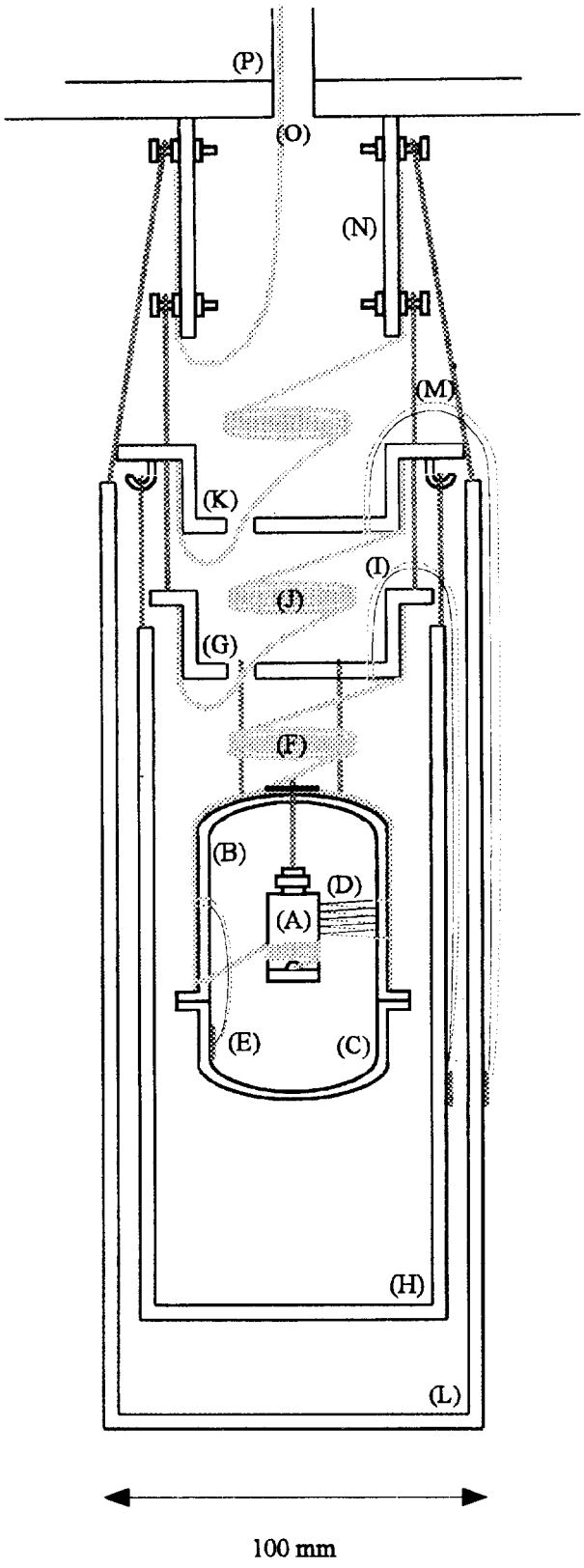

Fig. 2.4. Adiabatic control unit of the constructed adiabatic calorimeter: (A) calorimeter vessel, (B) top adiabatic shield, (C) bottom adiabatic shield, (D) thermocouple between (A) and (B), (E) thermocouple between (B) and (C), (F) lead wires and thermocouple between (B) and (G), (G) inner thermal station ring, (H) inner radiation shield, (I) thermocouple between (G) and (H), (J) lead wires and thermocouple between (G) and (K), (K) outer thermal station ring, (L) outer radiation shield, (M) thermocouple between (K) and (L), (N) lower part of the coolant cantainer, (O) edge of the inner jacket evacuation tube.

the coolant container. Each removable edge of the thermocouples is screwed on the side of each shield.

A heater wire with 100 Ω (about 6 m), which is glass wool-coated constantan wire, is bent back in the middle to be a duplex wire of about 3 m, which is noninductive for direct current. The bent point is put on the center of each component of the adiabatic control unit and then the wire is put around it spirally and uniformly to the flange with GE varnish. Thus, the both terminals of the heater wire come to around the flange of each component. For the removable bottom, inner, and outer shields, aluminum foil is glued with GE varnish on the whole outside surface in order to make close thermal contact between the heater wire and the body. The terminals of the heater wire of the bottom, inner, and outer shields are connected with a coupler to the terminals of the lead wires made around the flange of the top shield, and the inner and outer rings, respectively. The terminals for connecting the lead wires of a calorimeter vessel are made around the flange of the top shield. The lead wires that originate in these terminals are put around the top shield spirally from the flange to the center, and then connected to the inner ring after circling around several times in the space between the top shield and inner ring in order to gain path. Next, these wires are put around the inner ring, and then connected to the outer ring in the same manner. After put around the outer ring, these wires are connected to the lower part of the coolant container, and then put around this part. Finally, the wires are led to the external terminals along the inner jacket evacuation tube through the thermal anchor, which is soaked in liquid nitrogen, the temperature of which is kept to be liquid nitrogen temperature whenever the colorimeter is working. Aluminum foil is glued with GE varnish on the whole outside surface of each component and the lower part of the coolant container over the put lead wires. This multifold structure composed of the two thermal station rings and the thermal anchor prevents direct thermal conduction through the lead wires between the fist adiabatic unit and the exterior, and contributes greatly to fine adiabatic control.

The whole adiabatic control unit is covered with the inner jacket, which is screwed on the coolant container flange, where a sealant indium wire is put between them. The inner jacket is further covered with the outer jacket, which is screwed on the top flange in the same manner as the inner jacket. The vacuum can (Precision Cryogenic Systems, Inc.) is put on to cover the whole body and filled with liquid nitrogen whenever the calorimeter is working. The insides of the inner and outer jackets can be independently evacuated or filled with a small amount of helium gas for thermal exchange. Following preliminary evacuation with an oil rotary pump to $\sim 4.0\times 10^{-2}$ Pa, main evacuation is carried out with an oil diffusion pump to $\sim 1.0\times 10^{-3}$ Pa, where the rotary pump is backing the diffusion pump. Introducing liquid nitrogen into the vacuum can, high vacuum of $\sim 2.0\times 10^{-4}$ Pa is always maintained. A measurement can be carried out only in a heating run and is usually started at 80, 50, or 13 K. When a

measurement is started at 80 K, the inside of both jackets is filled with a small amount of helium gas (~ 10 Pa), and then a calorimeter vessel is cooled down to 80 K in ~ 3 h. In the case of a measurement from 50 K, a calorimeter vessel is preliminarily cooled down to 80 K in the same manner, and then only the inside of the outer jacket is evacuated to isolate thermally the inner jacket. After that, liquid nitrogen of ~ 500 ml is introduced into the coolant container through the coolant charge tube, and then pumped through the coolant discharge tube with an oil rotary pump. Thus the liquid nitrogen transforms into a solid phase, and a calorimeter vessel is cooled down to 50 K in ~ 3 h. Empirically, the solid nitrogen seems to remain in the coolant container for a few days. In the case of a measurement from 13 K, following preliminary cooling down to 80 K, only the inside of the outer jacket is evacuated. After that, liquid helium is introduced into the coolant container using a liquid helium transfer tube, which is inserted to the coolant charge tube, and evaporated helium gas is discharged through the coolant discharge tube to the exterior. When temperature reaches to around 30 K, the inside of the inner jacket should be evacuated because the helium gas is adsorbed on the surface of each component within the inner jacket and the adsorbed helium causes a serious experimental error during a measurement: a part of applied energy is wasted on the desorption of the helium. After evacuating the inside of the inner jacket, a calorimeter vessel is cooled by the thermal conduction through the lead wires alone. A calorimeter vessel is cooled down to liquid helium temperature in ~ 1 h but liquid helium is continuously introduced until the coolant container is completely filled, which can be confirmed by the pulsation of a balloon that is equipped in the vicinity of the coolant discharge opening. Empirically, the liquid helium remains in the coolant container for ~ 6 h.

Calorimeter Vessel

Although a calorimeter vessel can be fundamentally employed for any adiabatic calorimeters, in this laboratory a calorimeter vessel has been regularly employed for a specific calorimeter for convenience. In the present case, however, a calorimeter vessel that can be used at high temperatures is especially required. Thus, a new calorimeter vessel for the new adiabatic colorimeter was also constructed in this study.

The external form of the calorimeter vessel is schematically shown in Fig.2.5. The body is cylindrical shape with the diameter of ~ 13 mm and the height of ~ 23 mm. As a result of a volume measurement using pure water, the volume of the vessel is estimated to be 1930 mm^3. This vessel is quite miniaturized relative to conventional vessels and the miniaturization is mainly owing to employment of a small thermometer. The vessel is mainly composed of four parts, namely the screw top, the upper and lower bodies, and the radiation shield. The upper body has a screw mouth for introducing a sample at the center. After introducing a sample, the

mouth is tightly closed with the screw top, where a sealant gold plate is put between them. This sealant is renewed after using a few times, but every sealant should have the same mass because the heat capacity of the calorimeter vessel should be unchangeable. Therefore, in this calorimeter vessel, a gold plate with the thickness of 0.2 mm, the diameter of ~ 6 mm, and the mass of 106.5 mg is used every time. Since strong force is mechanically applied to the screw top and the upper body, these are made of beryllium copper alloy, which has mechanical strength. On the other hand, the lower body is made of copper, and the cylindrical sheath for the thermometer and the heater is made at the center. The lower edge of the lower body is covered with a copper plate as the radiation shield for the thermometer. Before uniting, all of these components are plated with gold, which is effective to prevent both radiation and reaction between sample and copper. For uniting the components with each other, eutectic solder (melting point of 183 °C) is used for a high temperature heat capacity measurement up to 420 K.

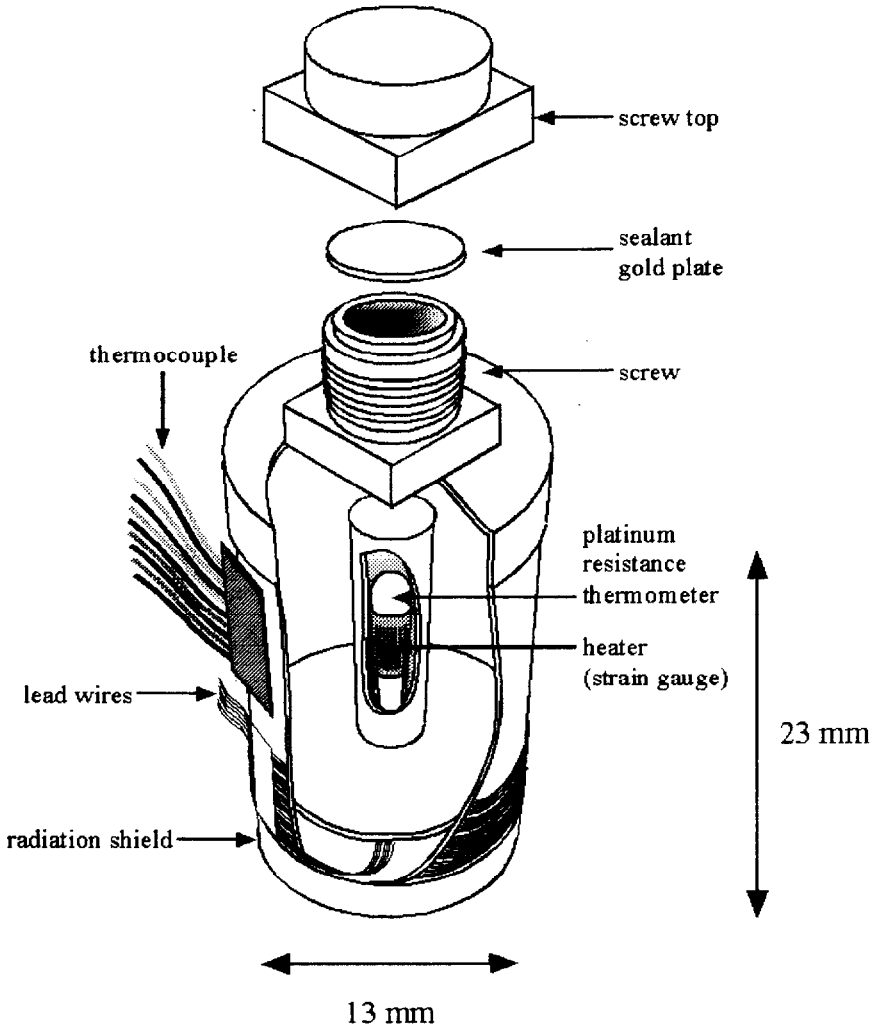

Fig. 2.5. Schematic view of the calorimeter vessel made in the present study.

The thermometer mounted on the vessel is a platinum resistance thermometer (Model S1059PJ5X6, Serial No.525, Minco Products, Inc.), which is calibrated on the basis of International Temperature Scale 90 (ITS-90) from 13 K up to 533 K. A strain gauge (Type KFH-5-120-C1-16, 120 Ω, Kyowa Electric Instruments Co., Ltd.) is employed for the heater, which has a small temperature coefficient of resistivity. The thermometer and the heater are bound with fine copper wires. This unit is inserted to the sheath of the lower body, and permanently fixed with solder. A polyester-coated copper wire with the diameter of 0.08 mm is employed for the lead wires of the thermometer and the heater. Although polyester seems to be a little insufficient for using up to 420 K as mentioned above, thick wires can not be used for a calorimeter vessel from both aspects of thermal conduction and ease in treating. The thermometer has four terminals, and four wires are joined to each terminal with solder and covered with GE varnish. On the other hand, the heater has two terminals, and two wires are joined to one terminal and one wire is joined to the other terminal. Thus, the voltage between both terminals is measured by the three-terminal method because it is necessary to take account of the Joule heat generated in the lead wires between the heater and the top shield. These seven lead wires are led to the outside from a small hole around the fringe of the lower body, and then put around the body a few times and glued with GE varnish in order to make good thermal contact.

The thermocouple fixed on the outside surface of the vessel is composed of double type-E thermocouple and triple Au+5atom%Fe-chromel thermocouple in order to be highly sensitive to a slight temperature difference between the vessel and the top shield. The Au+5atom%Fe-chromel thermocouple is sensitive especially at low temperatures. Each wire of the thermocouple is a teflon-coated wire with the diameter of 0.08 mm. Since the Au+5atom%Fe wire is alloyed with solder, the wires are joined with silver solder. Both terminals are joined to polyimide-coated copper wires also with silver solder. Both edges of the thermocouple are covered with a polyimide thin film (LARC-TPI) for electric insulating and then with a copper plate with the thickness of ~ 0.1 mm, where these are glued with GE varnish. The edge without terminals is fixed on the surface of the lower body with solder, and the other edge with terminals is screwed on the inside surface of the top shield.

When a sample is put into the vessel, it is also necessary to introduce a small amount of helium gas into the vessel in order to ensure the thermal uniformity within the vessel during a measurement. If there is no thermal exchange gas within the vessel, it takes quite long time to reach a thermal equilibrium state, and of course, a measurement can not be carried out. In the manner of sealing with gold plate, a special vacuum chamber with an arm for driving the screw top is needed for introducing helium gas. After putting a sample in the vessel, a gold plate and the screw top are simply put on the mouth of the vessel and then the vessel is placed inside the

vacuum chamber. Next, the inside of the chamber and the vessel is evacuated to ~ 2.5×10^{-3} Pa. After that, a small amount of helium gas is introduced into the chamber and the vessel. Finally, the screw top is driven with the arm and the vessel can be sealed. For the same reason as a gold plate, nominally the amount of the introduced helium gas should be the same every time. However, the contribution of a necessary and sufficient amount of helium gas to total heat capacity is negligibly small. For example, in the heat capacity measurement of the empty calorimeter vessel, helium gas is introduced at 3 kPa at room temperature. Assuming that the helium gas behaves as the ideal gas, the heat capacity at constant volume C_V of helium gas is the constant value of $3nR/2$ from 5 K up to 6000 K, where $n = pV/RT$ is molar amount. Thus C_V of the introduced helium gas can be rewritten by $3pV/2T$. In the present case, as p ~ 3 kPa, V ~ 2×10^{-6} m^3, and T ~ 300 K, it is finally obtained that C_V ~ 3×10^{-5} JK^{-1}, and its contribution to the heat capacity of the vessel is 0.1, 0.05, 0.004, 0.002, and 0.001 % at 13, 20, 50, 100, and 300 K, respectively. When a sample is put into the vessel, of course dead space inside the vessel decreases. Therefore, the introducing pressure of helium gas should be increased according to the volume of the dead space. However, a little fluctuation of the amount of introduced helium gas does not affect measured heat capacity data so much as explained above. In many cases of a solid sample, i.e., powder, ceramics, and single crystals, the vessel can not be completely filled with a sample even if it seems to be completely filled. Thus it is usually considered for convenience that a half of the vessel is filled with a sample, and helium gas is introduced at 5 ~ 6 kPa at room temperature, which is as twice as the case of the empty vessel.

In order to start sample measurements, it is necessary to measure the heat capacity of the calorimeter vessel. The measurement was carried out between 13 and 420 K with ΔT of 0.5 K from 13 to 80 K, 0.75K from 80 to 120 K, and 1 K from 120 to 420 K. Small ΔT values provide accurate heat capacity values and a large number of data help to fit the data with polynomials by the least-square method. The measured heat capacity of the calorimeter vessel is shown in Fig.2.6(a). Since the heat capacity of a sample is obtained by subtracting that of the vessel from total heat capacity, it is necessary to smooth and interpolate the heat capacity data of the vessel. The heat capacity data are divided into some divisions, where neighboring divisions are partially overlapping with each other, and the data in each division are fitted with a suitable polynomial by the least-square method. Neighboring two polynomials are connected in their overlapped region using the following weighting cosine function:

$$f=\left(\frac{1}{2}\cos(\pi x)+\frac{1}{2}\right)f_i(x)+\left(-\frac{1}{2}\cos(\pi x)+\frac{1}{2}\right)f_{i+1}(x),\quad x=\frac{T-T_i}{T_{i+1}-T_i}. \tag{2.3}$$

where f_i is the i-th polynomial, T_{i+1} is the minimum temperature of (i+1)-th region, and T_i is the maximum temperature of i-th region. A function smoothed in this manner is continuous as far as a first-order derivative. This smoothing method was designed by O. Fujishima, who was

a master student in this laboratory. Fig.2.6(b) shows the relative deviations of the measured data from the smoothing function. The deviations are within $\sim \pm 0.1$ % over the whole measurement temperature range, which suggest the high precision of this calorimeter. The enthalpy of the vessel is derived by integrating this smoothing function at 0.01 K intervals using quadrature by parts over the whole measurement temperature range. The derived enthalpy values are tabulated as a function of temperature and inserted into an automatic measurement program. Thus, sample heat capacity can be obtained using Eq.(2.2).

Since the vessel is miniaturized, it is possible to measure heat capacity even with a small sample of ~ 1 g. However, a large piece of a solid sample can not be put into the vessel because there is the sheath right under the mouth. This is the worst demerit of this calorimeter vessel.

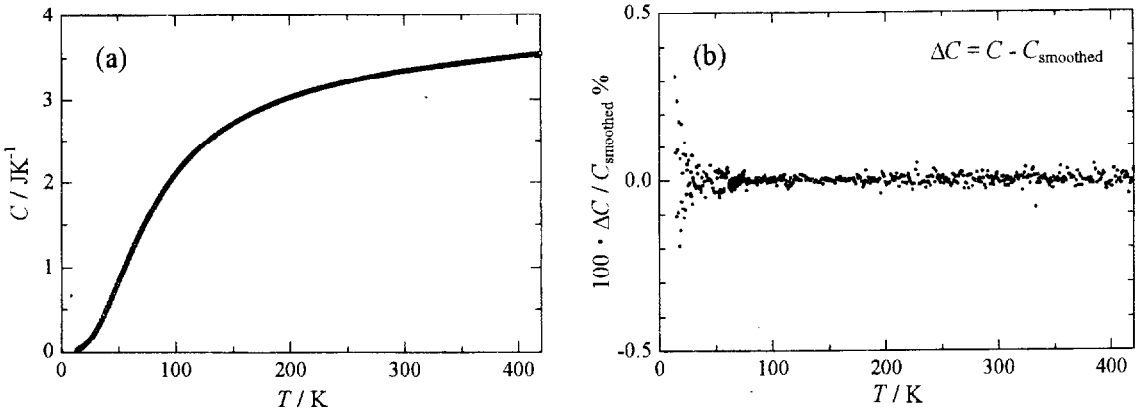

Fig. 2.6. (a) Measured heat capacity of the calorimeter vessel and (b) its deviation from the smoothed values obtained using Eq.(2.3) for fitting polynomials in the least-square fitting to the measured data.

Measurement System

The heat capacity measurement system is mainly composed of three systems, i.e., the adiabatic control system, the temperature measurement system, and the energy measurement system. Fig.2.7 shows a block diagram of the measurement system. The temperature and energy measurement systems are operated in compliance with a command from the host computer, in which the homemade automatic measurement program is installed. On the other hand, the adiabatic control system is completely independent of other systems.

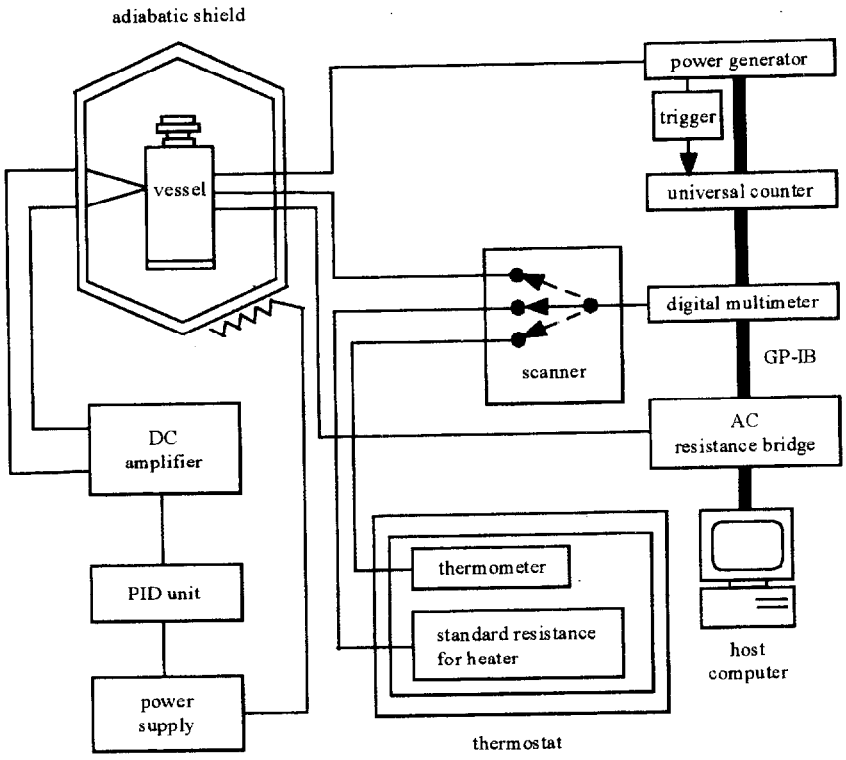

Fig. 2.7. Block diagram of the heat capacity measurement system of the adiabatic calorimeter.

The adiabatic control method is the negative feedback method where the temperature difference between the calorimeter vessel and the top shield is immediately detected by the thermocouple, and the power supplied to the shield is adjusted to extinguish the temperature difference. The signal of the thermocouple is amplified with the DC amplifier (Micro-voltmeter AM-1001B, Okura Electric Co., Ltd.) and then transmitted to the digital PID controller (DB1000F, Chino Corp.), which is the brain of the adiabatic control system. This digital PID controller generates an output signal according to the magnitude, duration, and

changing rate of the signal of the thermocouple. According to the output signal from the digital PID controller, the DC stabilizing power supply (PR36-1.2A, Kenwood TMI Corp.) supplies power to the heater of the adiabatic shield. Each component of the adiabatic control unit is also controlled in the same manner, but temperature difference is made on purpose between the top shield and the inner ring, and between the inner and outer rings as already explained. Like this, the adiabatic control is not absolute but relative. Therefore, if the same amount of heat leaks out from the vessel and the adiabatic shield simultaneously, the temperature of the vessel continues to decrease even though the adiabatic shield is regularly controlled. In fact, such situation is not unusual because it is quite difficult to establish a complete adiabatic state experimentally, and the situation strongly depends on various external conditions, e.g., the residual amount of coolant (especially at low temperatures below 100 K), radiation (especially at high temperatures above 300 K), and the temperature-dependent sensitivity of the thermocouples. Thus, in order to make the situation better, the adiabatic control condition should be changed according to these external conditions. Actually, the adiabatic control condition can be changed using zero-point correction of the DC amplifier for the thermocouple between the vessel and the top shield. In other words, the extra power supplied to the adiabatic shield is adjusted according to the external conditions using the zero-point correction. This adjustment should be done in the middle of heating process because each temperature is calculated at this point (see Fig.2.2). In this way, a temperature drift rate can be kept within $\pm 1.0 \times 10^{-5}$ K/min.

Temperature measurement is performed by measuring the resistance of the thermometer mounted on a vessel using the AC resistance bridge (5840D, H. Tinsley & Co. Ltd.), where the internal standard resistance is used for determining the resistance value of the thermometer. In a temperature-measurement period, the resistance is measured at 30 s intervals and a measured resistance value is converted to temperature according to the calibrating equation given in the certificate of the thermometer, which is inserted into the automatic measurement program.

Energy measurement system is composed of the digital multimeter (Model 2010, Keithley Instruments, Inc.) and the universal counter (TR5822, Advantest Corp.). In the circuit for supplying power to the heater mounted on the vessel, the power supply, the heater, and the standard resistance are connected in series. The programmable DC voltage/current generator (R6144, Advantest Corp.) is employed as the power supply for the heater. The standard resistance (Type 2794, 100 Ω, Yokogawa Electric Co., Ltd.) is for measuring current and placed in the thermostatic bath, the temperature of which is kept to be 27 °C by the temperature controller (E5LD, Omron Corp.). However, the temperature of the thermostatic bath fluctuates within ± 0.5 °C, and it is measured by reading the signal of the high precision thermosensor (LM35D) using the digital multimeter at the beginning of every heating period. The precise

value of the standard resistance is determined by this temperature according to the calibrating equation, which is inserted into the automatic measurement program. In a heating period, the voltage between both edges of the heater and the standard resistance is alternately measured by the digital multimeter at 30 s intervals from 15 s later of a heating start. The heating time is measured by the universal counter, where the on/off signals of the DC voltage/current generator are the direct trigger for a start and end of the time measurement. Finally, the applied energy to the vessel including a sample is calculated by Eq.(2.1).

Performance

After the construction of an apparatus, it is necessary to check the performance. For calibrating and checking calorimeters used to measure either enthalpy or heat capacity within the range of 10 to 2250 K, the Standard Reference Material 720 (SRM720) is furnished by National Bureau of Standards (NBS) [present National Institute of Standards and Technology (NIST)], U. S. Department of Commerce. The material furnished is synthetic sapphire (α-Al_2O_3) cylinders, cut from centerless-ground rods grown by the Vernieul process. The attached certificate says as follows.

> "The enthalpy and heat capacity data have been derived from high temperature enthalpy and low temperature heat capacity measurements. The enthalpy values are accurate to ± 0.1 % from 70 to 1173 K and the heat capacity values have an accuracy ranging from ± 0.1 % at 70 K to ± 0.3 % at 1200 K, while below 70 K, the inaccuracy in heat capacity and enthalpy values increase gradually to ± 10 % at 10 K, because with decreasing temperature, the heat capacity of sapphire diminishes at a much faster rate than does that of the sample container (mainly copper)."

Thus checking the performance in a low temperature region is considered to be useless, and the heat capacity measurement on SRM720 was carried out only above 50 K.

The certificate also says that it is recommended that the material be heated to 1000 °C in air prior to heat capacity measurements below 350 K, because an occasional particle may contain an end smear due to the method employed cutting the material. Thus SRM720 was heated at 1000 °C in air before putting in the calorimeter vessel although it has been already used for checking the performance of other calorimeters in this laboratory. The amount of SRM720 used for the measurement was 3.5440 g (34.758 mmol), which was corrected for atmospheric buoyancy using the following equation:

$$m = \frac{\rho_{\text{sample}}}{\rho_{\text{sample}} - \rho_{\text{air}}} m_{\text{measured}}, \qquad (2.4)$$

where m and $m_{measured}$ are the true and measured mass of a sample, respectively, and ρ_{sample} and ρ_{air} are the density of a sample and dry air, respectively. The density of α-Al_2O_3 is 3.97 g/cm^3, which is given in the certificate. The density of dry air is estimated by the following equation:

$$\rho_{air} = \frac{0.0012932}{1+0.00367(T/\mathrm{K}-273.15)} \cdot \frac{p}{101325/\mathrm{Pa}}. \tag{2.5}$$

The mass difference before and after the correction was 0.03 %.

The result of heat capacity measurement is shown with the data given by NBS in Fig.2.8(a). It seems that there is no so much difference between both data in the full-scaled figure but slight difference should be discussed in relative deviation. The relative deviation of the present data from the NBS data is calculated and shown in Fig.2.8(b). It shows a little bit strange temperature-dependence: decreasing from 100 to 250 K, showing a minimum of −0.4 % at 250 K, increasing to 330 K, and showing a constant of −0.2 % up to 420 K. On the whole the measured data are less than the NBS data, which implies extra heat inflow from the adiabatic control unit to the vessel in a heating process. Although it might be necessary to check the performance again after altering the adiabatic control setting, e.g., the temperature-difference between the first and second adiabatic control units, at this stage it can be concluded that the accuracy of this calorimeter is 0.1, 0.3, and 0.2 % at 100, 200, and above 300 K, respectively.

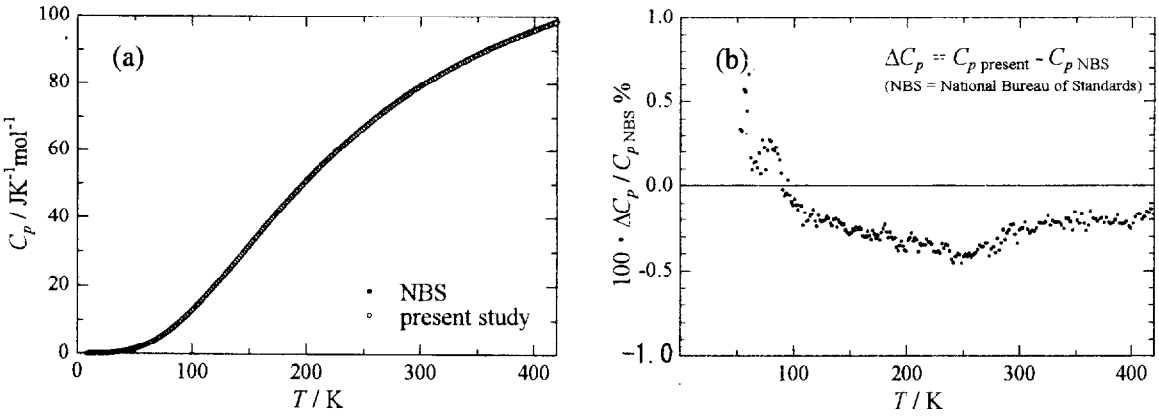

Fig. 2.8. (a) Heat capacity of SRM720 measured by the adiabatic calorimeter constructed in the present study with that provided by National Bureau of Standards (NBS), U. S. Department of Commerce, and (b) deviation of the present result from the data of NBS.

2.3. Heat Capacity Measurements by a Relaxation Method

2.3.1. Principle

A relaxation method is the method that has been mainly developed for very low temperature heat capacity measurements. In the conventional relaxation method **[5]**, the thermal system shown in Fig.2.9(a) is considered. The sample is mounted on the sample platform that has the thermometer and the heater. It is assumed that the sample and the sample platform are in good thermal contact with each other and forming the unit with the same temperature T. The heat capacity of this unit C_{total} is assumed to be constant during the measurement with a small temperature rise ΔT. The sample platform is connected with the thermal bath by thermal media (electrical and thermal lead wires), where the temperature T_b of the thermal bath is kept to be constant during the measurement and the thermal conductance K_w of the lead wires is already known. In addition, it is also assumed that the energy applied to the unit diffuses only toward the thermal bath through the lead wires. At this time, the system is in a thermal equilibrium state, and the unit temperature T is the same as T_b. Under this condition, the constant power P_0 is applied to the unit during the heating period and the unit temperature T is measured as a function of time t (Fig.2.10(a)), which obeys the equation

$$C_{\text{total}} \frac{dT}{dt} = -K_w(T(t) - T_b) + P(t), \tag{2.6}$$

where $P(t)$ is the power applied by the heater, which is equal to P_0 during the heating period and equal to zero during the cooling period. The solution of this equation is given by exponential functions with a characteristic time-constant τ equal to C_{total}/K_w. Thus, the total heat capacity can be obtained as $C_{\text{total}} = K_w\tau$. In order to obtain the heat capacity of the sample C_{sample}, the heat capacity of the platform alone C_{platform} must be measured in advance. After that, the heat capacity of the sample can be obtained as $C_{\text{sample}} = C_{\text{total}} - C_{\text{platform}}$.

When the thermal contact between the sample and the platform is very good and the thermal diffusion is rapidly achieved inside of the sample, e.g., in metals, heat capacity can be obtained with high accuracy by a conventional method. However, in the cases that the thermal contact between the sample and the platform is poor or that the thermal diffusion is not readily accomplished inside of the sample, a temperature-difference is produced between both, and the thermal relaxation process does not simply obey Eq(2.6) (Fig.2.10(b)). Recently, considering the thermal system shown in Fig.2.9(b), a more sophisticated method has been developed, where taking into account not only thermal relaxation process from the platform to the thermal bath (external relaxation process) but also from the platform to the sample (internal relaxation process) **[6]**. The following equations express each relaxation process:

$$C_{\text{platform}} \frac{dT_p}{dt} = P(t) - K_w\left(T_p(t) - T_b\right) + K_g\left(T_s(t) - T_p(t)\right) \tag{2.7}$$

$$C_{\text{sample}} \frac{dT_s}{dt} = -K_g\left(T_s(t) - T_p(t)\right), \tag{2.8}$$

where C_{platform} is the heat capacity of the sample platform, C_{sample} is the heat capacity of the sample, and K_g is the thermal conductance between the sample and the sample platform, which is usually due to grease. $T_p(t)$ and $T_s(t)$ is the temperatures of the platform and the sample, respectively. In these equations, the measurable quantities are $P(t)$, $T_p(t)$ and T_b. In this method, utilizing a nonlinear least-square fitting algorithm for these measurable quantities, the heat capacity of the sample can be determined with high accuracy [6], especially at low temperatures.

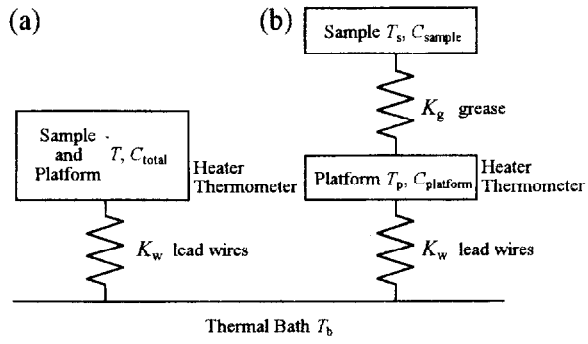

Fig. 2.9. Thermal system considered in the heat capacity measurements by a thermal relaxation methods: (a) conventional model and (b) more sophisticated model.

In both conventional and sophisticated relaxation methods, since it is assumed that the energy applied to the sample and the platform diffuses only toward the thermal bath through the lead wires, the accuracy becomes low in a high temperature region where the heat leak due to the radiation is not negligible. In addition, since it is also assumed that the thermal relaxation process can be described by exponential functions, it is difficult to determine accurately the heat capacity of the sample that shows the thermal relaxation process remarkably deviating from this model, e.g., a glass former. In the case of a first-order phase transition, it is impossible in principle to measure the heat capacity because of latent heat, which diminishes the signal of the temperature rise due to the applied energy. Even if the latent heat is not so large, the supercooling phenomenon takes place in the thermal relaxation process, and the accurate heat capacity value can not be obtained. Thus, when some heat capacity anomaly is observed, the closest attention should be paid for the evaluation of the data.

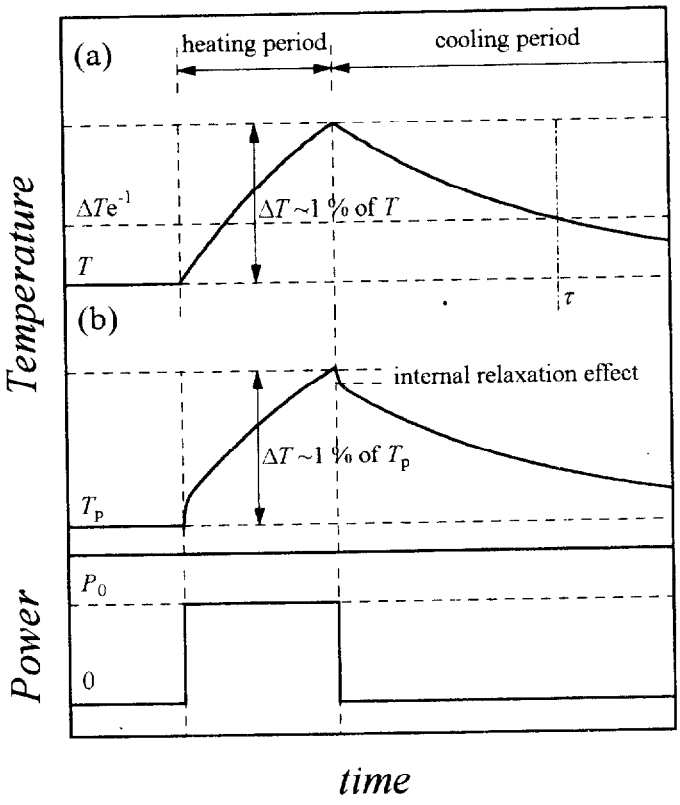

Fig . 2.10. Expected thermal relaxation process, i.e., the time-dependence of the temperature after the power is applied to the thermal system shown in Fig. 2.9, and (a) and (b) in this figure correspond to those in Fig. 2.9. In the case of (a), the relaxation process can be characterized by a single relaxation time, i.e., the external relaxation time, while in the case of (b), it can not be well described by the conventional model, because an internal relaxation effect is observed. In this case, it is characterized by two relaxation time, i.e., the internal relaxation time besides external one, and can be described by the sophisticated model.

2.3.2. Apparatus

The apparatus for the heat capacity measurement by a thermal relaxation technique has been manufactured by Quantum Design Inc. as a Physical Property Measurement System (PPMS). Using this apparatus, it is possible to measure the heat capacity between 2 and 320 K with a small sample of ~ 1 mg with relatively high accuracy of ~ 1 %. However, the sample is restricted to a solid with a ceramic or single crystal form. Although it is not impossible to

measure a powder sample if it is tightly pressed into a pellet, the accuracy might become low because the effect of slow thermal diffusion inside of the sample can not be neglected. Thus, even in the case of a ceramic or single crystal, the sample should be thinned and its surface contacting to the sample platform should be polished as smoothly as possible. The schematic view of the thermal system of PPMS is shown in Fig.2.11. The heater and the thermometer are attached to the bottom side of the sample platform. Small electrical lead wires for the heater and the thermometer provide the thermal connection between the platform and the thermal bath and structural support for the platform. The sample is mounted on the platform using a thin layer of grease (Apiezon N or H), which provides the thermal contact between the sample and the platform. The surroundings of the system are evacuated by a turbo-molecular pump to provide a sufficient vacuum ($\sim 2.5 \times 10^{-4}$ Pa) so that the thermal conductance between the sample platform and the thermal bath is completely dominated by the conductance of the wires. In addition, multi-radiation shield is equipped over the system in order to reduce the effect of the radiation.

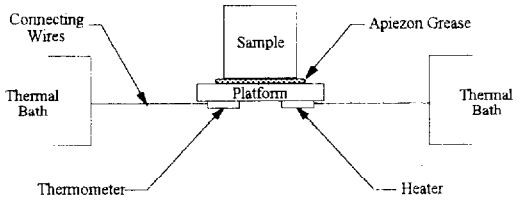

Fig. 2.11. Schematic view of the sample puck of PPMS, which is general one for the heat capacity measurements by a thermal relaxation technique.

Prior to the sample measurement, it is necessary to measure the addenda composed of the sample platform and the grease every time, as the amount of grease changes every time. PPMS adopts Eq.(2.6) for the addenda measurement. For the sample measurement, Eqs.(2.7) and (2.8) are basically adopted where $C_{platform}$ is already known to be the addenda heat capacity, but Eq.(2.6) is also adopted when the internal relaxation effect is negligible. The measurement can be performed on both heating and cooling but there should be no difference between both runs as the measurement procedure is the same at each temperature. If some difference is observed, it implies the existence of some anomaly or significant experimental error. In PPMS, it is possible to set up the various experimental conditions. Among these, the relative magnitude of the temperature rise ΔT to the platform temperature, i.e., the magnitude of the

applied power, is especially important because it strongly affect the resultant heat capacity data. If ΔT is small relative to T_p, a signal-to-noise ratio in a thermal relaxation process increases, which leads to a significant experimental error. On the other hand, if ΔT is large, the assumption that C_{total} (= $C_{platform}$ + C_{sample}) is constant for ΔT is not approved any longer. Thus, ΔT is usually selected to be ~1 % of T_p below 100 K and 1 K above 100 K.

The measurement system of PPMS is completely automated. Because of the good performance and convenience, PPMS has come into wide use recently. However, there are many points to notice in order to use PPMS correctly. Although the detailed explanation can not be given for a commercial apparatus, only these points to notice are explained here. Fig.2.12(a) shows the heat capacity data of $NaNO_2$ measured using the adiabatic calorimeter (circles) and PPMS (triangles). In the measurement using PPMS, the thermal contact between the sample and the sample platform is very important. However, the measurement program provides specious data (black and gray triangles in Fig.2.12(a)) even if the thermal connection is insufficient to determine the heat capacity values. In case of $NaNO_2$, the thermal expansion coefficient of the sample seemed to be very different from those of the Apiezon N grease and the sample platform, and the sample peeled off from the sample platform due to abrupt cooling down from room temperature. Thus, when the sample was very slowly cooled down, the measured heat capacity data agreed with those measured by an adiabatic method. As expected from this example, it is also necessary to pay attention to a change in quality of the grease used as the thermal medium. Fig.2.12(b) shows the heat capacity of ferroelectric $Pb(Sc_{1/2}Ta_{1/2})O_3$ (PST) around the ferroelectric phase transition measured using the adiabatic calorimeter (circles) and PPMS (triangles). The ferroelectric phase transition in PST is of first-order, and it is impossible in principle to measure the heat capacity of a first-order phase transition by a thermal relaxation technique. However, the measurement program of PPMS also provides specious data, which are quite different from those measured by an adiabatic method while a relatively good agreement can be seen apart from the phase transition points. In such a case, it is never allowed to discuss the data quantitatively. As demonstrated by these examples, the closest attention should be paid for the evaluation of the data measured by a thermal relaxation technique. In this respect, the ability to obtain the data by an adiabatic method is the best strength in the heat capacity investigations.

In this study, PPMS was used in order to obtain the data below 13 K, which can not be measured using the adiabatic calorimeter. Moreover, in the case that only a small sample was available, PPMS was also used between 2 and 300 K.

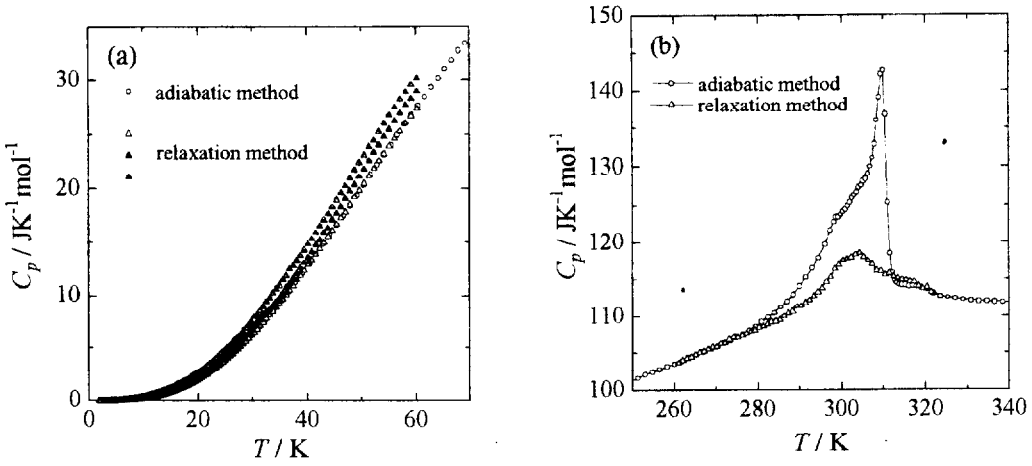

Fig. 2.12. Examples showing the points to notice for the heat capacity measurements by a thermal relaxation technique: (a) heat capacity of $NaNO_2$ single crystal measured by an adiabatic method and a relaxation method, and (b) that of ferroelectric $Pb(Sc_{1/2}Ta_{1/2})O_3$ (PST). In the case of $NaNO_2$, because of a large difference in thermal expansion between the sample and the sample platform including grease, the sample often peel off from the sample platform, and it is impossible to obtain the correct value of the heat capacity (triangles in (a)). However, taking care of a cooling rate before starting a measurement, good data can be obtained, which is in good agreement with that obtained by adiabatic calorimetry. On the other hand, ferroelectric PST shows a first-order ferroelectric phase transition, the heat capacity of which can not be measured correctly by a relaxation method in principle. Thus, it is necessary to take care of treating the data when some anomaly is observed in the heat capacity measured by a relaxation method.

2.4. Dielectric Constant Measurements

2.4.1. Principle

When the external electric field is applied to a dielectric material, the dielectric constant (or permittivity) is defined as the constant in the linear relationship between the external electric field $\boldsymbol{E}$ and the internal electric flux density $\boldsymbol{D}$:

$$\boldsymbol{D} = \varepsilon\varepsilon_0\boldsymbol{E} = \varepsilon_0\boldsymbol{E} + \boldsymbol{P}, \tag{2.9}$$

where $\boldsymbol{P}$ is the macroscopic polarization, and ε_0 is the dielectric constant of the vacuum. For a field fluctuating in time and space, e.g., the AC field, the polarization can not follow the fluctuation of the field immediately, and the consequent fluctuation of the electric flux density shows a delay. This delay is caused by various reasons, e.g., the weak electronic or ionic conduction, the resistance against ionic vibration, and the orientational relaxation of dipoles, which result in the energetic loss within a dielectric material. In this case, the dielectric constant is represented by the complex number:

$$\boldsymbol{D} = (\varepsilon' + i\varepsilon'')\varepsilon_0\boldsymbol{E}_0\,\mathrm{e}^{-i\omega t} = \dot{\varepsilon}\varepsilon_0\boldsymbol{E}_0\,\mathrm{e}^{-i\omega t}, \tag{2.10}$$

where $\boldsymbol{E}_0$ and ω are the amplitude and the angular frequency of the AC electric field, respectively. The real and imaginary parts of the complex dielectric constant represent the dielectric constant and the dielectric loss, respectively. Letting δ denote the deviation angle from the real axis in the complex plane, the dielectric constant and loss are represented by

$$\begin{cases} \varepsilon' = |\dot{\varepsilon}|\cos\delta \\ \varepsilon'' = |\dot{\varepsilon}|\sin\delta \end{cases} \quad \therefore \varepsilon' + i\varepsilon'' = |\dot{\varepsilon}|(\cos\delta + i\sin\delta) = |\dot{\varepsilon}|\mathrm{e}^{i\delta}, \tag{2.11}$$

where $|\dot{\varepsilon}|$ is the absolute value of the complex dielectric constant. Thus Eq.(2.10) can be rewritten as

$$\boldsymbol{D} = |\dot{\varepsilon}|\mathrm{e}^{i\delta}\,\varepsilon_0\boldsymbol{E}_0\,\mathrm{e}^{-i\omega t} = |\dot{\varepsilon}|\varepsilon_0\boldsymbol{E}_0\,\mathrm{e}^{-i(\omega t-\delta)}. \tag{2.12}$$

This equation means that the fluctuation of the electric flux density shows a delay of phase δ to that of the electric field. The phase δ is called the loss angle, and the following relation is derived from Eq.(2.11):

$$\tan\delta = \varepsilon''/\varepsilon'. \tag{2.13}$$

This factor is called the dielectric loss tangent. Since it is desired for a practical dielectric material to have large dielectric constant and small dielectric loss, the dielectric loss tangent is an important factor in the quality evaluation of a dielectric material.

On the other hand, the electrostatic capacity C of a parallel-plate capacitor consisting of a dielectric material with the dielectric constant ε is written by

$$C = \frac{\varepsilon\varepsilon_0 S}{d}, \tag{2.14}$$

where S and d are the square of a plate and the distance between parallel plates, respectively. When the AC electric field with the angular frequency ω is applied to this capacitor, the impedance $Z = R - iX_C$ is ideally equal to the capacitive reactance X_C (= $1/\omega C$), because there is no resistance R in the ideal capacitor. However, there is loss in real materials as mentioned above, and the capacitor should be considered as the equivalent circuit that consists of the resistance and the reactance. The simplest equivalent circuit consists of a single resistance and a single reactance, and there are series and parallel equivalent circuits. The simplest equivalent circuits for the capacitor are shown in Table 2.1. In the case of the series equivalent circuit, there is a following relation to the loss tangent:

$$\tan\delta = -R/X_C \ . \tag{2.15}$$

On the other hand, in the case of the parallel equivalent circuit, it is convenient to employ the admittance $Y = G + iB_C$, which is the reciprocal of the impedance Z, where G (= $1/R$) is the conductance and B_C (= $1/X_C$) is the capacitive susceptance. There is the following relation to dielectric loss tangent:

$$\tan\delta = G/B_C \ . \tag{2.16}$$

It is entirely arbitrary to select which equivalent circuit to use for the measurement. However, in the case that the same capacitor is measured under the same condition, the measured value in the series equivalent circuit is usually different from that in the parallel equivalent circuit. This difference is closely related to the loss tangent of the capacitor, and the measured values in each circuit are connected with each other by the loss tangent (Table 2.1).

equivalent circuit	dielectric loss tangent	converting to the other circuit
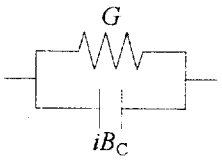	$\tan\delta = \dfrac{G}{\omega C_{\text{parallel}}}$	$C_{\text{series}} = (1+\tan^2\delta)C_{\text{parallel}}$ $R = \dfrac{\tan^2\delta}{1+\tan^2\delta}\cdot\dfrac{1}{G}$
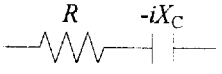	$\tan\delta = -\omega C_{\text{series}} R$	$C_{\text{parallel}} = \dfrac{1}{1+\tan^2\delta} C_{\text{series}}$ $G = \dfrac{1}{1+\tan^2\delta}\cdot\dfrac{1}{R}$

Table 2.1. Relation between the measured impedance parameters in the series and parallel equivalent circuits. C_{series} and C_{parallel} are the series and parallel equivalent capacitance, respectively.

In many cases, the parallel equivalent circuit is adopted for the dielectric constant measurement. The dielectric constant and loss can be calculated by following equations, respectively:

$$\begin{cases} \varepsilon' = \dfrac{B_C d}{\omega \varepsilon_0 S} \\ \varepsilon'' = \varepsilon' \tan\delta = \dfrac{\varepsilon' G}{B_C} = \dfrac{Gd}{\omega \varepsilon_0 S} \end{cases} \tag{2.17}$$

Therefore, the dielectric constant and loss of a sample can be obtained by measuring G and B_C of the parallel-plate capacitor made of a sample.

2.4.2. Measurement System

According to the measurement temperature range, two different measurement systems were used, but the difference between the two is the difference in cryostats, and there is no difference in the basic structures. The block diagram of the measurement system is shown in Fig.2.13. The measurement system is mainly composed of the impedance measurement device, the temperature measurement device, and the temperature control system. The impedance measurement device and the temperature measurement device are operated in compliance with the command of the host computer, in which the homemade automatic measurement program is installed. On the other hand, the temperature control system is independent from the other devices.

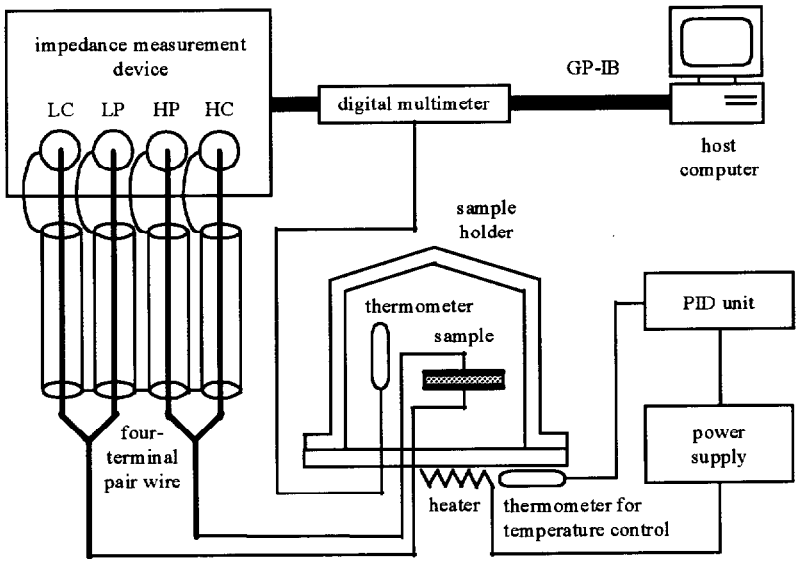

Fig. 2.13. Block diagram of the dielectric constant measurement system.

In the system for the low temperature measurement between 15 and 320 K, the sample holder made of copper is equipped with the helium compression refrigerator (CryoMini Compressor, Iwatani CryoTechno Corp.). The sample is mounted on the sample holder and then the holder is covered with the holder lid of stainless steel. After evacuating the inside of the sample holder, helium gas (100 kPa at room temperature) is introduced for the thermal exchange. The sample holder is covered with the radiation shield of stainless steel, and then the radiation shield is covered with the outer jacket of stainless steel, the inside of which is evacuated by an oil rotary pump during the measurement. The temperature of the holder is controlled by the programmable digital PID controller (Model KP, Chino Corp.), in which the arbitrary automatic temperature control program can be installed according to the purpose. This controller generates an output signal according to the reference signal of the thermometer for the temperature control attached to the bottom side of the sample holder. According to the output signal from the digital PID controller, the regulated DC power supply (Model PAB32-2A, Kikusui Electronic Corp.) supplies power to the heater of the sample holder. On the other hand, in the system for the high temperature measurement between 100 and 420 K, the sample holder made of copper is suspended in midair and multi-radiation shield is equipped over the sample holder. The sample holder and the radiation shield are covered with the jacket of Pyrex glass®, the inside of which is filled with helium gas (100 kPa at room temperature) after evacuated. The jacket is covered with a liquid nitrogen Dewer vessel, the inside of which is filled with liquid nitrogen during the measurement on cooling while is empty on heating. The temperature of the holder is also controlled by the programmable digital PID controller (KP1000, Chino Corp.) and the regulated DC power supply (PD35 10D, Kenwood TMI Corp.) in the same manner as in the low temperature measurement system.

The devices employed for each measurement system are tabulated in Table 2.2. In each measurement system, the corresponding devices are different, but there is no large difference in the basic performance between these devices. The conductance and the susceptance of the sample are measured by the four terminal-pair method in the parallel equivalent circuit mode using the impedance measurement device. Temperature measurement is performed by measuring the resistance of the Pt-Co resistance thermometer or the thermoelectromotive force of the type-E thermocouple mounted next to the sample using the digital multimeter. The measured value of the resistance or the thermoelectromotive force is converted to temperature according to the calibrating equation, which is inserted into the automatic measurement program. Since temperature is usually changing at a constant rate during the measurement (of course it is also possible to control at a constant temperature), temperature is measured before and after the impedance parameter measurement and then averaged.

cryostat	impedance measurement device	temperature measurement device	thermometer	temperature controller
low temperature 15 ~ 320 K	Model 4284A Precision LCR Meter (Hewlett-Packard Inc.)	Model 3748A Multimeter (Hewlett-Packard Inc.)	Pt-Co resistance thermometer	Model KP (Chino Corp.)
high temperature 100 ~ 420 K	Model 4192A LF Impedance Analyzer (Hewlett-Packard Inc.)	182 Sensitive Digital Voltmeter (Keithley Instruments, Inc.)	type-E thermocouple	KP 1000 (Chino Corp.)

Table 2.2. Employed devices for the dielectric constant measurement systems. The corresponding devices have a similar performance, and there is no large difference between both.

References

[1] Y. Ogata, K. Kobayashi, T. Matsuo, and H. Suga, *J. Phys.* **E17**, 1054 (1984).

[2] T. Atake, H. Kawaji, A. Hamano, and Y. Saito, *Rep. Res. Lab. Eng. Mater., Tokyo Inst. Tech.* **15**, 13 (1990).

[3] T. Tanaka, T. Atake, H. Nakayama, T. Eguchi, K. Saito, and I. Ikemoto, *J. Chem. Thermodyn.* **26**, 1231 (1994).

[4] F. Grønvold, *Acta Chem. Scand.* **21**, 1695 (1967).

[5] R. Bachmann, F. J. DiSalvo, Jr., T. H. Geballe, R. L. Greene, R. E. Howard, C. N. King, H. C. Kirsch, K. N. Lee, R. E. Schwall, H. U. Thomas, and R. E. Zubeck, *Rev. Sci. Instrum.* **43**, 205 (1972).

[6] J. S. Hwang, K. J. Lin, and C. Tien, *Rev. Sci. Instrum.* **68**, 94 (1997).

Chapter 3

$BaTiO_3$, $PbTiO_3$, and $PbZrO_3$

Typical Perovskite Ferro- and Antiferroelectrics

—— Features in their Heat Capacity

3.1. Introduction

Barium titanate, $BaTiO_3$, and lead titanate, $PbTiO_3$, are the representative perovskite ferroelectrics, and lead zirconate, $PbZrO_3$, is the representative perovskite antiferroelectric. The phase transition behavior of these representatives is already mentioned in *Chapter 1*. In spite of the long history, little heat capacity measurements over a wide temperature range has been made for these perovskites, especially $PbTiO_3$ and $PbZrO_3$, although it has been made in a narrow temperature range such as very low temperatures **[1-4]** and a phase transition region by an AC method **[5]** or DSC **[6]**. A small number of heat capacity measurements are presumably due to the indifference to regions without a phase transition and the difficulty of a qualitative heat capacity measurement especially at high temperatures. However, heat capacity below room temperature contains much information about an energetic state of the system such as lattice vibrational excitation process even if there is no phase transition, and in many cases, such information is directly related to characteristics of substances. In addition, it is difficult to obtain quantitative heat capacity data by an AC method and DSC, and in order to obtain accurately the thermodynamic quantities concerning a phase transition, it is necessary to employ an apparatus with high accuracy.

In this chapter, the heat capacity of these typical perovskite (anti)ferroelectrics is considered in detail and the features in their heat capacity are specified. The heat capacity of $BaTiO_3$ has been already measured by an adiabatic method between 8 and 310 K by Hamano *et al.* **[7]**, and between 50 and 300 K by Todd *et al.* **[8]**. However, the present measurement was carried out between 13 and 420 K using the newly constructed adiabatic calorimeter. Thus the data between 300 and 420 K was newly obtained and all of the heat capacity anomalies caused by the three phase transitions in $BaTiO_3$ could be caught by an adiabatic method. On the other hand, the phase transitions in $PbTiO_3$ and $PbZrO_3$ are at a much higher temperature than the upper limit temperature of the present measurements, 420 K, and of course the heat capacity

anomaly caused by the phase transitions can not be caught. However, the absence of phase transitions in these lead-based perovskites below 420 K is rather favorable to the present objective: the heat capacity of $PbTiO_3$ and $PbZrO_3$ below 420 K must consist purely of the lattice contribution. $Pb(Mg_{1/3}Nb_{2/3})O_3$, $Pb(Mg_{1/3}Ta_{2/3})O_3$, and $Pb(Sc_{1/2}Ta_{1/2})O_3$ relaxors show a dielectric anomaly below room temperature, and if there is certain singularity in their heat capacity corresponding to the dielectric anomaly, it is possible to extract the singularity by comparing their heat capacity with the pure lattice contribution in the compounds with the same crystal structure and ionic kinds. Thus the heat capacity of $PbTiO_3$ and $PbZrO_3$ was measured between 2 and 420 K by an adiabatic and relaxation method.

3.2. Experimental

3.2.1. Sample Preparation

$BaTiO_3$ [7]

The powder sample of $BaTiO_3$ used for the present measurement was synthesized by melt-solidification method by Hamano [7] in this laboratory about 15 years ago. Thus, only this substance is not synthesized in this study, but the method of synthesis is mentioned here. Powder materials of $BaCO_3$ (Rare Metallic Co., Ltd., 99.99 %) and TiO_2 rutile (do., 99.99 %) in the stoichiometric proportions were mixed in an alumina mortar with ethanol media for 1h. This powder mixture was pressed into pellets at 80 MPa. These pellets were put into a platinum crucible and then heated preliminarily at 1200 °C for 12 h. After that, the materials were melted at 1630 °C for 10 min, and melt-solidified sample of $BaTiO_3$ was obtained, where a slight formation of hexagonal-type was confirmed. To transform the hexagonal to cubic-type, the materials were annealed at 1200 °C for 12 h. Finally, the materials identified to be a single phase of cubic-type $BaTiO_3$ by powder X-ray diffraction, and no evidence for the phase transition of hexagonal-type of $BaTiO_3$ was obtained by DTA and dielectric measurements.

$PbTiO_3$

The single crystals of $PbTiO_3$ were prepared by PbO-flux method. The single crystal of $PbTiO_3$ is more easily synthesized than the other lead-based perovskites. The synthesis was carried out basically according to the procedure reported by Remeika et al. [9]. Powder materials of TiO_2 rutile (Rare Metallic Co., Ltd., 99.99 %) and PbO (do., 99.99 %) were mixed in the mass ratio of 1:10. This powder mixture was put into a platinum crucible, and then the crucible was covered with a platinum lid. This crucible was placed in the furnace. The

crucible was rapidly heated in an oxygen atmosphere up to 1100 °C. In order to dissolve TiO_2 in PbO-flux, the crucible was soaked at this temperature for 5 h. After that, in order to promote crystallization of perovskite $PbTiO_3$, the crucible was slowly cooled down to 700 °C at the rate of 5 °C/h, and then brought to room temperature by turning off the furnace. The flux was dissolved by 30 % hot nitric acid and the single crystals were isolated. The crystals have the size of about 5 mm and brownish yellow color. The crystal structure of was identified to be tetragonal perovskite structure (*P4mm*) by powder X-ray diffraction at room temperature (Fig.3.1).

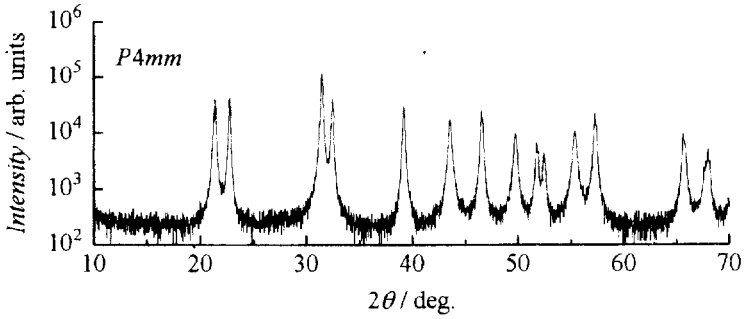

Fig.3.1. Powder X-ray diffraction pattern of $PbTiO_3$.

$PbZrO_3$

The single crystals of $PbZrO_3$ can be also prepared by PbO-flux method. However, while $PbTiO_3$ single crystals can be easily obtained, it is quite difficult to obtain a large amount of high quality $PbZrO_3$ single crystals with large size **[10,11]**. It can be seen from the phase diagrams of PbO-TiO_2 **[12]** and PbO-ZrO_2 **[13]** systems that the synthesis of $PbZrO_3$ single crystal is quite difficult compared with $PbTiO_3$. For example, even in the case that 1200 °C is chosen as a temperature to promote the solution of ZrO_2 in PbO-flux, only about 1 mol% of ZrO_2 is soluble in PbO-flux. Thus PbO-PbF_2 flux is often used to obtain a large amount of $PbZrO_3$ single crystals, but as mentioned in *Chapter 1*, the phase transition behavior is strongly affected by flux used for the synthesis: in the case of PbO-PbF_2 flux, the intermediate phase between the low and high temperature phases almost disappears, while in the case of PbO-flux, it appears more clearly **[11]**. Like this, although a large amount of $PbZrO_3$ single crystals can be obtained with PbO-PbF_2 flux, such a change in the properties due to impurity is unfavorable to a close investigation into properties of substances. However, a sample of a few grams is required for a heat capacity measurement by an adiabatic method, and it will take a great deal of labor to obtain such a large amount of $PbZrO_3$ single crystals. In fact, a sample with single crystal form is more favorable to various measurements owing to smaller specific surface area,

easier processing, clear crystallographic axes, and so on, than that with a powder or ceramic form: in the case of heat capacity measurements by an adiabatic method, only the specific surface area of a sample can be a problem because of the adsorption of thermal exchange helium gas to the sample surface at very low temperatures, but other factors do not much matter. On the other hand, in the case of lead-based compounds, it is needed to take care of the formation of lead deficiencies because of the high volatility of lead when a sample of a powder or ceramic form is prepared at a high temperature. In consideration of such circumstances, it was considered as the best way to prepare powder and ceramic samples for heat capacity measurements by an adiabatic and relaxation method, respectively.

Powder sample of $PbZrO_3$ was prepared by a solid state reaction technique. Powder materials of PbO (Rare Metallic Co., Ltd., 99.99 %) and ZrO_2 (do., 99.99 %) in the stoichiometric proportions were mixed in an alumina mortar with ethanol media for 1 h, where 3 mol% excess PbO was added to avoid lead loss in the reaction process. This powder mixture was dried in an oven and then put into an alumina Tamman crucible. The Tamman crucible plugged with kaolinite wool was placed in the furnace and then heated at 900 °C for 12 h. The structure of the resultant powder was identified to be orthorhombic perovskite (*Pbam*) by powder X-ray diffraction at room temperature (Fig.3.2). Ceramic sample was prepared for a heat capacity measurement by a relaxation method. The powder was pressed into pellets with 14 mm diameter and ~ 2 mm thickness. These pellets were sintered at 1100 °C for 1 h. Taking account of the formation of lead deficiencies in the vicinity of the surface, only the core of the sintered body was used for the measurement.

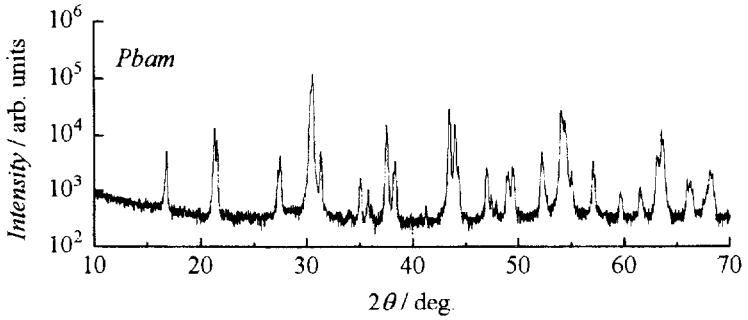

Fig.3.2. Powder X-ray diffraction pattern of $PbZrO_3$.

3.2.2. Heat Capacity Measurements

$BaTiO_3$

The heat capacity of $BaTiO_3$ was measured by an adiabatic method between 13 and 420 K, but an old-type calorimeter vessel was used only for this measurement, since this is the earliest work in this study. The amount of the sample put into the calorimeter vessel was 15.4816 g (66.390 mmol). The contribution of the sample to the total heat capacity was 18, 29, 42, 48, 58, 59, and 67 % at 13, 20, 50, 100, 200, 300, and 400 K, respectively. No deterioration of the sample was confirmed by the agreement of the present with previous data [7] between 13 and 310 K.

$PbTiO_3$

The heat capacity of $PbTiO_3$ was measured by an adiabatic method between 13 and 420 K. The amount of the sample put into the calorimeter vessel was 7.0404 g (23.231 mmol). The contribution of the sample to the total heat capacity was 38, 35, 39, 42, and 43 % at 50, 100, 200, 300, and 400 K, respectively. In order to obtain the heat capacity data below 13 K, the heat capacity was also measured between 2 and 60 K by a relaxation method. The mass of a single crystal used for the measurement was 24.536 mg (80.959 μmol). The contribution of the sample to the total heat capacity was 35, 46, 73, 87, 86, 84, 81 and 79 % at 2, 5, 10, 20, 30, 40, 50 and 60 K, respectively.

$PbZrO_3$

The heat capacity of $PbZrO_3$ was measured by an adiabatic method between 13 and 420 K using a powder sample. The amount of the sample put into the calorimeter vessel was 5.7644 g (16.640 mmol). The contribution of the sample to the total heat capacity was 65, 62, 36, 31, 33, 35 and 36 % at 13, 20, 50, 100, 200, 300, and 400 K, respectively. In order to obtain the heat capacity data below 13 K, the heat capacity was also measured between 2 and 60 K by a relaxation method using a ceramic sample. The mass of a sample used for the measurement was 18.271 mg (52.742 μmol). The contribution of the sample to the total heat capacity was 24, 54, 80, 85, 83, 80, 77 and 74 % at 2, 5, 10, 20, 30, 40, 50 and 60 K, respectively.

3.2.3. Differential Scanning Calorimetry [DSC]

Since the phase transition point of $PbTiO_3$ and $PbZrO_3$ is much higher than the upper limit temperature of the present heat capacity measurements, 420 K, the heat capacity anomaly caused by the phase transition can not be caught by the heat capacity measurement. Thus, to confirm the phase transition behavior of both compounds, DSC was carried out using Pyris 1 DSC (ParkinElmer, Inc.). Each powder sample of both compounds was put into an aluminum pan. The analyses were made between 300 and 800 K on both heating and cooling runs at the heating/cooling rate of 10 K/min. The results are shown in Fig.3.3 for $PbTiO_3$ and Fig.3.4 for $PbZrO_3$. In $PbTiO_3$, an endothermic peak caused by the ferroelectric phase transition is observed at 768 K in a heating run, and an exothermic peak is observed at 755 K in a cooling run. The transition temperature of $PbTiO_3$ estimated from these curves is 765 and 758 K in heating and cooling runs, respectively. The phase transition point in the literature **[14]** is 763 K, and it is confirmed that this sample of $PbTiO_3$ certainly undergoes a phase transition around 760 K. On the other hand, in $PbZrO_3$, an endothermic peak caused by the antiferroelectric transition is observed at 507 K in a heating run, while two exothermic peaks are observed at 504 and 495 K in a cooling run. Taking into account the previous reports on the phase transition behavior of $PbZrO_3$ **[11,15-18]**, it can be considered that the larger peak at 504 K corresponds to the cubic-rhombohedral phase transition, and the smaller peak at 495 K corresponds to the rhombohedral-orthorhombic phase transition, which is more clearly seen in the inset of Fig.3.4. Considering the difference in the phase transition behavior between both runs, the present results are consistent with the previous report on the dielectric constant

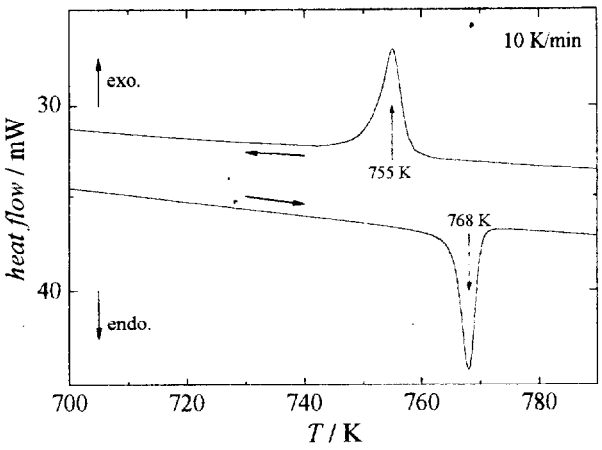

Fig.3.3. DSC data for $PbTiO_3$.

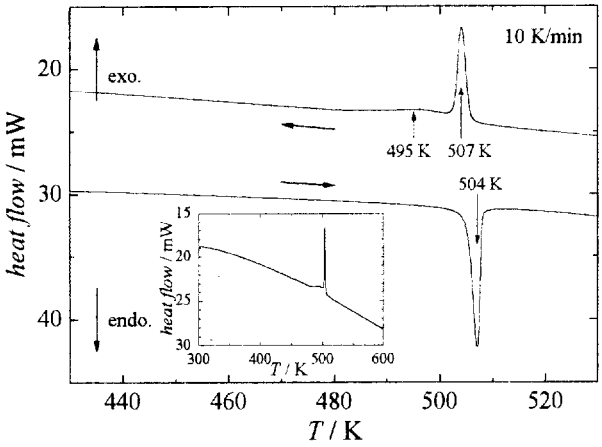

Fig.3.4. DSC data for $PbZrO_3$.

measurements for a ceramic sample [15]. If the appearance of the intermediate phase is caused by some impurities in $PbZrO_3$, it is really very sensitive to the existence of small quantities of impurities, as high purity (99.99 %) starting powder materials of PbO and ZrO_2 were used and any other components that are not included in the resultant compound were not used in the present synthesis. The transition temperature estimated from the larger anomaly is 505 K in both runs, remarkable thermal hysteresis like $PbTiO_3$ was not observed.

3.3. Result and Discussion

Measured molar heat capacity of $BaTiO_3$ (BT), $PbTiO_3$ (PT), and $PbZrO_3$ (PZ) are shown together in Fig.3.5, where the classical value of Dulong-Petit law of perovskites, namely $15R$ is shown as a broken line. In BT, three sharp heat capacity anomalies are observed at 204, 289, and 402 K, which are caused by the rhombohedral-orthorhombic, orthorhombic-tetragonal, and tetragonal-cubic phase transitions, respectively. On the other hand, in PT and PZ, there is no heat capacity anomaly between 2 and 420 K, as expected. Comparing heat capacity of these

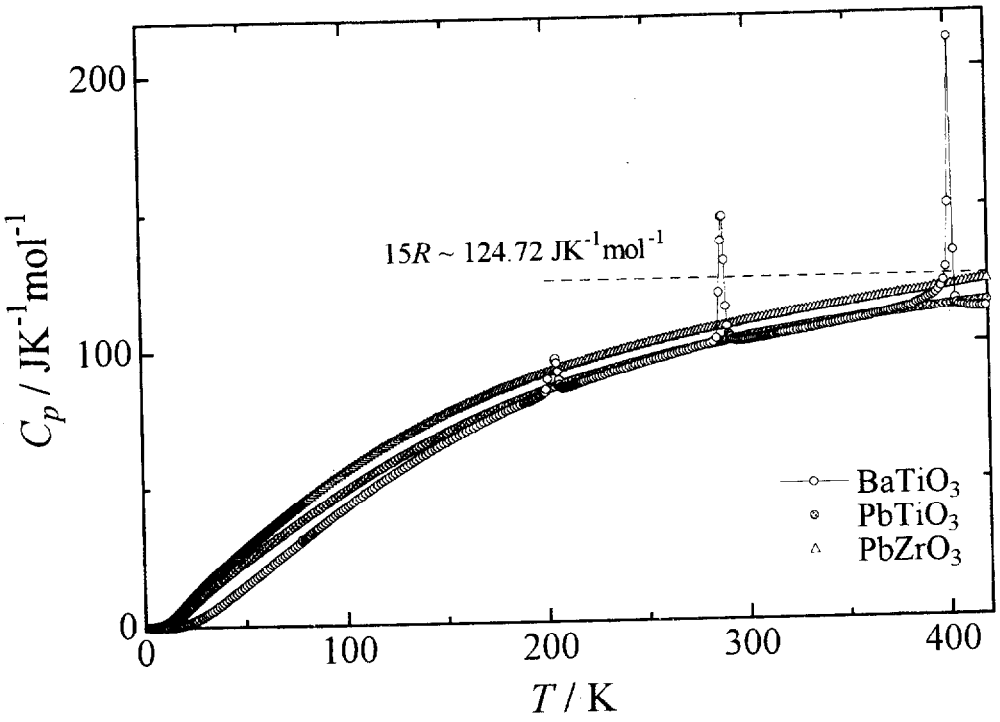

Fig.3.5. Measured molar heat capacity of $BaTiO_3$, $PbTiO_3$, and $PbZrO_3$. A broken line represents the classical value of Dulong-Petit law, $15R$ for the perovskites.

perovskites with each other, some interesting features come to the front. The heat capacity of BT is smaller than that of PT in the whole measurement temperature range except for the phase transition regions. However, both heat capacity curves are approach each other and showing nearly the same value with increasing temperature although their heat capacity values are quite different in the low temperature region below 200 K. Both curves do not yet reach the classical value above 400 K, as generally expected for metal oxides with a high melting point. On the other hand, PZ shows a larger heat capacity value than PT and BT in the whole measurement temperature range. Especially in a high temperature region, PZ shows a much larger value, which is about to exceed the classical value at 420 K, in spite of the approach of PT to BT. The heat capacity of these perovskites is also shown in Fig.3.6 as the C_pT^{-3} *vs.* log$T$ plot in order to see more clearly the difference in a low temperature region, where the previous data of BT [7] are plotted below 13 K. All of them show a peak in the C_pT^{-3} curve, and the peak temperature shifts to lower temperatures and the peak value increases with increasing formula weight, namely BT = 233.1922, PT = 303.0652, and PZ = 346.4222. In addition, below the peak temperature, each value of C_pT^{-3} seems to approach a constant with decreasing temperature. Before discussing such differences among these perovskites, general aspects of the heat capacity should be mentioned.

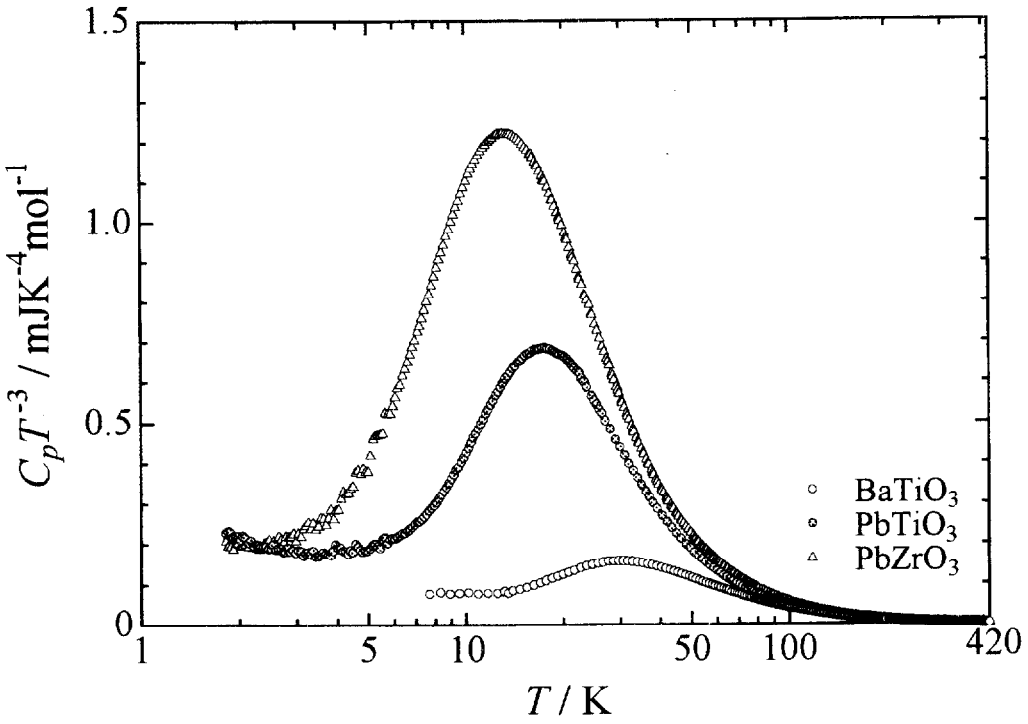

Fig.3.6. C_pT^{-3} *vs.* log$T$ plot for $BaTiO_3$, $PbTiO_3$, and $PbZrO_3$.

As mentioned in *Chapter 1*, since the heat capacity has no selection rule, every energetic contribution is involved in the heat capacity. For example, the excitation of each atomic oscillation in a substance contributes to the heat capacity. Especially in solids, such atomic oscillations form coupled oscillations as the lattice vibration, and the lattice contribution is common to the heat capacity of every solid. At high enough temperatures, the lattice contribution reaches the classical value of Dulong-Petit law according to the equipartition law of energy. In the case that it is sufficient to consider only the translational atomic motion, e.g., metals, ionic crystals, and covalent crystals, the classical value is $3nR$, where n is the number of atoms in formula unit, R (= Nk) is the gas constant, N is Avogadro number, and k is Boltzmann constant, respectively. However, in more complicated cases such as molecular crystals, it is necessary to consider the contributions of molecular rotation, intramolecular vibration and rotation, besides translational molecular motion, and the classical value is determined as a sum of these contributions. In addition to the lattice contribution, in metallic materials, the excitation of free electronic motions contributes to the heat capacity, and in magnetic materials, where the lattice and spin systems behave independently, the magnetic contribution takes part. In general, at very low temperatures, contributions other than the lattice contribution is much larger, while at higher temperatures, it can be said that most part of the heat capacity consists of the lattice contribution. Unlike metallic and magnetic materials with additional contributions, in ideal dielectric materials, their heat capacity should consist of only the lattice contribution. Thus, when the heat capacity of dielectric materials is investigated, it is usually sufficient to consider only the lattice contribution.

In order to describe the temperature dependence of the heat capacity of solids, A. Einstein assumed that each atom in solids was doing harmonic oscillation independently with the same frequency, and derived the following formula:

$$C_v = 3nR\left(\frac{\Theta_E}{T}\right)^2 \frac{e^{\Theta_E/T}}{\left(e^{\Theta_E/T}-1\right)^2}, \tag{3.1}$$

where Θ_E (= $h\nu_E/k$) is Einstein characteristic temperature, ν_E is Einstein characteristic frequency, and h is Planck constant. Einstein could demonstrate skillfully with this formula that the heat capacity of solids decreases with decreasing temperature due to the quantum effect and becomes zero at 0 K. In the lowest temperature region, however, the heat capacity calculated from this formula was not in qualitative agreement with many experimental results concerning the heat capacity of solids, which suggested that his model was too much simplified to describe the real temperature-dependence of the heat capacity. Thus, P. Debye described the lattice vibration as elastic waves propagating through a crystal as an elastic continuum, and found a good agreement with experimental results. Debye formula is represented as

$$C_v = 3nR\left(\frac{T}{\Theta_D}\right)^3 \int_0^{\Theta_D/T} \frac{x^4 e^x}{(e^x-1)^2} dx \quad , \tag{3.2}$$

where Θ_D ($=h\nu_D/k$) is Debye characteristic temperature, and ν_D is Debye characteristic frequency (or cut-off frequency). In this model, at $T \le \Theta_D/10$, the heat capacity is proportional to T^3 as $C_v = 233.8nR(T/\Theta_D)^3$, while at $T \ge \Theta_D$, it becomes $3nR$, which is the classical value of Dulong-Petit law. The heat capacity calculated from Einstein and Debye models and the phonon density of states are shown in Fig.3.7. In Fig.3.7(a), it seems that both heat capacity show similar temperature-dependence and approach asymptotically the classical value above characteristic temperature, where the heat capacity and the temperature are normalized by the classical value and the characteristic temperature, respectively. However, the most striking difference is seen in the lowest temperature region shown in Fig.3.7(b) as the C_vT^{-3} vs. log$T$ plot. In this plot, C_vT^{-3} of Debye model becomes constant at $T \le \Theta_D/10$, as $C_v = 233.8nR(T/\Theta_D)^3$, while C_vT^{-3} of Einstein model shows a broad maximum at $T = \Theta_E/5$ and approaches zero with decreasing temperature. This approach to zero of C_vT^{-3} is the worst failure of Einstein model. Nevertheless, the contribution of vibrations

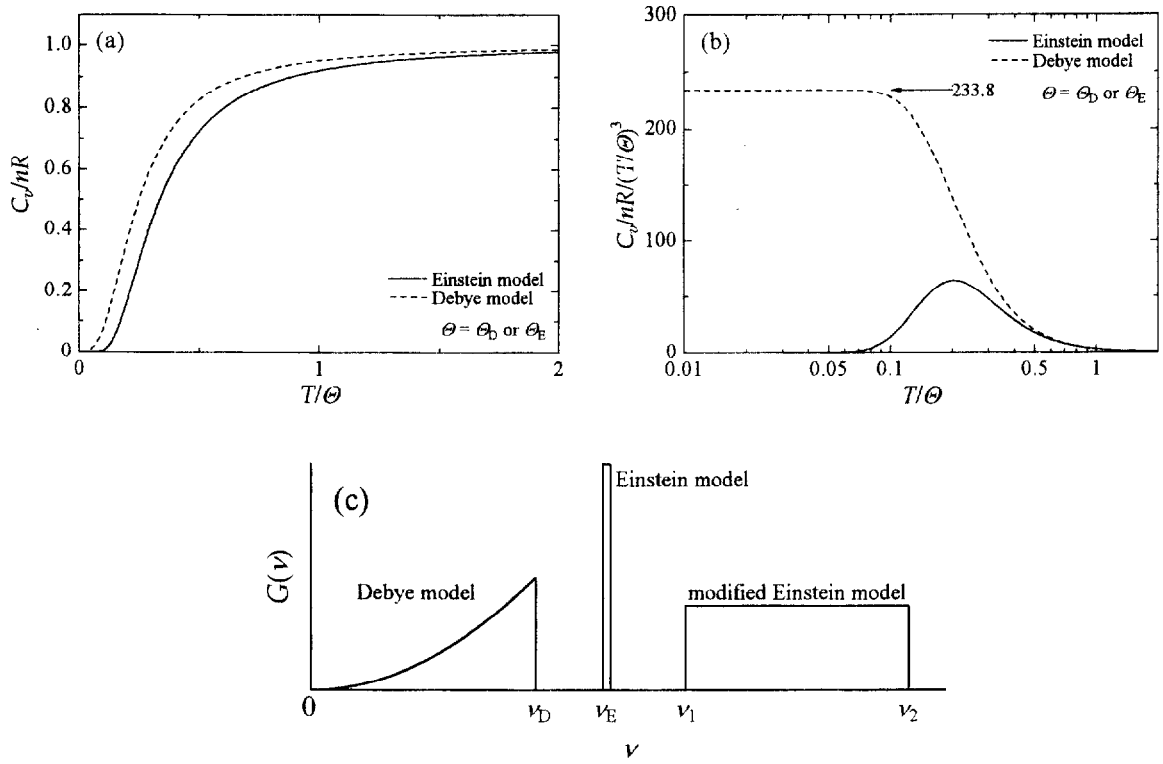

Fig.3.7. (a) Heat capacity calculated from Einstein and Debye formulae, (b) C_pT^{-3} *vs.* log$T$ plot, and (c) phonon density of states of each model.

characterized by a single frequency such as intramolecular vibrations and weak dispersive optical phonons can be well described by Einstein model, where the distribution of phonon density of state is described as δ-function, as it is characterized by a single characteristic frequency ν_E (Fig.3.7(c)). For describing strong dispersive optical phonons, a modified Einstein model can be employed. This model can be considered as Einstein model with strong dispersion, and the δ-function-like distribution of the phonon density of states is dispersed over the frequency range from ν_1 to ν_2 while the phonon density of states at every frequency is kept to be the same, as shown in Fig.3.7(c). The modified Einstein formula is represented as

$$C_v = 3nR\frac{T}{\Theta_2 - \Theta_1}\int_{\Theta_1/T}^{\Theta_2/T}\frac{x^2 e^x}{(e^x - 1)^2}dx, \tag{3.3}$$

where Θ_1 and Θ_2 are the characteristic temperatures representing the lower and upper limit of the phonon density of states, and $\Theta_i = h\nu_i/k$ (i = 1 or 2). The heat capacity calculated from this formula shows a similar temperature-dependence to that of Einstein model. On the other hand, Debye model is essentially for the acoustic phonons, which are elastic waves by nature. In general, since only the acoustic phonons with a long wavelength can be excited at very low temperatures, the real temperature-dependence of the heat capacity in the lowest temperature region can be well described by Debye model. In Debye model, the phonon density of states is proportional to ν^2 and cut off at ν_D, and the gradient near $\nu = 0$ is of importance for describing the temperature-dependence of the heat capacity in the lowest temperature region. As expected from the fact that in Debye model a crystal is considered as an elastic continuum, Debye characteristic temperature Θ_D can be estimated from the propagating velocity of elastic waves, i.e., the sound velocity. Θ_D in general anisotropic crystals is represented as

$$\Theta_D^{el} = \frac{h\nu_m}{k}\left(\frac{3nN}{4\pi V}\right)^{1/3}, \tag{3.4}$$

where V is molar volume and ν_m is the space average of three sound velocities ν_1, ν_2, and ν_3. The averaging process is defined by the equation

$$\nu_m = \left(\frac{1}{3}\sum_{i=1}^{3}\int_0^{4\pi}\frac{1}{\nu_i^3}\frac{d\omega}{4\pi}\right)^{-1/3}. \tag{3.5}$$

In anisotropic crystals, the estimation is a little complicated due to this averaging procedure of sound velocities, while in the case of isotropic crystals, simpler equation is obtained as

$$\nu_m = \left(\frac{1}{3\nu_l^3} + \frac{2}{3\nu_t^3}\right)^{-1/3}, \tag{3.6}$$

where ν_l and ν_t are the longitudinal and transverse sound velocities, respectively. These sound

velocities are connected with Young's modulus E_{el} and rigidity modulus G_{el} as the following relation:

$$v_l = \left(\frac{G_{el}}{\rho} \cdot \frac{4G_{el} - E_{el}}{3G_{el} - E_{el}} \right)^{1/2} \quad \text{and} \quad v_t = \left(\frac{G_{el}}{\rho} \right)^{1/2}, \tag{3.7}$$

where ρ is the density of a crystal.

In the system with a finite number of discrete energy levels, the heat capacity anomaly called "Schottky anomaly" appears in the temperature region where the population probability at each level is changed by thermal excitation. This anomaly is generally observed in the substances with paramagnetic ions, and in the case of a nondegenerate two-level system with interval E, it is represented as

$$C_{Sch} = N\left(\frac{E}{kT}\right)^2 \frac{e^{E/kT}}{\left(e^{E/kT}+1\right)^2}. \tag{3.8}$$

Although every particle is populating the ground level at 0 K, particles are gradually excited to higher energy levels with increasing temperature, and the heat capacity becomes larger by the energy required for the excitation. With further increasing temperature, however, the number of particle at the ground level decreases, and the heat capacity becomes smaller. Thus, Schottky anomaly describes a curve with a broad maximum as shown in Fig.3.8(a). It is known that in a two-level system, this maximum appears around $kT / E = 0.42$. Here, compared Schottky formula (3.8) with Einstein formula (3.1), it can be seen that Schottky formula is equivalent to the difference between the two Einstein formulae with different characteristic frequencies of ν_E and $2\nu_E$, i.e., $C_{Sch} = C_v(\Theta_E/T) - C_v(2\Theta_E/T)$. This means

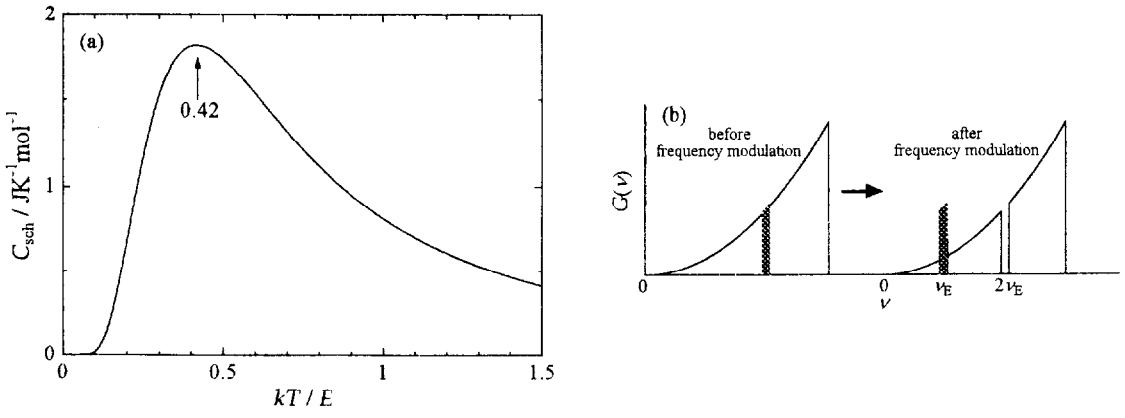

Fig.3.8. (a) Schottky heat capacity anomaly, and (b) the example of change in the phonon density of states providing a Schottky anomaly-like excess heat capacity.

that for a specific lattice vibrational mode in a substance, when the frequency is modulated to be a half without changing the degrees of freedom, the heat capacity difference between before and after the frequency modulation shows Schottky anomaly-like temperature-dependence. For example, assuming the Debye-type phonon density of states as the original, the phonons at the frequency of $2\nu_E$ is shifted down to ν_E as shown in Fig.3.8(b), and the difference between the heat capacity calculated from the phonon density of states before and after the frequency modulation describes the same curve as shown in Fig.3.8(a). Thus, when the difference or change in the phonon density of states between two similar compounds is investigated, it is often effective to consider the heat capacity difference between those compounds.

These models for describing the temperature-dependence of the heat capacity seem to be a little outdated in these days when the developments of computational technologies are so amazing: in computer simulations using lattice dynamics or molecular dynamics, it is possible to some extent to estimate the phonon density of states and the heat capacity on the basis of specific models for individual substances in line with other experimental results, especially structural studies. On the other hand, these models are general ones for the heat capacity and do not presume any specific models for individual substances. Thus, it is impossible to obtain the information about the origin of a heat capacity difference between different substances directly from these models. Nevertheless, these models have been employed quite frequently in the forefront of heat capacity investigations even at the present, because these models are very simple and might be easier to treat as not requiring complicated calculations. In addition, so long as only a low frequency region is considered, these models are sufficient to estimate the approximate distribution of the phonon density of states from measured heat capacity. Finally, it should be noted that in general, measured heat capacity of solids is usually the heat capacity at constant pressure C_p, while calculate heat capacity is the heat capacity at constant volume C_v. Thus, the correction between C_p and C_v is necessary for comparing the results of experiment and calculation, but in the case of solids, a difference between C_p and C_v is not so large, and especially at low temperatures, it can be considered that $C_p \cong C_v$. Therefore, in this study, the correction between C_p and C_v is not made for every data analysis.

Here, returning to the subject, the heat capacity difference, ΔC_p, of PT and PZ from BT is considered, as BT shows the lowest heat capacity among these perovskites. Fig.3.9 shows ΔC_p of PT and PZ from BT, except for the phase transition regions. It is clearly seen that PT shows a Schottky anomaly-like heat capacity difference with a broad maximum at 43 K, which suggests that for a specific lattice vibrational mode common to perovskites, the frequency shifts down by substitution of Ba by Pb: in simple consideration on dynamics, the frequency of oscillation decreases with increasing the mass of oscillator. On the other hand, PZ also shows a Schottky anomaly-like heat capacity difference with a broad maximum at 71 K, but an

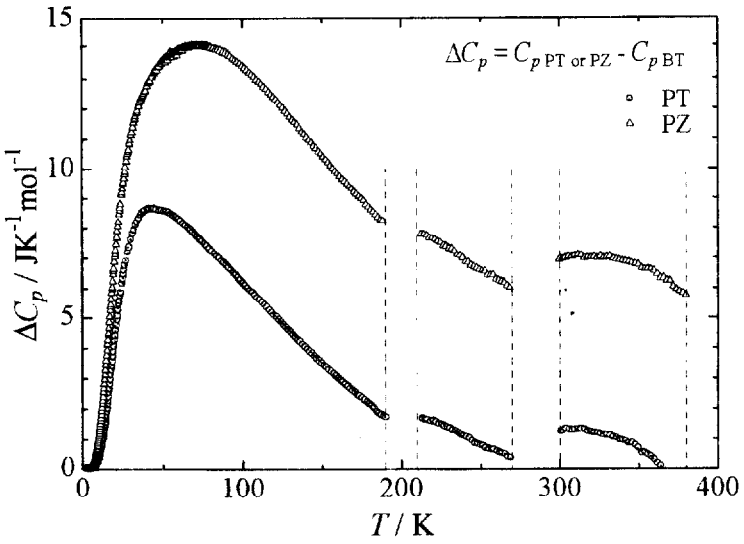

Fig.3.9. Heat capacity difference of $PbTiO_3$ and $PbZrO_3$ from $BaTiO_3$.

additional contribution clearly exists in PZ. In BT and PZ, their crystal structures are the same but ionic kinds are quite different, and it is difficult to compare directly. Thus, the heat capacity difference of PZ from PT is considered and shown in Fig.3.10. In this figure, PZ also shows a Schottky anomaly-like maximum at 112 K, which suggests the atomic mass effect between Zr and Ti, similar to that between Pb and Ba, but additional contributions clearly exist around 20 K (the arrowed point) and above 300 K, which demonstrate singularity of PZ.

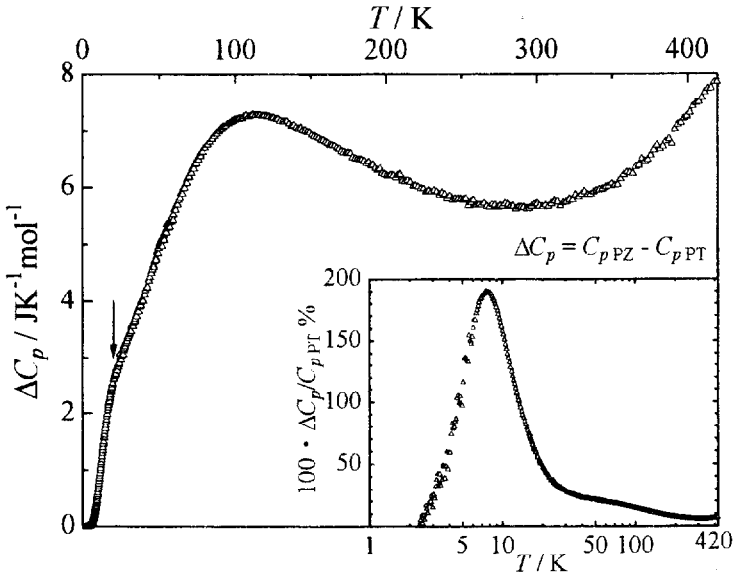

Fig.3.10. Heat capacity difference of $PbZrO_3$ from $PbTiO_3$. The inset shows the percentage of the heat capacity difference.

Compared Fig.3.6 and Fig.3.7(b), it can be seen that the heat capacity of these perovskites in a low temperature region can be described by a combination of Debye and Einstein terms. Thus, the distribution of the phonon density of states was estimated for each perovskite by nonlinear least square fitting to the measured heat capacity using Debye, Einstein and modified Einstein formulae. The contribution of the acoustic phonons with $3N$ degrees of freedom* is described by Debye formula. Since perovskites have 5 atoms in the formula unit, the total degrees of freedom become $15N$. Thus the residual $12N$ degrees of freedom are for the optical phonons. For the contribution of low frequency optical phonons with weak dispersion, Einstein formula is employed, while the contribution of optical phonons in a high frequency region is represented by modified Einstein formula. Nonlinear least square fitting to the measured heat capacity was performed with the characteristic temperatures and the degrees of freedom of each formula as independent fitting parameters, except for the degrees of freedom in Debye formula, which was fixed to be $3N$. The results of the fittings are shown in Fig.3.11. Low temperature heat capacity below 50 K of many dielectric materials has been already

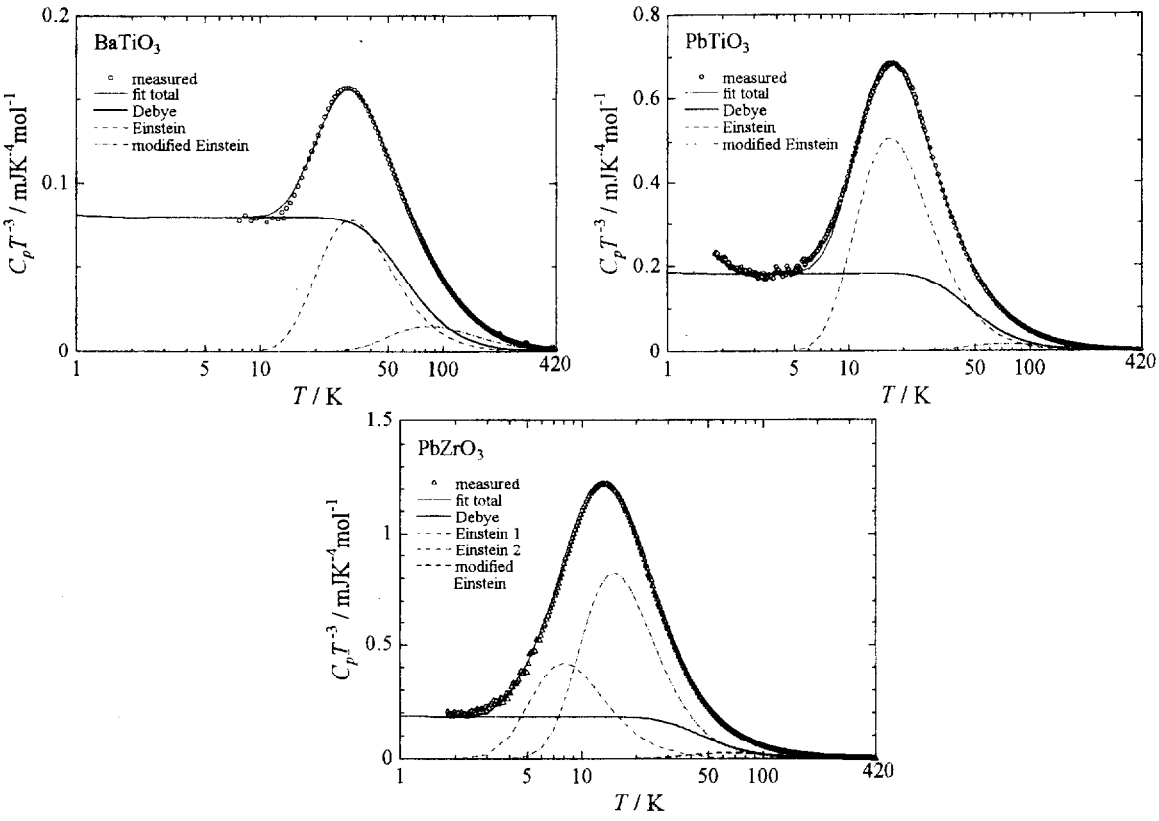

Fig.3.11. Results of the fittings to the measured heat capacity using Debye, Einstein, and modified Einstein formulae as the C_pT^{-3} vs. log$T$ plots.

* It can be called "the number of states". In the case of Einstein model, some call it "oscillator strength", but this is not so good expression.

measured by Lawless [1], and he has suggested that in many cases a maximum in the C_pT^{-3} *vs.* log$T$ plot is well described by a single Einstein formula. In BT and PT, the maximum is well described by a single Einstein formula as reported by Lawless [1]. On the other hand, in PZ, the maximum can not be described by a single Einstein formula, and PZ requires at least two Einstein formulae, which suggested additional lattice vibrational mode or some other contributions in a very low frequency region. The estimated distribution of the phonon density of states in a low frequency region is shown in Fig.3.12. It can be clearly seen in this figure that in common to these perovskites, there is a lattice vibrational mode with nearly the same degrees of freedom (1.6 ~ 1.9), and the frequency shifted from 3.2 THz in BT down to 1.7 and 1.5 THz in PT and PZ, respectively: the frequency is modulated to be a half by substitution of Ba by Pb, and this frequency modulation of the specific lattice vibrational mode can be considered as the origin of Schottky anomaly-like excess heat capacity of PT and PZ for BT. This frequency modulation is mainly caused by the mass effect between Pb (207) and Ba (137) although it can be also considered the difference in the force constant between each ion due to the difference in the covalency between Pb-O and Ba-O [19-21]. On the other hand, in PZ, there are additional phonon states at 0.8 THz, which are indispensable for describing the heat capacity in a low temperature region: this corresponds to the additional contribution seen in the heat capacity difference of PZ from PT around 20 K (Fig.3.10). However, the physical origin of this additional contribution is unclear. If this is attributed to the phonon, it results in low frequency "anomalous" optical phonons. Recently, Ghosez *et al.* [20] has performed first-principle lattice dynamics simulation for cubic BT, PT, and PZ, and reported that the substitution of Ba by Pb strongly strengthens the *A*-O coupling, while the substitution of Ti in PT by Zr strongly modified *B*-O interaction and slightly strengthens Pb-O coupling. Maybe

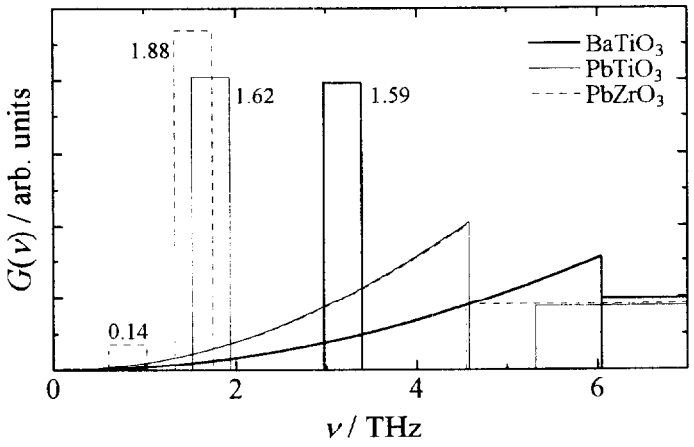

Fig.3.12. Estimated phonon density of states in a low frequency region from the results of the fittings to the measured heat capacity.

either the strong Pb-O coupling or the oscillation of Zr uncoupled with Pb and O results in the anomalous low frequency optical phonons in PZ. However, such a low frequency optical phonon is quite unusual and another possibility can be also considered. In the orthorhombic antiferroelectric phase of PZ, Pb ions form double rows with alternate displacements along $[1\,\bar{1}\,0]_{cub}$ and $[\bar{1}\,10]_{cub}$ directions (the subscript 'cub' denotes indices referred to the pseudo-cubic lattice) **[15]**, and there might be some low energy excitation related to singular Pb ion displacements or antiferroelectric dipolar interactions. In comparison of PT and PZ, it is interesting that PZ shows larger heat capacity values than PT over almost the whole measurement temperature range, especially around 10 K (the inset of Fig.3.10), but in T^3-region, both are described by Debye formula with the same Debye temperature of 220 K. And for these perovskites, Debye temperature is estimated from elastic coefficient data reported previously. In the case of perovskites, Debye temperature is generally estimated for $15N$ degrees of freedom, as perovskites include 5 atoms in the formula unit. However, now considering the acoustic phonons with $3N$ degrees of freedom, an estimated value of Θ_D^{el} for $15N$ should be scaled for $3N$, as ${}^{3N}\Theta_D^{el} = 5^{-1/3} \cdot {}^{15N}\Theta_D^{el}$ *. There have been some reports on elastic stiffness moduli in the tetragonal phase of BT and PT, but no reports on that in the rhombohedral phase of BT to the best of my knowledge. Since there is anisotoropy in the tetragonal phase, it is necessary to average the sound velocities over the whole space using Eq.(3.5). However, it is impossible to estimate Θ_D^{el} only with the reported elastic stiffness moduli, and it requires a great deal of labor even if possible. Thus, the harmonic series expansion method for the tetragonal symmetry **[22]** is employed, which can provide a good result comparable to a numerical integration method **[22]**. The results of the estimation are tabulated in Table.3.1. For PT, the elastic Debye temperature is in good agreement with the calorimetric one obtained in this study, while for BT, a large discrepancy is seen between both, which might be due to the difference in the phase where the measurements were carried out: the elastic measurements were made on the tetragonal phase at room temperature, while in the heat capacity measurements, the low temperature region for determining Debye temperature is in the rhombohedral phase. On the other hand, for PZ, there has been a report on an elastic measurement for a ceramic sample **[29]**, where the anisotropy should not be observed due to random orientations of grains, and Eq.(3.6) can be used by accumulating a large number of sound velocity data along arbitrary different directions **[30]**, but a result may depend on the density of a sintered sample. An estimated elastic Debye temperature has been already provided in that report, and it is also shown in Table 3.1, which is also in good agreement in the

* The phonon density of state in Debye model is proportional to ν^2 and its integral from 0 to ν_D, i.e., $\nu_D^3/3$ is the total degrees of freedom. Thus, $3N : 15N = {}^{3N}\nu_D^3/3 : {}^{15N}\nu_D^3/3$. This is a valid scaling method, because in Debye model, only the gradient of the density of states near $\nu = 0$ is of importance for describing the low temperature heat capacity below $\Theta_D/10$.

calorimetric one. Thus, it can be confirmed from both elastic and calorimetric investigations that PT and PZ have nearly the same Debye temperature about 220 K.

	$BaTiO_3$				$PbTiO_3$				$PbZrO_3$	
	[23]	[24]	[25]	C_p	[26]	[27]	[28]	C_p	[29]	C_p
${}^{15N}\Theta_D$ / K	426	422	409	496	358	367	372	380	396	370
${}^{3N}\Theta_D$ / K	249	245	239	290	209	214	218	222	232	216

Table.3.1. Estimated elastic and calorimetric Debye characteristic temperature for $BaTiO_3$, $PbTiO_3$, and $PbZrO_3$. The number in the brackets refers to the reference number.

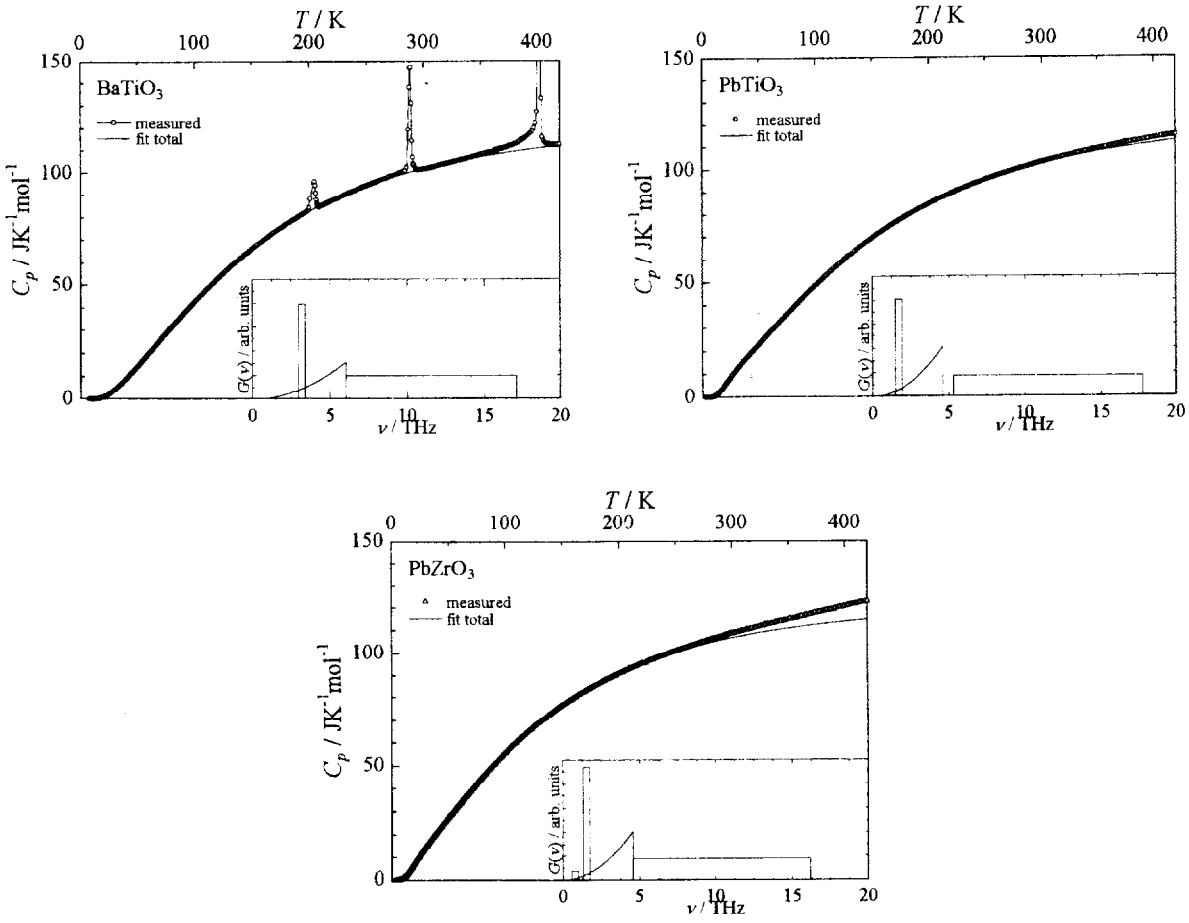

Fig.3.13. Full-scale results of the fittings to the measured heat capacity. The inset shows the estimated distribution of phonon density of states.

The full-scale results of the fittings are shown in Fig.3.13, where the estimated distribution of the phonon density of states is also shown in the insets, and the converged values of the fitting parameters are tabulated in Table 3.2. Employing a single modified Einstein formula for high frequency phonons, the heat capacity of these perovskites can be described except for a high temperature region. In BT, there are three phase transitions and there is a small jump between the lattice contributions of each phase at the phase transitions, which is observed as a jump of the heat capacity difference shown in Fig.3.9. Nevertheless, the heat capacity of BT can be well described by such simple models. For PT, the heat capacity can be also well described although a small discrepancy is seen above 300 K, which is usually caused by the anharmonicity in the lattice vibrations: the calculated heat capacity is C_v, where the anharmonic effect should not be observed by nature. On the whole, the heat capacity of PT and BT shows typical temperature-dependence of the heat capacity of metal oxides, and it can be said that both perovskites are "normal" ferroelectrics. On the other hand, for PZ, the heat capacity below 200 K can be also well described by simple models, and the mass effect between Zr and Ti expected from ΔC_p of PZ from PT (Fig.3.10) can be observed as shift-down of the characteristic frequency in a modified Einstein formula from 5.3 ~ 17.8 THz in PT to 4.5 ~ 16.2 THz in PZ: as the mass of the *B*-site cations, Ti (48) and Zr (91), are smaller than that of the *A*-site cations, Ba (137) and Pb (207), the mass effect of *B*-site cations should be observed in a higher frequency region. However, above 200 K, a large discrepancy is observed between the measured and calculated heat capacity. Moreover, the heat capacity shows rather divergent than convergent tendency, and this tendency is also seen in Fig.3.10. Since the antiferroelectric transition point of PZ is about 500 K, the precursor of the phase transition might already occur around room temperature. However, BT does not show such a large discrepancy even around the phase transition regions, but the tendency only below the ferroelectric phase transition, i.e., the tetragonal-cubic one, is similar to that of PZ: the heat capacity anomaly has long tail below the transition point. In fact, the other two phase transitions in BT are clear first-order transitions with the displacive type of mechanism, while the ferroelectric phase transition is a first-order transition quite close to second-order with both displacive and order-disorder types of mechanism **[31-34]**, and the detailed mechanism of the ferroelectric phase transition in BT is still in controversy. In addition, it has been reported that the structure of the cubic phase of BT is not ideal cubic but pseudo-cubic with random ionic shifts from the ideal crystallographic sites, and this random ionic shifts closely related to the order-disorder type of mechanism in BT **[35]**. Recently, similar random ionic shifts in the cubic paraelectric phase and the related order-disorder type of phase transition mechanism has been also reported for PZ **[36]**, while no evidence of such ionic shifts has been observed in PT **[36]**. Thus, such random ionic shifts might be related to the long tail of heat capacity anomaly below the transition point.

compound	model	characteristic frequency ν / THz (characteristic temperature Θ / K)	degrees of freedom / N
$BaTiO_3$	Debye	6.04 (290)	3.00 (fixed)
	Einstein	3.20 (153)	1.59
	Modified Einstein	6.04 – 17.13 (290 – 822)	10.41
$PbTiO_3$	Debye	4.63 (222)	3.00 (fixed)
	Einstein	1.73 (83)	1.62
	Modified Einstein	5.31 – 17.75 (255 – 852)	10.38
$PbZrO_3$	Debye	4.50 (216)	3.00 (fixed)
	Einstein 1	0.81 (39)	0.14
	Einstein 2	1.54 (74)	1.88
	Modified Einstein	4.54 – 16.19 (218 – 777)	9.98

Table.3.2. Converged values of the fitting parameters in nonlinear least square fitting to the measured heat capacity using Debye, Einstein, and modified Einstein formulae.

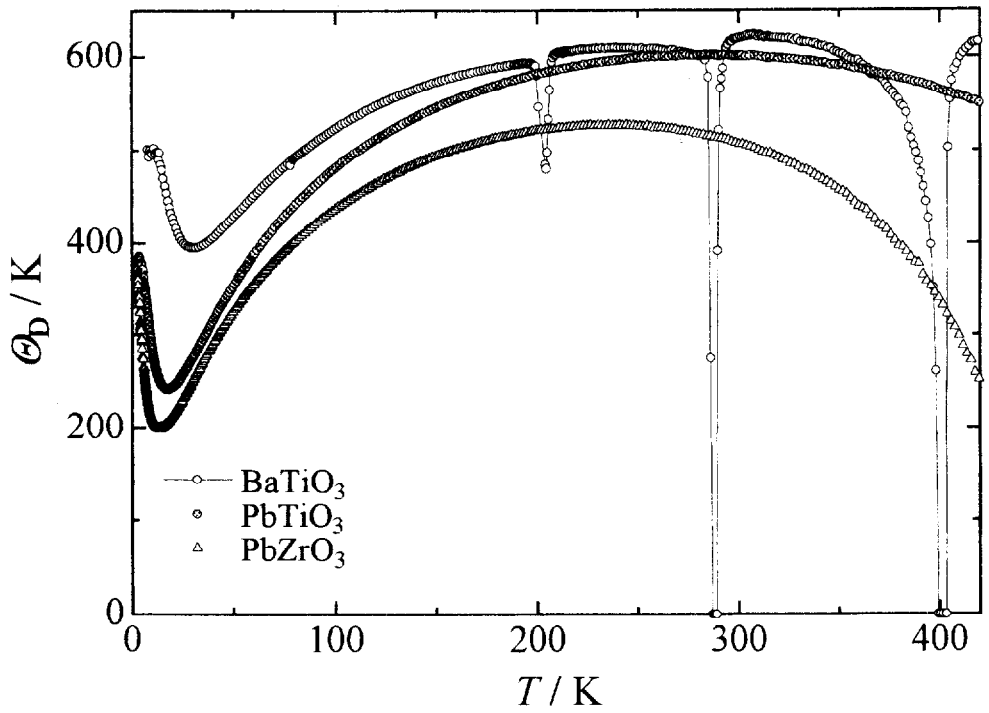

Fig.3.14. Debye characteristic temperature calculated from the measured heat capacity of $BaTiO_3$, $PbTiO_3$, and $PbZrO_3$, assuming $15N$ degrees of freedom.

In Debye and Einstein models, the temperature-dependence of the heat capacity is uniquely determined by a single parameter, i.e., a characteristic temperature. Contrary, if the values of temperature and heat capacity are given to the formula, the value of a characteristic temperature that gives that heat capacity value at that temperature can be obtained. In heat capacity investigation, measured heat capacity values are often converted to Debye characteristic temperature* according to this procedure. Fig.3.14 shows the Debye temperature of BT, PT, and PZ calculated from the measured heat capacity assuming $15N$ degrees of freedom**. If the heat capacity calculated from Debye formula is converted to Debye temperature, of course the Debye temperature does not show temperature-dependence, namely it is constant. However, there is no real substance completely obeying Debye model, and the Debye temperature calculated from measured heat capacity shows characteristic temperature-dependence of individual substances as shown in Fig.3.14. Therefore, Debye temperature curve indicates a relative difference from Debye model. In the lowest temperature region, i.e., T^3-region, Debye temperature is constant, but with decreasing temperature, it falls down and shows a deep minimum (around 20 ~ 30 K in Fig.3.14). This minimum is caused by various contributions that are not assumed in Debye model such as low frequency optical phonons, and it corresponds to a maximum in the C_pT^{-3} *vs.* log$T$ plot. With further increasing temperature, Debye temperature increases gradually and approaches a constant value, as the heat capacity approaches a classical value. However, if anharmonic effect in the lattice vibrations becomes stronger with increasing temperature, Debye temperature decreases again as seen above 300 K in PT, and in this case, it never increases again. On the other hand, in PZ, the Debye temperature decreases drastically above 200 K, and if it continues to decrease at the same rate, it reaches zero around 450 K, which means the excess of the heat capacity over the classical value. Thus, it can be considered that in PZ the precursor of the phase transition greatly contributes to the heat capacity. In the case that there are heat capacity anomalies, Debye temperature curve shows downward spike-like features as illustrated by the phase transitions in BT, and in the temperature region where heat capacity is exceeding the classical value, Debye temperature can not be defined. In a substance with larger heat capacity values, corresponding Debye temperatures become smaller, namely $C_{p\mathrm{BT}} < C_{p\mathrm{PT}} < C_{p\mathrm{PZ}}$ but $\Theta_{\mathrm{DBT}} > \Theta_{\mathrm{DPT}} > \Theta_{\mathrm{DPZ}}$. In addition, a small heat capacity difference between BT and PT above 200 K is not clearly seen in the plot of raw data (Fig.3.5), while it can be clearly seen in the plot of Debye temperature. Thus, in some cases, Debye temperature is more sensitive to a small heat capacity difference

* Debye temperature converted from measured heat capacity is often called "effective Debye temperature" and distinguished from that estimated from heat capacity in T^3-region, elastic coefficient data, and other experiments.

** Since the degrees of freedom is different from each substance, it must be determined in advance, but the way to determine is arbitrary. For example, assuming that at very low temperatures, only the acoustic phonons with $3N$ degrees of freedom can be excited, it is possible to provide $3N$ degrees of freedom for the formula. The calorimetric Debye temperatures in Table.3.1 can be obtained in this manner. In this case, however, above the temperature where heat capacity value exceeds $3R$, Debye temperature can not be defined.

and anomalies than raw data of heat capacity, as also illustrated by the phase transitions in BT, where the corresponding anomalies become sharper. Debye temperature is nothing but a converted parameter of measured heat capacity, and it has no physical significance. However, it gives us the information difficult to catch in raw data of heat capacity, and it is often used for heat capacity investigations.

3.4. Conclusion

In this chapter, the features seen in the heat capacity are specified for the typical perovskite (anti)ferroelectrics, $BaTiO_3$ (BT), $PbTiO_3$ (PT), and $PbZrO_3$ (PZ). For specific lattice vibrational states common to the perovskites, the frequencies are modulated by the atomic mass effect due to the atomic substitution, e.g., from Ba to Pb: the frequency decreases with increasing the atomic mass. For BT and PT, the heat capacity below 50 K can be well described by the combination of a single Debye and single Einstein formula, while for PZ, at least two Einstein formulae are required for describing the heat capacity below 50 K. This suggests the existence of additional low energy excitation in PZ, which might be related to its antiferroelectricity. The heat capacity of BT and PT can be well described by the combination of simple models over the whole measurement temperature range, and both perovskites can be considered as "normal" ferroelectrics from a point of view of the heat capacity. On the other hand, in PZ, a large discrepancy is seen between the measured and calculated heat capacity above 200 K, which suggests the precursor toward the antiferroelectric phase transition about 500 K. Not considered in detail since it is not the main subject of this study, it is very interesting that in PT and PZ with the same crystal structure and the same ionic kinds, such large heat capacity difference is observed between both as shown in Fig.3.15. Moreover, both also have the interest as the end members of $PbZr_xTi_{1-x}O_3$ solid solution system. However, there has been no report on the systematic and detailed heat capacity investigations over a wide temperature range in this system so far. It is also very interesting to investigate systematically the heat capacity variation with respect to the Zr fraction x, and it can be sufficiently a significant subject of investigation.

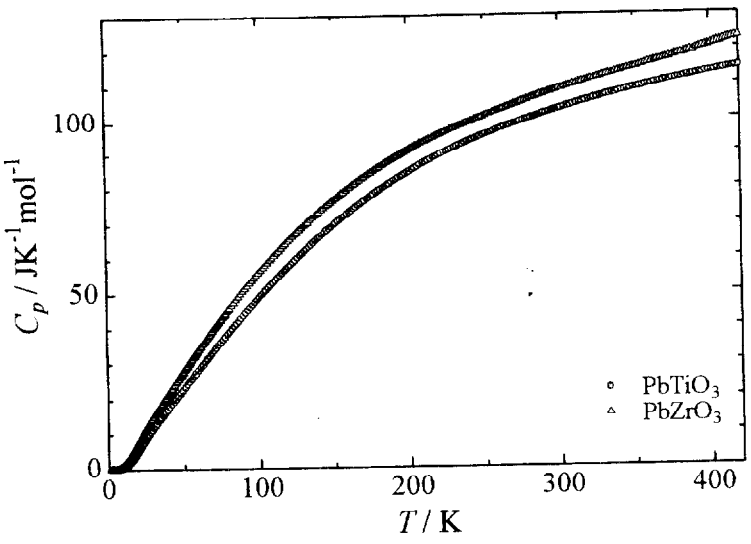

Fig.3.15. Heat capacity of $PbTiO_3$ and $PbZrO_3$ in enlarged scale of Fig.3.5.

References

[1] W. N. Lawless, *Phys. Rev.* **B14**, 134 (1976); *Ferroelectrics*, **17**, 341 (1977).

[2] W. N. Lawless, T. Nakamura, M. Takashige, and S. L. Swartz, *J. Phys. Soc. Jpn.* **52**, 207 (1983).

[3] M. Hortal, S. Vieira, and R. Villar, *Ferroelectrics* **54**, 313 (1984).

[4] M. C. Hoote and A. C. Anderson, *Ferroelectrics* **62**, 11 (1985).

[5] I. Hatta and A. Ikushima, *J. Phys. Soc. Jpn.* **41**, 558 (1976).

[6] M. H. Frey and D. A. Payne, *Phys. Rev.* **B54**, 3158 (1996)

[7] A. Hamano, Ph.D. thesis (Tokyo Institute of Technology, 1988)

[8] S. S. Todd and R. E. Lorenson, *J. Am. Chem. Soc.* **74**, 1952 (1952).

[9] J. P. Remeika and A. M. Glass, *Mat. Res. Bull.* **5**, 37 (1970).

[10] R. Clarke and R. W. Whatmore, *J. Cryst. Growth* **33**, 29 (1976).

[11] R. W. Whatmore and A. M. Glazer, *J. Phys. C: Solid State Phys.* **12**, 1505 (1979).

[12] B. Jaffe, W. R. Cook, Jr. and H. Jaffe, *Piezoelectric Ceramics* (Academic Press, London, 1971).

[13] S. Fushimi,and T. Ikeda, *J. Am. Ceram. Soc.* **50**, 129 (1967).

[14] G. Shirane and S. Hoshino, *J. Phys. Soc. Jpn.* **6**, 265 (1951).

[15] E. Sawaguchi, H. Maniwa, and S. Hoshino, *Phys. Rev.* **83**, 1078 (1951);E. Sawaguchi, G. Shirane, and Y. Takagi, *J. Phys. Soc. Jpn.* **6**, 333 (1951).

[16] V. J. Tennery, *J. Electrochem. Soc.* **112**, 1117 (1965).

[17] V. J. Tennery, *J. Am. Ceram. Soc.* **49**, 483 (1966).

[18] L. Goulpeau, *Sov. Phys.-Solid State* **8**, 1970 (1967).

[19] R. Cohen, *Nature* **358**, 136 (1992); *Ferroelectrics* **136**, 65 (1992).

[20] Ph. Ghosez, E. Cockayne, U. V. Waghmare, and K. M. Rabe, *Phys. Rev.* **B60**, 836 (1999).

[21] Y. Kuroiwa, S. Aoyagi, A. Sawada, J. Harada, E. Nishibori, M. Takata, and M. Sakata, *Phys. Rev. Lett.* **87**, 217601 (2001).

[22] G. A. Alers, in *Physical Acoustics*, edited by W. P. Mason (Academic, New York, 1965), Vol. IIIB, p.1.

[23] Z. Li, S.-K. Chan, M. H. Grimsditch, and E. S. Zouboulis, *J. Appl. Phys.* **70**, 7327 (1991).

[24] A. Schaefer, H. Schimitt, and A. Dorr, *Ferroelectrics* **69**, 253 (1986).

[25] D. Berlincourt and H. Jaffe, *Phys. Rev.* **111**, 143 (1958).

[26] A. G Kalinichev, J. D. Bass, B. N. Sun, and D. A. Payne, *J. Mat. Res.* **12**, 2623 (1997).

[27] Z. Li, M. Grimsditch, X. Xu, and S.-K. Chan, *Ferroelectrics* **141**, 313 (1993).

[28] S. Ikegami, I. Ueda, and T. Nagata, *J. Acoust. Soc. Am.* **50**, 1060 (1971).

[29] A. Y. Wu and R. J. Sladek, *Phys. Rev.* **B27**, 2089 (1983).

[30]O. L. Anderson, in *Physical Acoustics*, edited by W. P. Mason (Academic, New York, 1965), Vol. IIIB, p.43.

[31]H. Takahashi, *J. Phys. Soc. Jpn.* **16**, 1685 (1961).

[32]R. Comes, M. Lambert, and A. Guiner, *Solid State Commun.* **6**, 715 (1968).

[33]Y. Yamada, G. Shirane, and A. Linz, *Phys. Rev.* **177**, 848 (1969); G. Shirane, J. D. Axe, and J. Harada, *Phys. Rev.* **B2**, 3651 (1970); J. Harada, J. D. Axe, and G. Shirane, *Phys. Rev.* **B4**, 155 (1971)

[34]H. Vogt, J. A. Sanjurjo, and G. Rossbroich, *Phys. Rev.* **B26**, (1982); K. Iniue and S. Akimoto, *Solid State Commun.* **46**, 441 (1983).

[35]K. Itoh, L. Z. Zeng, E. Nakamura, and N. Mishima, *Ferroelectrics* **63**, 29 (1985).

[36]S. Aoyagi, Y. Kuroiwa, A. Sawada, H. Tanaka, J. Harada, E. Nishibori, M. Takata, and M. Sakata, *J. Phys. Soc. Jpn.* **71**, 2353 (2002).

Chapter 4

$Pb(Mg_{1/3}Nb_{2/3})O_3$ and $Pb(Mg_{1/3}Ta_{2/3})O_3$

Typical Perovskite Relaxors

—— Singularities in Their Heat Capacity

4.1. Introduction

$Pb(Mg_{1/3}Nb_{2/3})O_3$ (PMN) is a typical relaxor showing a large, broad and frequency-dependent peak in the dielectric constant curve around 300 K. Most of studies on relaxors have been conducted on PMN, since it has been considered as a prototype of relaxors. Therefore, first of all, brief explanations are given for the structural features elucidated experimentally and the physical models proposed for PMN.

Ferroelectric Nanoregions

The earlier question is why PMN shows a broad peak in the dielectric constant unlike a sharp peak at a ferroelectric phase transition in usual (anti)ferroelectrics. When a peak is observed in the dielectric constant, everybody may remind of the occurrence of a phase transition. In fact, many researchers thought so at the beginning, not excepting the discoverer of relaxors, G. A. Smolenskii. On the analogy of $BaTi_{1-x}Sn_xO_3$ solid solution system **[1]**, he tried to explain a broad dielectric peak of relaxors with the compositional fluctuation model **[2,3]**. In lead-based perovskite complex compounds, the *B*-site is occupied by two kinds of cations, and these cations distribute randomly on the *B*-site sublattice. Thus, the compositional fluctuation on the *B*-site sublattice gives rise to the fluctuation of local phase transition points, and the microscopic regions with different phase transition points gradually undergo a phase transition. Consequently, a broad peak is formed in the dielectric constant curve as a function of temperature, and a peak temperature indicates an averaged phase transition point. Therefore, Smolenskii called this phenomenon "diffuse phase transition", and according to this concept, the low temperature phase of PMN should be ferroelectric. However, this model faced a problem soon, i.e., glass-like dielectric dispersion. The peak temperature of the dielectric constant increases with increasing measurement frequency, and the definition of a peak temperature as an averaged phase transition point was not approved any longer. Moreover, in PMN, no

spontaneous polarization is observed and optical isotropy is retained even below the dielectric peak temperature, which suggested no ferroelectric phase transition in PMN. Later work on the structure of PMN revealed that no evidence for a structural phase transition is found and averaged cubic symmetry remains down to liquid helium temperature **[5,6]**. The experimental results reported by Burns *et al.* **[4]** in 1983 became a breakthrough of the studies on relaxors. They measured the temperature-dependence of the index of refraction for some relaxors including PMN in detail, and found a deviation from the linear temperature-dependence starting around 600 K with decreasing temperature in PMN. This result indicates that local polarizations are formed in the PMN crystal below 600 K, which is far above the dielectric peak temperature about 300 K, and Burns named the state with local polarizations "glassy polarization state". Nowadays, the temperature at which the local polarizations appear on cooling or disappear on heating is called "Burns temperature". These local polarizations are randomly oriented so that no macroscopic spontaneous polarization is observed, but the root-mean-square of the local polarization is non-zero, and the index of refraction shows a deviation from the linear temperature-dependence without polarizations below Burns temperature through the second electro-optic effect. In early 1990's, detailed structural investigations on PMN employing X-ray and neutron diffractometry were performed over a wide temperature range by a few research groups. Bonneau *et al.* **[5,6]** reported that PMN has an averaged cubic perovskite structure with random ionic shifts from the ideal lattice sites and random distribution of the *B*-site cations (space group $Pm\bar{3}m$ and lattice constant $a \cong 4$ Å) from 1023 to 5 K without significant evidence for a structural phase transition. However, some diffusion line tails appears in the diffraction patterns at about 600 K and their intensities increase with decreasing temperature, suggesting some local structural change with the formation of local polarizations. de Mathan *et al.* **[7]** performed a structural refinement on PMN at 5 K assuming two-phase coexistence of polar and nonpolar, i.e., ferroelectric and paraelectric phases. The X-ray and neutron static diffusion scattering lines were well described and the reliability factor was considerably improved by the two-phase coexistent structural model. The result of the refinement indicates that the ferroelectric phase is of rhombohedral symmetry ($R3m$) with ionic shifts along $<111>_{cub}$ directions and the volume ratio of the ferroelectric phase is estimated to be 20 % to the whole crystal at 5 K. Uesu *et al.* **[8]** repeated the structural refinement on PMN using two-phase structural model at seven temperatures below 300 K and investigated the temperature-dependence of the volume ratio of the rhombohedral phase. As a result, they found the ratio of the rhombohedral phase dramatically increases from 300 to 200 K with decreasing temperature but reaches the maximum of 20 % around 150 K. On the other hand, although the rhombohedral phase had been considered as ferroelectric on the analogy of the formation of the local polarizations

suggested by the index of refraction, there is no experimental confirmation on whether the rhombohedral phase is ferroelectric. In order to confirm it, they also measured the reflective intensity of second harmonic generation (SHG), and observed the similar temperature-dependence to the volume ratio of the rhombohedral phase **[9]**. The rhombohedral phase can be thus identified to be ferroelectric. The direct observations of the formation of the ferroelectric phase have been attempted using transmission electron microscope (TEM) **[10-13]**. Since the ferroelectric phase is of rhombohedral symmetry, it shows lattice distortions along $<111>_{cub}$ directions, which form contrast in a TEM image. Yoshida *et al.* **[13]** observed the formation of the ferroelectric regions as contrast in a TEM image, which becomes clear with decreasing temperature, especially below 200 K. In addition, they estimated the maximum size of the ferroelectric regions to be a few 10 nm. Summarizing these experimental results, the ferroelectric regions of rhombohedral symmetry with local polarizations nucleate around 600 K in the cubic paraelectric matrix and grow gradually with decreasing temperature but the growth ceases around 150 K. Consequently, these ferroelectric regions can not become macroscopic ferroelectric domains but ferroelectric nanoregions (FNR) with a size of a few 10 nm, and most of the crystal remains the cubic paraelectric phase down to liquid helium temperature. Thus two phases coexist below 600 K, and the phase transition as a macroscopic cooperative phenomenon does not occur after all. Fig.4.1 shows the schematic view of the crystal structure of PMN at room temperature reported by Uesu *et al.* **[8]**. Most of PMN crystal is the cubic paraelectric matrix, where Pb ions shift from the ideal *A*-sites by ~ 1/10 of the lattice constant of ~ 4 Å and distribute spherically around the ideal *A*-sites, and O ions distribute circularly around the ideal *X*-sites on the upper and lower sides of the [100] planes, which indicates tilting of the oxygen octahedra by ~ 5°, while Mg/Nb ions do not show remarkable shifts from the ideal *B*-sites. On the other hand, in FNR, O and Mg/Nb ions shift along $<111>_{cub}$ directions relative to Pb ions, but the axial angle is almost 90° and the lattice distortion is quite small. This result of the structural refinement is basically the same as the other results **[6,7]**. However, it is not clear why the size of the ferroelectric regions is restricted to nanoscale and a ferroelectric phase transition does not occur in PMN. Concerning this problem, the relation with the *B*-site cation arrangement has been pointed out.

1:1 *B*-site Cation Ordered Nanodomains

As mentioned in *Chapter 1*, in some $Pb(B'_{1/2}B''_{1/2})O_3$-type lead-based complex perovskites, e.g., $Pb(Mg_{1/2}W_{1/2})O_3$, the 1:1 ordered arrangement of B' and B'' ions is formed on the *B*-site sublattice. Considering alternate B^{I} and B^{II}-positions on the *B*-site sublattice, these positions form alternate B^{I} and B^{II}-layers along $<111>_{cub}$ directions, i.e., $-B^{I}-B^{II}-B^{I}-B^{II}-B^{I}-B^{II}-$ where the structural formula is represented as $Pb(B^{I}_{1/2}B^{II}_{1/2})O_3$ (Fig.4.2(a)). In the 1:1 order, the B^{I} and

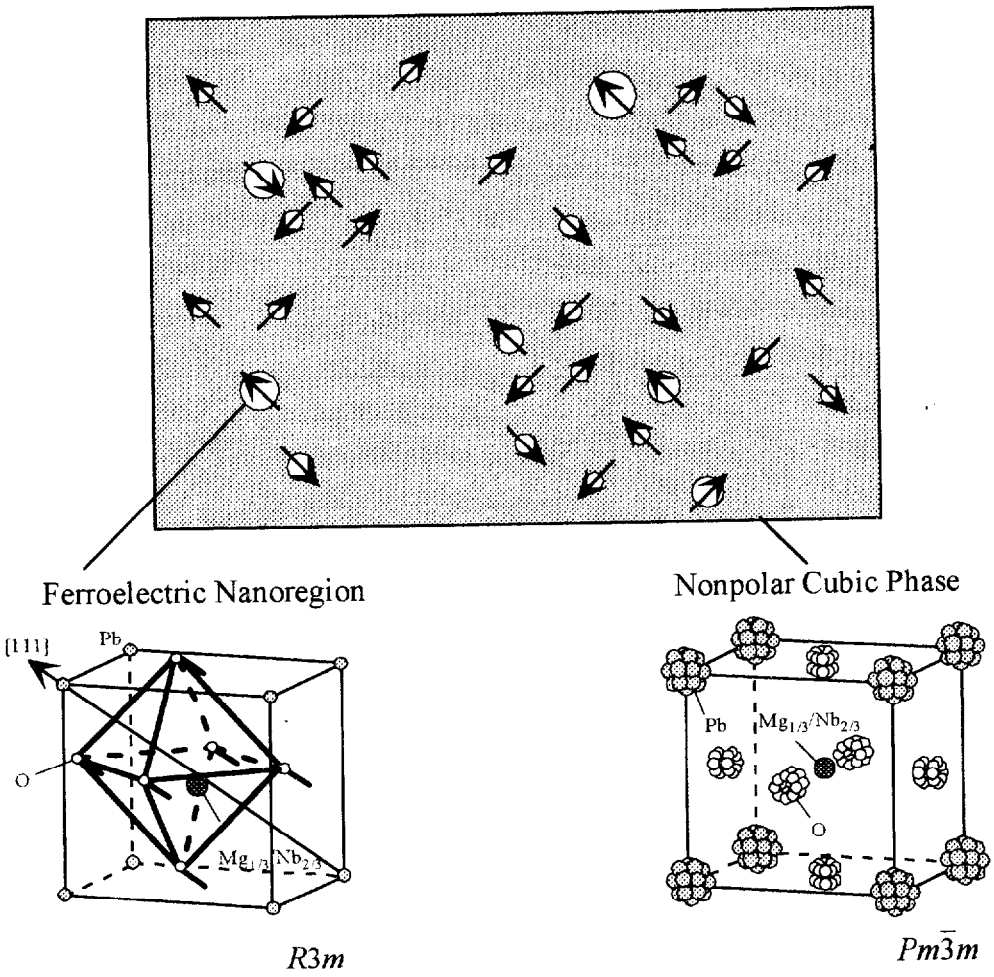

Fig. 4.1. Schematic crystal structure of PMN at room temperature determined from the results of the structural refinement by Rietveld analysis using powder neutron diffraction data [8]. PMN crystal is characterized by disordered cubic paraelectric matrix with significant ionic shifts from the ideal lattice sites and the formation of rhombohedral ferroelectric nanoregions formed in the matrix, the local polarizations of which is considered the origin of the characteristic dielectric behavior in PMN.

B^{II}-layers are exclusively occupied by B' and B'' ions, respectively, and the chemical composition is $Pb(B'_{1/2}B''_{1/2})O_3$. Therefore, the unit cell is of the superstructure with the double period of the basic perovskite unit cell, and the space group $Pm\bar{3}m$ is replaced by $Fm\bar{3}m$. In the diffraction image, the superlattice reflections caused by the unit cell doubling appear besides the basic perovskite reflections. On the other hand, in most of $Ba(B'_{1/3}B''_{2/3})O_3$-type barium-based complex perovskites, e.g., $Ba(Mg_{1/3}Nb_{2/3})O_3$, the 1:2 ordered arrangement of B' and B'' ions is formed. Considering alternate one B^{I}-position and two continuous B^{II}-positions

on the B-site sublattice, these positions form alternate one B^{I} and two continuous B^{II}-layers along $<111>_{cub}$ directions, i.e., $-B^{I}-B^{II}-B^{II}-B^{I}-B^{II}-B^{II}-$ where the structural formula is represented as $Pb(B^{I}_{1/3}B^{II}_{2/3})O_3$ (Fig.4.2(b)). Also in the 1:2 order, the B^{I} and B^{II}-layers are exclusively occupied by B' and B'' ions, respectively, and the chemical composition is $Pb(B'_{1/3}B''_{2/3})O_3$. Therefore, the unit cell is of the hexagonal symmetry with triple period of the basic perovskite unit cell, the space group of which is $P\bar{3}m1$. In the diffraction image, the superlattice reflections caused by the unit cell tripling is observed.

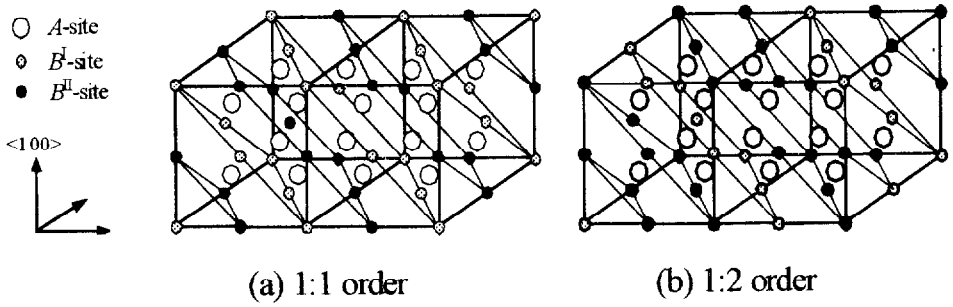

Fig.4.2. (a) 1:1 and (b) 1:2 ordered arrangement on the B-site sublattice. The former results in the unit cell doubling, the space group of which is $Fm\bar{3}m$, while the latter results in the unit cell tripling leading to change into the hexagonal symmetry of $P\bar{3}m1$.

In the case of PMN, if the ordered arrangement is formed on the B-site sublattice, the 1:2 ordered arrangement is expected because of 1:2 occupancy of Mg and Nb. Actually, there is no macroscopic ordered arrangement in PMN, namely space group $Pm\bar{3}m$ as reported by Bonneau *et al.* **[5,6]**. However, in the electron diffraction image of PMN, the superlattice reflections are observed at the (h+1/2, k+1/2, l+1/2) positions of the body-centered coordinate in the reciprocal space **[10-17]**, which arise from the face-centered cubic structure ($Fm\bar{3}m$) with the double period of the basic perovskite unit cell. Thus, Hilton *et al.* **[11]** named these reflections "F-spots". The F-spots are easily detected by electron but so weak as to be barely detected by synchrotron radiation X-ray using the single crystal. In addition, the intensities of the F-spots do not show temperature-dependence. The result of TEM observations indicates the existence of the 1:1 ordered regions in spite of 1:2 occupancy of Mg and Nb in PMN. The dark field TEM image formed by the F-spots shows that these regions have a size of 2 ~ 3 nm and are distributed over at least 30 % of the whole crystal **[17]**. Thus, these regions are called "1:1 ordered nanodomains".

For the actual ionic arrangement inside of the 1:1 ordered nanodomains, two models have been proposed so far **[15]**: one is the "space charge model" and the other is the "random layer model". In the space charge model, the B^{I} and B^{II}-layers in $Pb(B^{I}_{1/2}B^{II}_{1/2})O_3$ are exclusively

occupied by Mg and Nb. Thus the chemical composition of the ordered domains becomes $Pb(Mg_{1/2}Nb_{1/2})O_3$, and these domains are negatively charged, i.e., $[Pb(Mg_{1/2}Nb_{1/2})O_3]^{1/2-}$. However, it is unrealistic that such charged domains can exist stably. Newnham **[18]** proposed the structural model that the negatively charged ordered domains are surrounded by the positively charged Nb-rich regions $[PbNbO_3]^+$ to guarantee the charge neutrality over the whole crystal and to minimize the electrostatic energy. Assuming that these $PbNbO_3$ regions are composed of one layer, the size of the ordered domains corresponds to that of six unit cells, which agrees with the observed size of ~ 2 nm. The most important result of this model is the formation of random electric field locally induced by the charge unbalance in nanoscale, which has been considered as the primary factor preventing the ferroelectric phase transition in PMN **[19]**. Moreover, in this model, the evolution of ordering, i.e., the domain growth to the whole crystal is impossible because of the 1:2 occupancy of Mg and Nb and the minimization of the electrostatic energy. On the other hand, in the random layer model, the B^{II}-layer is exclusively occupied by Nb while the B^{I}-layer is occupied by the random distribution of Mg and Nb in the ratio of 2:1: this is the reason why the B^{I}-layer is called "random layer". Thus the chemical composition of the ordered domains becomes $Pb[(Mg_{2/3}Nb_{1/3})_{1/2}Nb_{1/2}]O_3$. In this case, the charge balance is maintained also in nanoscale, and the domain growth is expected to the whole crystal under a kinetically active condition according to thermodynamic stability.

In order to verify the two models, it has been attempted to observe the domain growth in PMN on thermal annealing under the various conditions **[11,15,20,21]**, but no domain growth has been observed. This fact has been supported the validity of the space charge model and the description of the local random field competing the long-range Coulomb force had been accepted for a long time. However, some researchers had doubted whether such phase segregation with charge unbalance was actually realized. Recently, Akbas and Davies **[22-24]** have investigated eagerly the domain growth in the PMN-family relaxors and found the domain growth in the $Pb(Mg_{1/3}Ta_{2/3})O_3$ (PMT) ceramic sample annealed at 1325 °C for 48 h. This fact indicates that the ordering is evolved under a kinetically active condition and supports the random layer model. They concluded that the absence of the domain growth in PMN was attributed to the existence of the thermodynamic order-disorder phase transition at a low temperature where the ionic movement is actually kinetically inactive. They also showed that a small amount of Zr doping to PMT crystal remarkably promote the domain growth and succeeded to obtain the PMT-PZ ceramic sample composed of the completely 1:1 ordered grains. In addition, the completely 1:1 ordered PMT-PZ still shows the relaxor behavior, which means the inhibition of the ferroelectric phase transition in PMN is not caused by the random field. They attributed the inhibition to the existence of B^{II} ions in the random layer, which gives rise to the local strain field. Thus, the regions with the arrangement of

$-B'-B''-B'-B''-B'-B''-$ can be ferroelectric but their expansion is inhibited at the part with $-B'-B''-B''-$. Recently, the direct observation of the ionic arrangement in the ordered domains has been attempted by the *Z*-contrast imaging method utilizing TEM **[25]**. The result suggests that the observed ionic arrangement is not of the space charge model but the random layer model. Nowadays, the random layer model is being generally accepted.

Unlike $Ba(B'_{1/3}B''_{2/3})O_3$-type perovskites where the 1:2 order is formed, $Pb(B'_{1/3}B''_{2/3})O_3$-type perovskites show a tendency to form the 1:1 order in spite of the 1:2 occupancy of *B'* and *B''*. The formation mechanism of the 1:1 order has not been clarified yet but considered to be closely related to the covalency of Pb. Burton **[26]** has reproduced this tendency by calculation using the empirical cluster expansion models.

Physical Models

So far, some physical models for PMN (or relaxors) have been proposed to explain the characteristic dielectric properties. These physical models can be classified broadly into two categories, i.e., "orientational glass model" and "domain state model". The common point to every model is the existence of FNR in the paraelectric matrix. However, their results for the nature of relaxors are a little different and the consistent physical model has not been established yet.

On the analogy of the superparamagnetism, Cross **[27]** proposed the "superparaelectric model" for relaxors extending the concept of the glassy polarization state reported by Burns *et al.* **[4]**. The local polarizations of FNR are considered to be thermally activated and dynamically fluctuating between the eight possible orientations along $<111>_{cub}$ directions above the dielectric maximum temperature. However, FNR grow gradually with decreasing temperature, and the activation energy of the thermal fluctuation, i.e., the barrier between potential minima increases with increasing the size of FNR, because it is known that E_a is proportional to the individual size of polar regions **[28]**. Thus, the polarizations are "trapped" at some minimum at low temperatures. Lu and Calvarin **[29]** calculated the dielectric behavior of PMN taking account of the distribution of the activation energy due to the size distribution of FNR and could reproduce the temperature- and frequency-dependence of the complex dielectric constant. Like this, the relaxor behavior can be explained by the superparaelectric model. In this sense, this model seems to point to the truth.

Developing the superparaelectric model, Viehland *et al.* **[30-32]** proposed the "dipolar glass model" on the analogy of spin glass system, where the strong interactions between magnetic moments are involved. Namely, they considered that the superparaelectric state resulted in the freezing at a finite temperature. They reported that the dielectric relaxation process of PMN in the middle frequency range can be well described by the V-F law (Fig.4.3):

$$f = f_0 \exp\left(-\frac{E_a}{k(T-T_f)}\right),$$

where E_a is the activation energy, T_f is the freezing temperature, and f_0 is the pre-exponential factor which usually has the value of $10^9 \sim 10^{12}$. They obtained $E_a = 0.0786$ eV, $T_f = 217.7$ K, and $f_0 = 10^{12}$. The fact that E_a and f_0 show physically acceptable values has also justified the dipolar glass model. According to this model, the local polarizations of FNR freeze cooperatively at around 220 K, showing critical slowing down. Since this model was proposed, a number of studies focused on the glasslike freezing in relaxors have been carried out and shown that the relaxation process obeys the V-F law. The glasslike freezing in PMN is supported by the existence of very slow dynamics and the long-time relaxation with logarithmic decay reported by Colla *et al.* **[33]**. However, Christen *et al.* **[34]** doubted the physical meaning of the description with the V-F law and reanalyzed the low frequency data reported by Colla *et al.* **[33]** with the phenomenological description for the high and low frequency dielectric behavior of PMN in terms of α(primary)- and β(secondary)-relaxation process in a glass former, where a relatively high frequency β-process takes over when the characteristic α-relaxation time becomes extremely long, showing continuous slowing down around the take-over temperature.

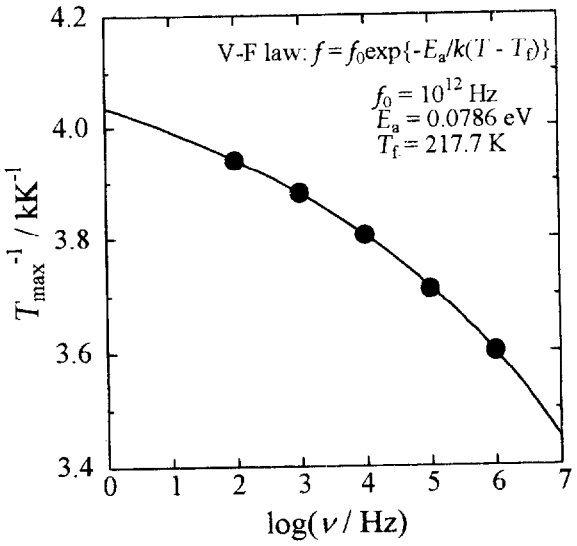

Fig. 4.3. Frequency f *vs.* maximum temperature T_{max} of the dielectric loss of PMN reported by Viehland *et al.* **[30-32]**. This result suggests that the dielectric relaxation process should obey the Vogel-Fulcher (V-F) law, which indicates cooperative freezing of the local polarizations of FNR at a finite temperature.

Originally, the dipolar glass model was established on the analogy of the spin glass system. Actually, however, the ideal dipolar glass whose behavior can be explained by the Sherrington-Kirkpatrick (S-K) model for spin glasses has not been found so far because the dipolar glass system is more complicated than the related spin glass system due to the long-range nature of the dipolar interactions and the coupling of the dipolar system with the lattice system. Thus it seems to be somewhat unreasonable to apply the model for spin glasses directly to dipolar glasses, especially relaxors. Very recently, Blinc *et al.* **[35,36]** proposed the "spherical random bond-random field (SRBRF) model" based on the results of NMR experiments for PMN. In the SRBRF model, the term expressing the interaction between the polarization and the random field is introduced to the Hamiltonian of S-K model. They showed that the temperature-dependence of the Edwards-Anderson order parameter and the nonlinear dielectric coefficient of PMN above the expected freezing temperature can be well described by the SRBRF model. According to the SRBRF model, the nonlinear dielectric coefficient should show a sharp peak under the presence of the weak random fields or diverge under the absence of the random field at the freezing temperature, while it should vanish at the ferroelectric phase transition. Thus, nonlinear dielectric constant measurements have been actively performed **[37-40]** as an effective means to investigate the existence of a finite freezing temperature. The measured nonlinear dielectric coefficient showed a tendency to increase at the expected freezing temperature with decreasing temperature, which might indicate the existence of a finite freezing temperature, but no peak was observed. This failure in the observation was attributed to the dynamic nature of the conventional dielectric spectroscopy because the expected peak is the static response at the freezing temperature.

On the other hand, Westphal *et al.* **[19]** proposed the "random field induced domain state model" based on the space charge model for the *B*-site cation arrangement. They stressed that PMN is ferroelectric by nature but the ferroelectric phase transition is smeared by the quenched random field arising from the negatively charged ordered domains. Consequently, the ferroelectric phase transition as a macroscopic cooperative phenomenon does not occur in PMN and the individual size of the ferroelectric regions is restricted to nanoscale, and they called this state "domain state". They measured the time-dependence of the birefringence of PMN under a bias electric field and observed that the birefringence increases with a jump (Barkhausen jump), which indicates that FNR grow into macroscopic ferroelectric domains when the random field is overcome by a bias field. Actually, PMN can be ferroelectric at ~ 213 K under a bias field above the threshold field strength of ~ 1.75 kV/cm **[41,42]**, and this phenomenon is called "electric field-induced phase transition". Thus, they concluded that the relaxor state in zero bias field is a ferroelectric state broken up into nanodomains under the constraint of quenched random electric field, which excludes the orientational glasslike freezing. Since this model is

established on the space charge model, it seems that this model can not be approved if the random layer model is correct. However, if the random electric field is replaced by the strain field argued in the random layer model, the similar concept might be applied. Thus, this model is simply called "domain state model" here.

In my opinion, both "orientational glass model" and "domain state model" point to an aspect of the nature of PMN (or relaxors) because a glasslike dielectric relaxation phenomenon is surely observed in PMN and this phenomenon is surely caused by the ferroelectric regions whose size is restricted to nanoscale by some reason. However, these models are said to be alternative. The essential difference between the two is attributed to whether the local polarizations of FNR freeze cooperatively at a finite freezing temperature. Namely, the orientational glass model argues the existence of a finite freezing temperature, while the domain state model does not admit its existence because the ferroelectric phase should be realized if FNR interact cooperatively with each other, and the state with the cooperative freezing is not ferroelectric nanodomain state any longer. Therefore, in the domain state model, each FNR should behave independently. Such a state is a superparaelectric state as an equilibrium state, showing a blocking phenomenon of the local polarizations as a nonequilibrium phenomenon, as discussed in the ferromagnetic fine particle system **[43]**. In this case, the dielectric relaxation process is expected to obey the Arrhenius law in stead of the V-F law. However, the actual dielectric relaxation process seems to obey the V-F law.

From the results of the structural studies on PMN, it has been suggested that FNR nucleate and grow in the paraelectric matrix with decreasing temperature. Namely, PMN has the hetero-structure composed of two phases below 600 K. Nowadays such hetero-structure is considered to be essential to relaxors, and every physical model for relaxors is established on the hetero-structure. In general, however, two phases can coexist at a first-order phase transition point, where an anomaly in the heat capacity should be observed. Even if the ferroelectric phase transition in relaxors is smeared by some reasons, e.g., random field or strain field, as argued in the domain state model, a heat capacity anomaly would be expected due to the formation of FNR. Therefore if there is no heat capacity anomaly in relaxors, the domain state model should be dismissed. The heat capacity of PMN has been measured by Strukov *et al.* **[44]** using an adiabatic method between 7 and 290 K, and by Fouskova *et al.* **[45]** using DSC between 140 and 790 K. Their heat capacity data of PMN are shown in Fig.4.4 together with the dielectric constant. Strukov *et al.* suggested that no remarkable heat capacity anomaly was observed below 290 K, where the dielectric peak is observed below the middle frequency range. On the other hand, Fouskova *et al.* assumed the lattice contribution using a single Debye formula with characteristic temperature Θ_D of 422.1 K and argued the existence of heat capacity

anomalies around 300 K and 700 K, where the dielectric peak is observed and the nucleation of FNR takes place, respectively. However, both results were not in good agreement in the overlapping temperature range, and it has been uncertain which of the two results is reliable. Such uncertainty of the experimental results might originate from both the essential complexity of relaxors and experimental restrictions such as precision, accuracy, and measurable temperature range: the temperature range of the measurement by an adiabatic method is insufficient to discuss the existence of a heat capacity anomaly in PMN, while fundamentally, DSC is not suitable for heat capacity measurements.

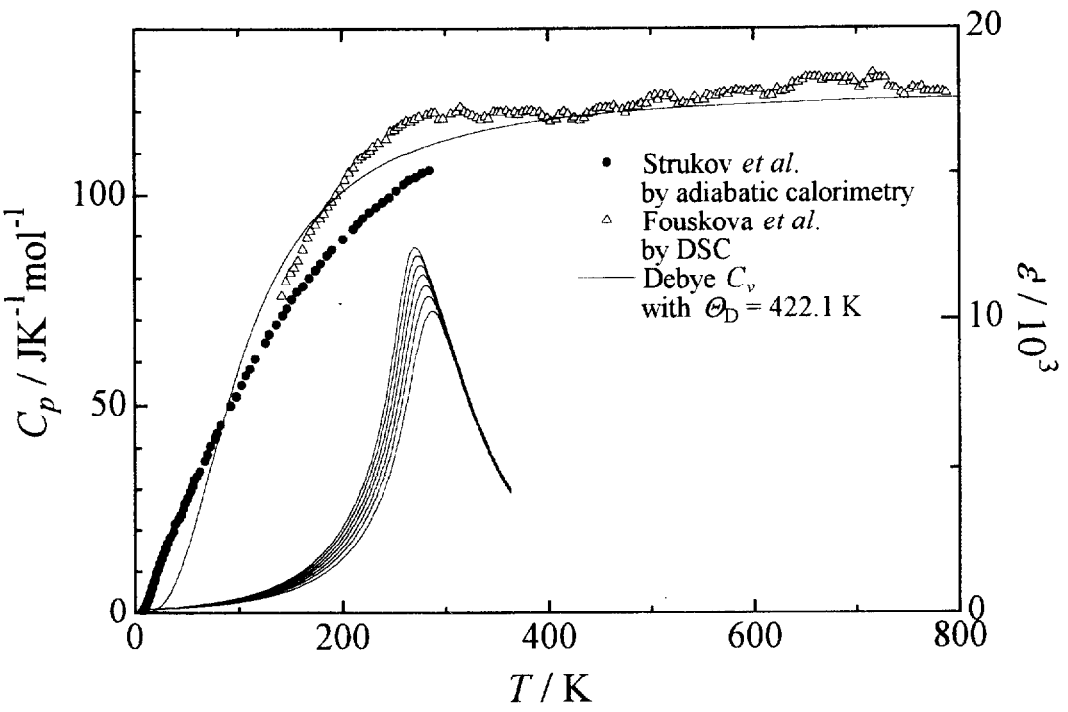

Fig.4.4. Heat capacity of PMN reported previously. Solid circles are the data measured by Strukov *et al.* **[44]** using an adiabatic method, while triangles shows the data measured by Fouskova *et al.* **[45]** using DSC. Both are in disagreement with each other. Strukov *et al.* suggested that there is no anomaly around the dielectric peak temperature, while Fouskova *et al.* argued the existence of some anomalies around the dielectric peak and around 700 K, which is close to the "Burns temperature", assuming the shown Debye heat capacity as the lattice contribution. However, this base line is invalid as far as taking the result by Strukov *et al.* into account.

In addition, the recent interests on PMN is focused on the state in the low temperature region below ~ 220 K, which is the freezing temperature expected by the dipolar glass model. However, there has been no studies on the thermodynamic properties in the state of PMN below ~ 220 K. In the heat capacity of PMN in this temperature region, some interesting features might be observed. For further understanding of the nature of relaxors, thermodynamic information is indispensable, and the precise data of the heat capacity over a wider temperature range are highly desired. In this chapter, based on the results of the precise heat capacity measurements for PMN up to 420 K, the properties of PMN are discussed in detail. In order to examine the findings on PMN, the heat capacity measurements were also performed for the fist time for PMT, which is a member of the PMN-family relaxors with a similar peak of dielectric constant around 200 K, and $Ba(Mg_{1/3}Ta_{2/3})O_3$ (BMT), which is a member of the nonrelaxor barium-based complex perovskites.

4.1. Experimental

4.1.1. Sample Preparation

In many cases, a two-valence metal oxide AO and a five-valence metal oxide B_2O_5 react at a high temperature and form a columbite AB_2O_6 or pyrochlore oxide $A_2B_2O_7$. Especially, lead-based pyrochlore oxides $Pb_2Nb_2O_7$ and $Pb_2Ta_2O_7$ can be easily obtained by reacting PbO with Nb_2O_5 and Ta_2O_5, respectively, at about 800 °C, and its high reactability had been an obstacle to obtain pure $Pb(B'_{1-x}Nb_x)O_3$ and $Pb(B'_{1-x}Ta_x)O_3$ perovskite oxides. For example, in the synthesis of PMN powder sample, when the starting powder materials PbO, MgO, and Nb_2O_5 are mixed in stoichiometric proportions and then heated at a high temperature, a resultant product usually includes a pyrochlore phase besides the perovskite phase, where the pyrochlore phase is considered to have a little complex stoichiometry of $Pb_{1.83}Mg_{0.28}Nb_{1.71}O_{6.83}$. It is impossible to separate the once formed pyrochlore from the perovskite because both chemical properties are quite similar contrary to the quite different physical properties: the dielectric constant of the pyrochlore is very small (~ 10) and the existence of the pyrochlore impurity in the perovskite lowers strikingly the quality of the material. Industrially, since dielectric materials with a ceramic form are widely used, the formation of the pyrochlore phase is a troublesome problem. In order to avoid its formation, it is necessary to mix the starting powder materials as uniformly as possible, and the starting materials were usually mixed using a mechanical method such as ball-milling for a long time. On the other hand, a synthesis process has been also developed through a chemical mixing method using the oxalate and

nitrate of component cations [46], although this process is unsuitable for mass-producing. In 1982, Swartz and Shrout [47] developed a method for the synthesis of PMN, which can be also applied for other lead-based complex perovskite oxides, where PMN was synthesized via a precursor with the columbite form. They prepared a ferrocolumbite ($FeNb_2O_6$) type metal oxide, namely $MgNb_2O_6$ prior to the synthesis of PMN, and today, this method is often called "columbite precursor method". With this method, they succeeded to synthesize pyrochlore-free PMN. However, since surviving Nb_2O_5 in $MgNb_2O_6$ can be a trigger for the formation of the pyrochlore phase, they recommended mixing a few mole percents excess MgO in the synthesis of $MgNb_2O_6$. Today, this method and its derivative are widely employed in the synthesis of lead-based complex perovskite oxides. In this study, single crystals synthesized by flux method were used for measurements, and it might not be necessary to prepare the precursors in the synthesis of single crystals. However, precursors were prepared taking into account the necessity of powder samples, and they were used for the synthesis of single crystals.

$Pb(Mg_{1/3}Nb_{2/3})O_3$

The single crystals of PMN were prepared by a PbO-flux method. Prior to the synthesis of PMN, the precursor $MgNb_2O_6$ was synthesized by a solid phase reaction technique. Powder materials of MgO (Rare Metallic Co., Ltd., 99.9 %) and Nb_2O_5 (Mitsui Mining & Smelting Co., Ltd., Reagent Grade) were mixed in stoichiometric proportions using an ethanol medium for 1 h. This powder mixture was put in an alumina crucible and then placed in a furnace. The powder mixture was heated in air at 1100 °C for 12 h. The heated powder was reground and then reheated at 1100 °C for 24 h. The resultant powder was identified to be a single phase of the columbite structure by powder X-ray diffraction. Next, the precursor $MgNb_2O_6$ and PbO (Rare Metallic Co., Ltd., 99.99 %) were mixed in the mass ratio of 1:7.5. This powder mixture was put in a platinum crucible and then the crucible covered with a platinum lid was placed in the furnace. The crucible was rapidly heated in an oxygen atmosphere up to 1240 °C. After soaking at this temperature for 4 h in order to dissolve $MgNb_2O_6$ in PbO- flux, the crucible was slowly cooled down to 940 °C at the rate of 1.5 °C/h to promote the crystallization and then brought to room temperature by turning off the furnace. The flux was dissolved with 30 % hot nitric acid and the products with a single crystal form were isolated. The crystals of about 2 mm in size were separated from the products but there were two types of single crystals: one has a light yellow color and a larger amount, while the other has an orange color and a smaller amount, and they were easily separated by hand. Both crystal structures were investigated by powder X-ray diffraction technique, and it was found that the former is a single phase of the perovskite structure and the latter is a single phase of the pyrochlore structure. Therefore the crystals with a light yellow color can be considered as PMN and its crystal structure was

identified to be cubic perovskite ($Pm\bar{3}m$) at room temperature (Fig.4.5).

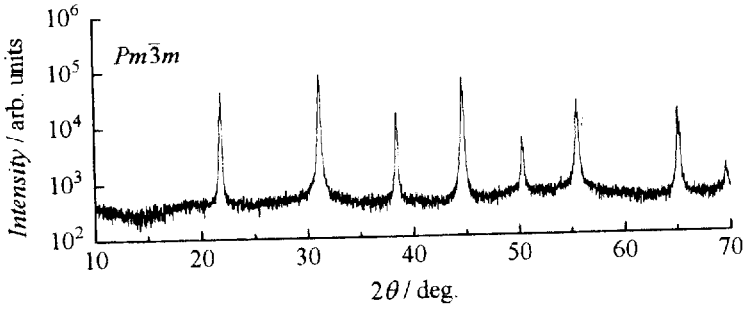

Fig. 4.5. Powder X-ray diffraction pattern of PMM.

$Pb(Mg_{1/3}Ta_{2/3})O_3$

The single crystals of PMT were prepared in a similar procedure to PMN. The same starting materials were used except for Nb_2O_5, which was replaced by Ta_2O_5 (Hikotaro Shudzui Co., Ltd., 99.9 %). Prior to the synthesis of PMT, the precursor $MgTa_2O_6$ was prepared in the same procedure to $MgNb_2O_6$ except that the heating temperature was 1300 °C. The resultant powder was identified to be a single phase of the columbite structure by powder X-ray diffraction. Next, the precursor $MgTa_2O_6$ and PbO were mixed in the mass ratio of 1:8. After that, the single crystals of PMT were obtained by following the same procedure as PMN. In the synthesis of PMT, two types of single crystals were also obtained: one has an orange color and a smaller amount, while the other has a light brown color and a larger amount. As a result of investigation using powder X-ray diffraction technique, it was also found that the former is a single phase of the pyrochlore structure and the latter is a single phase of the perovskite structure. Therefore the crystals with a light brown color can be considered as PMT and its crystal structure was identified to be cubic perovskite ($Pm\bar{3}m$) at room temperature (Fig.4.6), but as pointed out by Akbas *et al.* **[22]**, diffuse scattering line considered to be due to the 1:1 ordered nanoregion of Mg and Ta were observed around $2\theta = 19°$.

$Ba(Mg_{1/3}Ta_{2/3})O_3$

The ceramic sample of BMT was prepared by standard solid phase reaction techniques. Powder materials of $BaCO_3$ (Rare Metallic Co., Ltd., 99.99 % + Sr = 1.7 ppm) and previously prepared $MgTa_2O_6$ were mixed in stoichiometric proportions using an ethanol medium for 1 h. This powder mixture was put in an alumina crucible and then placed in a furnace. The powder mixture was heated in air at 1200 °C for 12 h. At this time, the crystal structure of the resultant powder was checked by powder X-ray diffraction technique, and it was identified to be hexagonal perovskite ($P\bar{3}m1$) with the partial 1:2-order of the arrangement of Mg and Ta

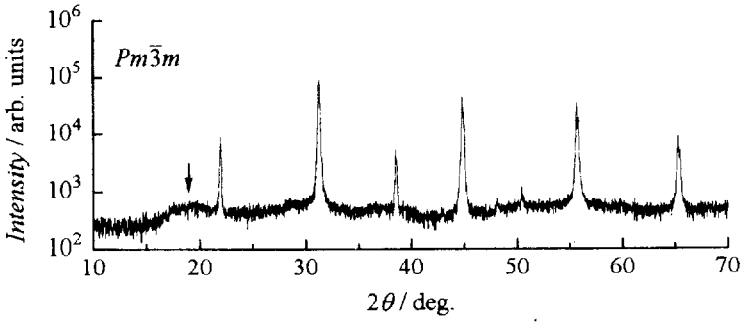

Fig. 4.6. Powder X-ray diffraction pattern of PMT. Around $2\theta = 19°$ (arrowed point), weak diffuse scattering not observed in PMN is observed, as pointed out by Akbas *et al.* **[22]**. This is considered due to the 1:1 ordered domains, which are easier to grow in PMT than PMN.

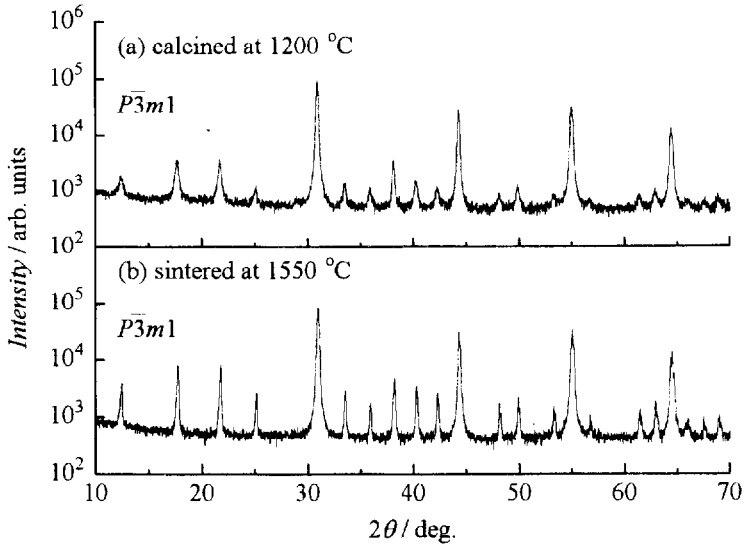

Fig. 4.7. Powder X-ray diffraction patterns of BMT: (a) the pattern after heated at 1200 °C for 12 h and (b) that of the ceramic sample sintered at 1550 °C for 24 h. Both are of the hexagonal symmetry, which indicates the 1:2 ordering of Mg and Ta, but the intensities of the corresponding reflections to the unit cell tripling become larger by the thermal treatment at a high temperature, which implies the evolution of the ordered arrangement.

on the *B*-site sublattice (Fig.4.7(a)). Next, this resultant powder was pressed into pellets with 14 mm diameter and about 10 mm thickness. These pellets were put in the same crucible and then placed in a furnace. The pellets were sintered in air at 1550 °C for 24 h. The obtained

ceramic sample was colorless. The final crystal structure of the resultant ceramics was checked, and it was found that the intensities of the superlattice reflections due to the 1:2-order increased (Fig.4.7(b)), which suggested the progress of the ordering.

4.1.2. Heat Capacity Measurements

$Pb(Mg_{1/3}Nb_{2/3})O_3$

The heat capacity of PMN was measured by an adiabatic method between 13 and 420 K. The amount of the sample put into the calorimeter vessel was 7.6933 g (23.654 mmol). The contribution of the sample to the total heat capacity was 39, 42, 45, and 45 % at 100, 200, 300, and 400 K, respectively. In order to obtain the heat capacity data below 13 K, the heat capacity of PMN was also measured between 2 and 60 K by a relaxation method. The mass of the ceramic sample used for the measurement was 6.460 mg (19.86 μmol). The contribution of the sample to the total heat capacity was 32, 66, 78, 76, 71, 65, 59 and 55 % at 2, 5, 10, 20, 30, 40, 50 and 60 K, respectively.

$Pb(Mg_{1/3}Ta_{2/3})O_3$

The heat capacity of PMT was measured by an adiabatic method between 13 and 420 K. The amount of the sample put into the calorimeter vessel was 8.0113 g (20.866 mmol). The contribution of the sample to the total heat capacity was 70, 44, 37, 40, 41 and 41 % at 20, 50, 100, 200, 300, and 400 K, respectively. In order to obtain the heat capacity data below 13 K, the heat capacity of PMT was also measured between 2 and 60 K by a relaxation method. The mass of the ceramic sample used for the measurement was 16.570 mg (43.159 μmol). The contribution of the sample to the total heat capacity was 55, 82, 90, 88, 85, 81, 77 and 73 % at 2, 5, 10, 20, 30, 40, 50 and 60 K, respectively.

$Ba(Mg_{1/3}Ta_{2/3})O_3$

The heat capacity of BMT was measured by an adiabatic method between 13 and 420 K. The amount of the sample put into the calorimeter vessel was 7.2219 g (22.995 mmol). The contribution of the sample to the total heat capacity was 33, 34, 34, 39, 41 and 42 % at 20, 50, 100, 200, 300, and 400 K, respectively. In order to obtain the heat capacity data below 13 K, the heat capacity of BMT was also measured between 2 and 60 K by a relaxation method. The mass of the ceramic sample used for the measurement was 27.044 mg (86.111 μmol). The contribution of the sample to the total heat capacity was 19, 29, 40, 67, 77, 79, 79 and 77 % at 2, 5, 10, 20, 30, 40, 50 and 60 K, respectively.

4.1.3. Dielectric Constant Measurements

$Pb(Mg_{1/3}Nb_{2/3})O_3$

The dielectric constant and loss of PMN were measured between 15 and 370 K with frequencies of 1, 3, 10, 30, 100, and 1000 kHz. A single crystal with suitable size was selected and then polished with rough sandpaper to be a parallel-plate shape. Both surfaces of the parallel plates were polished out with fine sandpaper. Gold was spattered on both surfaces to be electrodes of a parallel-plate capacitor. Gold wires with the diameter of 0.05 mm were connected to each electrode with silver paste (Engelhard K.K.). The thickness and the square of the sample were 0.20 mm and 1.96 mm^2, respectively. The effective voltage of the measurement AC field was 1 V_{rms}, and so the field strength was 50 V_{rms}/cm, which was weak enough to measure the dielectric property. The measurements were carried out in both cooling and heating runs with the rate of 1 K/min and no hysteresis was observed between both runs.

$Pb(Mg_{1/3}Ta_{2/3})O_3$

The dielectric constant and loss of PMT were measured in the same condition as PMN. The procedure of the sample preparation was also the same as PMN. The thickness and the square of the sample were 0.15 mm and 2.35 mm^2, respectively. The effective voltage of the measurement AC field was 1 V_{rms}, and so the field strength was 67 V_{rms} /cm, which was also weak enough. The measurements were carried out in both cooling and heating runs with the rate of 1 K/min and no hysteresis was also observed between both runs.

$Ba(Mg_{1/3}Ta_{2/3})O_3$

The dielectric constant of BMT was measured between 100 and 420 K with frequencies of 1, 3, 10, 30, 100, 300, 1000, 3000, and 10000 kHz. The procedure of the sample preparation was the same as PMN and PMT. The thickness and the square of the sample were 0.39 mm and 13.9 mm^2, respectively. The effective voltage of the measurement AC field was 1 V_{rms}, and so the field strength was 26 V_{rms} /cm, which was also weak enough. The measurements were carried out in both cooling and heating runs with the rate of 1 K/min and no hysteresis was also observed between both runs.

4.3. Result and Discussion

First of all, the comparison of the present with previous results of the heat capacity measurements on PMN is shown in Fig.4.8. As seen at a glance, the present data is in good agreement with the data measured by Strukov *et al.* **[44]** using an adiabatic method, while the data obtained by Fouskova *et al.* **[45]** using DSC is not in good agreement with the results of adiabatic calorimetry. In addition, the lattice contribution as the Debye heat capacity assumed by Fouskova *et al.* is clearly invalid in comparison with the low temperature data by an adiabatic method, and their argument on the existence of a heat capacity anomaly around 300 K seems to lose its persuasiveness. However, some signature related to the mechanism causing the unique dielectric response should be observed in the heat capacity that has no selection rule, and it is necessary to investigate more in detail using accurate heat capacity data.

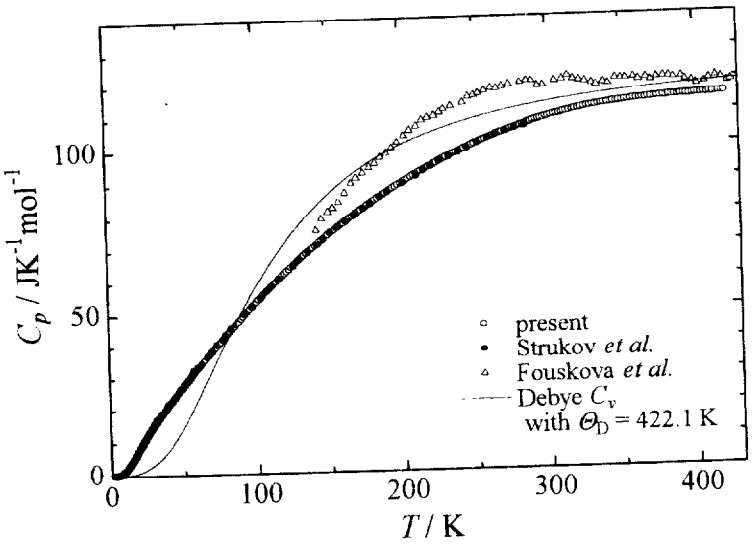

Fig. 4.8. Comparison between the present and previous results of the heat capacity measurements on PMN. Both results of an adiabatic method are in good agreement.

The measured heat capacity of PMN and PMT are shown in Fig.4.9. At a glance, no remarkable anomaly is seen in the both heat capacity curves, which seem to be an ordinary lattice contribution. PMT shows the larger heat capacity than that of PMN at low temperatures, which is probably due to the mass effect of heavier Ta ions, as seen between PT and PZ. Since both compounds have the same crystal structure of the perovskite, both heat capacity curves are expected to approach asymptotically the classical value of Dulong-Petit law, $15R$, without any remarkable features as temperature increases. However, the two curves intersect at 250 K,

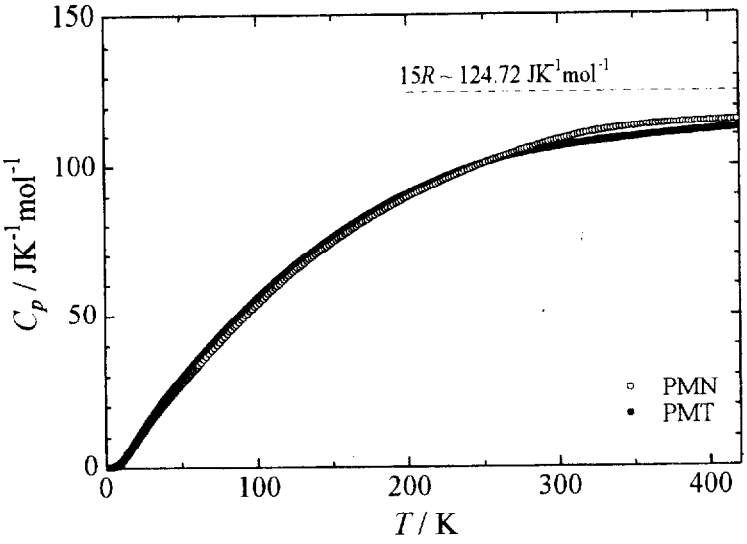

Fig. 4.9. Measured heat capacity of typical relaxors PMN and PMT. Heat capacity curves intersects at 250 K, which implies the existence of some anomaly around this temperature.

which implies some effects causing extra heat capacity at least in PMN. Thus, the heat capacity difference, ΔC_p, of PMN and PMT from $BaTiO_3$ (BT) and $PbTiO_3$ (PT) is considered at the beginning, and it is shown in Fig.4.10. Fig.4.10(a) shows ΔC_p of PMN and PMT from BT, where the calculated heat capacity in *Chapter 3* is used for the heat capacity of BT because there are heat capacity anomalies in the measured heat capacity of BT, which are obstructive to extract the singularities in the heat capacity of PMN and PMT. In this figure, two very interesting features are found in low and high temperature regions, respectively. One is the Schottky anomaly-like difference around 50 K and the other is a shoulder-like difference around 200 K for PMT and around 300 K for PMN. On the other hand, Fig.4.10(b) shows ΔC_p from PT, where the similar features to Fig.4.10(a) are also seen, but some additional contribution is found around 20 K in both PMN and PMT, similar to antiferroelectric $PbZrO_3$ (PZ). The origins of these quite singular features in PMN and PMT are discussed in detail as follows.

Anomalous Large Heat Capacity in a Low temperature Region

Here, the low temperature heat capacity difference among the lead-based perovskites, i.e., PT, PZ, PMN, and PMT, is considered and shown in Fig.4.11 as the C_pT^{-3} *vs.* log$T$ plot. It is very surprising that PMN and PMT relaxors show very larger values of the heat capacity than those of PT and PZ below 50 K, in spite of the same lead-based perovskites. Especially, at 2 K, the heat capacity value of PMN and PMT is about three times larger than that of PT and PZ.

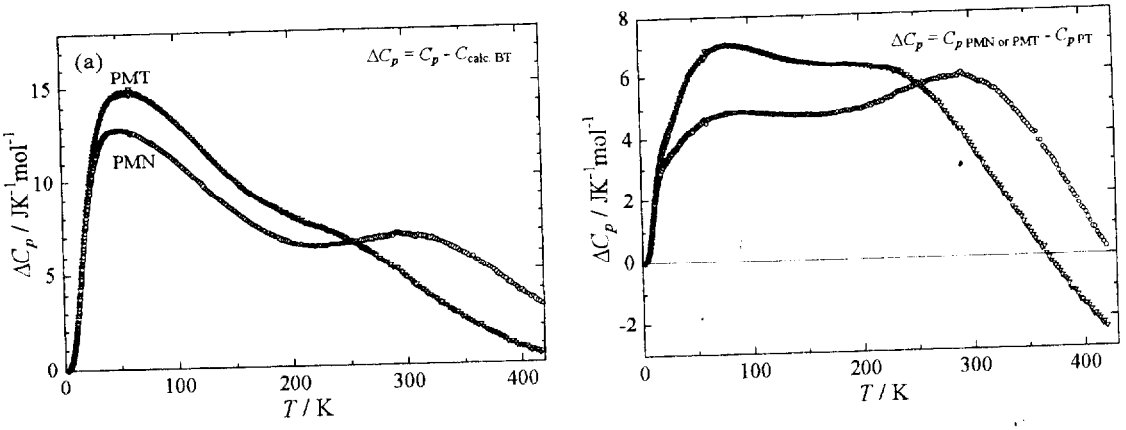

Fig. 4.10. Heat capacity difference of PMN and PMT from the normal perovskite ferroelectrics (a) $BaTiO_3$ (BT) and (b) $PbTiO_3$ (PT), where the calculated heat capacity of BT in *Chapter 3* is used as the heat capacity of BT because the measured heat capacity of BT has three anomalies, which make difficult to extract the singularities of the relaxors by comparison.

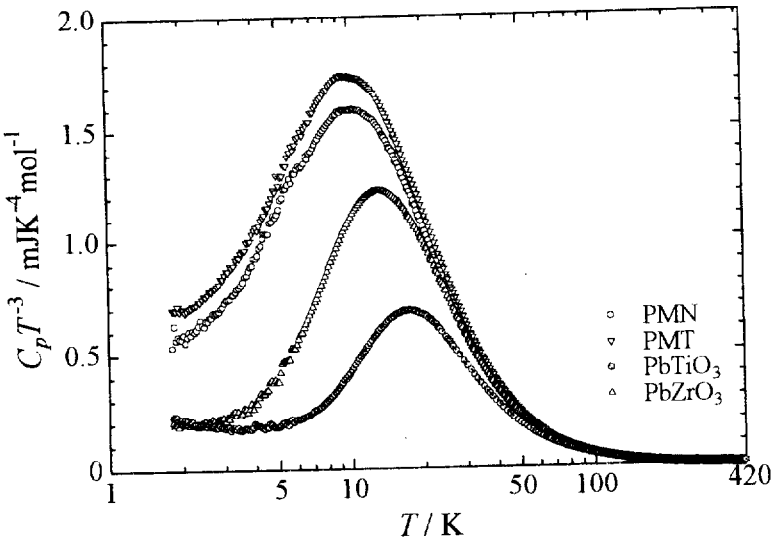

Fig. 4.11. Comparison of low temperature heat capacity between the relaxors and the normal perovskite ferroelectrics in the C_pT^{-3} *vs.* log$T$ plot.

In *Chapter 3*, it was shown that the elastic and calorimetric Debye temperatures of PT and PZ are in good agreement with each other, and estimated to be about 220 K assuming that at low temperatures only the acoustic phonons with $3N$ degrees of freedom can be excited. On the other hand, when the calorimetric Debye temperatures of PMN and PMT are estimated under

the same assumption, those values become 150 and 140 K, respectively. However, these values are very small relative to PT and PZ. If the large heat capacity value of PMN and PMT is actually attributed to the contribution of the acoustic phonons, the elastic and calorimetric Debye temperatures should agree with each other like in PT and PZ. Thus, the elastic Debye temperature was also estimated for PMN using the elastic data reported previously, while unfortunately, there is no available elastic data for PMT. Since the PMN crystal is of the cubic symmetry, the following equation for isotropic crystals can be used:

$$\Theta_{\mathrm{D}}^{\mathrm{el}} = \frac{h}{k}\left(\frac{9nN}{4\pi V}\right)^{1/3}\left(\frac{1}{v_{\mathrm{l}}^3}+\frac{2}{v_{\mathrm{t}}^3}\right)^{-1/3}. \qquad (4.1)$$

The results of the estimation are tabulated in Table 4.1. It is obviously seen that the elastic Debye temperatures of PMN are completely different from the calorimetric one, and this discrepancy in PMN has been already pointed out by Lawless *et al.* **[48]**, which indicates the existence of some additional low energy excitations in PMN.

	PMN				PMT	$PbTiO_3$		$PbZrO_3$	
	[49]	**[50]**	**[51]**	C_p	C_p	elastic	C_p	elastic	C_p
${}^{15N}\Theta_{\mathrm{D}}$ / K	397	376	382	257	240	372	380	396	370
${}^{3N}\Theta_{\mathrm{D}}$ / K	232	220	223	150	140	218	222	232	216

Table. 4.1. Estimated elastic and calorimetric Debye characteristic temperature for PMN, PMT, $PbTiO_3$, and $PbZrO_3$. The numbers in the brackets refers to the reference number.

Ackerman *et al.* **[52]** reported that some crystalline solids with topological disorder including PMN show the characteristics of glasses, i.e., the existence of an additional T-linear term in the heat capacity, T^2-dependence below 1 K and plateau around 10 K in the thermal conductivity, and a minimum in the dielectric constant around 0.1 K at about 10^4 Hz, associated with the two-level excitations **[53,54]**. The comparison of the present data with the data reported by Ackerman *et al.* is shown in Fig.4.12 as the double logarithmic C_pT^{-3} *vs.* T plot. Their data were measured in different facilities below and above 1.5 K, but there is no detailed description on the measurements in their report. Above 3 K, a qualitative agreement can be seen between both, e.g., the maximum of C_pT^{-3} at 10 K. On the other hand, below 3 K, their data show the tendency to diverge with decreasing temperature, which shows the existence of a T-linear term, while the present data do not show such a tendency between 2 and 3 K. Although there is no explaining the behavior below 2 K in detail because data below 2 K could not be obtained in the present study due to the restriction on the apparatus, their data below 1.5 K may be connected smoothly with the present data. In either case, there is no doubt the

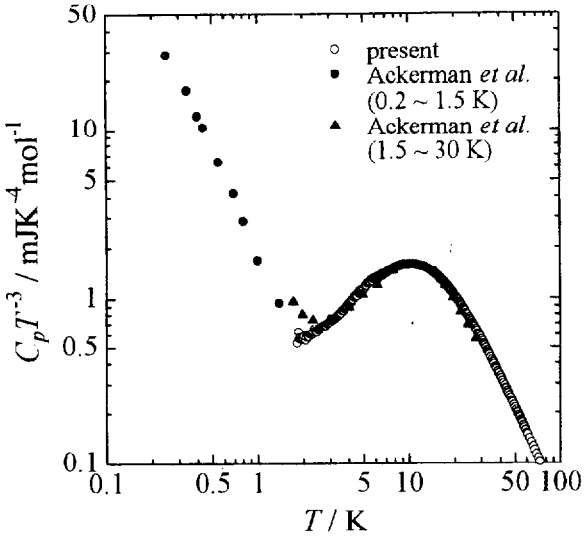

Fig. 4.12. Comparison of the present and previous results of low temperature heat capacity measurements on PMN in the C_pT^{-3} *vs.* log$T$ plot, where the date are shown in double logarithmic scale because of the existence of the T-linear term in the data reported by Ackerman *et al.* **[52]**.

existence of some additional low energy excitations in PMN.

Zeller and Pohl **[55]** performed heat capacity measurements on crystalline and glassy SiO_2, and found the existence of a T-linear term besides the normal T^3-term in the heat capacity of SiO_2 glass. After that, in order to explain the appearance of the T-linear term, Anderson *et al.* **[56]** proposed the phenomenological model that a number of two-level systems with the same split width are distributed uniformly in a glass and the two-level excitations arise from the quantum mechanical tunneling of oxygen ion between potential energy minima at very low temperatures, and showed skillfully that the T-linear term is introduced into the heat capacity. However, there has been no experimental support on this model. In addition, it has been shown by inelastic neutron scattering experiments **[57]** that in SiO_2 glass, there is another additional low energy excitation besides the two-level excitations and the density of vibratinal states around 1.5 THz is about three times greater than the Debye-type density of states whose characteristic temperature is estimated from the sound velocity. Nowadays, the existence of low energy excitations in this frequency region is considered as a characteristic of glasses, and called "Boson peak".

Although the mechanism causing the T-linear term in the heat capacity of PMN is unclear, there are the structural features showing a common point to the two-level excitation model. For example, the results of structural refinement **[5-8]** indicate that in the cubic paraelectric

matrix, Pb ions and oxygen octahedra are situated on a multi-minimum potential, and the quantum mechanical tunneling of Pb or O ions might occur at very low temperatures. On the other hand, in the superparaelectric model proposed by Cross [27], the local polarizations of FNR are thermally fluctuating between a multi-minimum potential at high enough temperatures but trapped at an either potential minimum at low enough temperatures (or frozen below about 220 K according to the dipolar glass model [30-32]), and it is possible to interpret the existence of the T-linear term with the excitations between the trapped or frozen polarizations. It is also very interesting that in PMN, the existence of the low energy excitation similar to the Boson peak is observed around 1.5 THz by inelastic neutron scattering [57,58] and Raman scattering experiments [57,59,60]. Concerning this low energy excitation, a very interesting feature is seen in Fig.4.11: the maximum in C_pT^{-3} of PT and PZ is at 17 and 13 K, while that of PMN and PMT is at 10 K in spite of their different composition, and that of SiO_2 glass is also found at 10 K, which is considered to be caused by the Boson peak [59]. Like this, it is obviously demonstrated from the low temperature heat capacity that in PMN, there are some additional low energy excitations not existing in the normal perovskite (anti)ferroelectrics, and the same situation can be assumed for PMT.

In order to obtain the information about the specific lattice vibrational states leading to the anomalous large heat capacity of PMN and PMT relaxors, the distribution of the density of vibrational states in a low frequency region was estimated using a combination of simple models for the lattice vibration, i.e., Debye and Einstein models. Debye formula was used for the contribution of the acoustic phonons with $3N$ degrees of freedom, and the characteristic temperature was fixed to be 230 K for PMN, which was estimated from elastic data. On the other hand, for PMT, the same value of Debye temperature was used because no elastic data was available. However, as seen in Table 4.1, it is very interesting that all of PMN, PT, and PZ have nearly the same elastic Debye temperature, and ${}^{3N}\Theta_D$ of 220 ~ 230 K may be common to lead-based perovskites. However, the heat capacity value at 2 K is about four times greater than that calculated from Debye formula with ${}^{3N}\Theta_D = 230$ K, which indicates the existence of glasslike low energy excitations in PMN and PMT. In order to describe the contribution of these glasslike low energy excitations, additional density of states were given to the lowest frequency region. The estimation was performed by nonlinear least-square fitting to the heat capacity data below 30 K with a combination of single Debye formula and Einstein formulae, where the characteristic temperatures and the degrees of freedom of Einstein formulae were the fitting parameters. Finally, it was found that the maximum in C_pT^{-3} of PMN and PMT were well described by three Einstein formulae. The results of the fittings to the heat capacity and the obtained distribution of the density of states in the low frequency region below 5 THz are shown in Fig.4.13 and Fig.4.14, respectively. Both of PMN and PMT have lattice vibrational

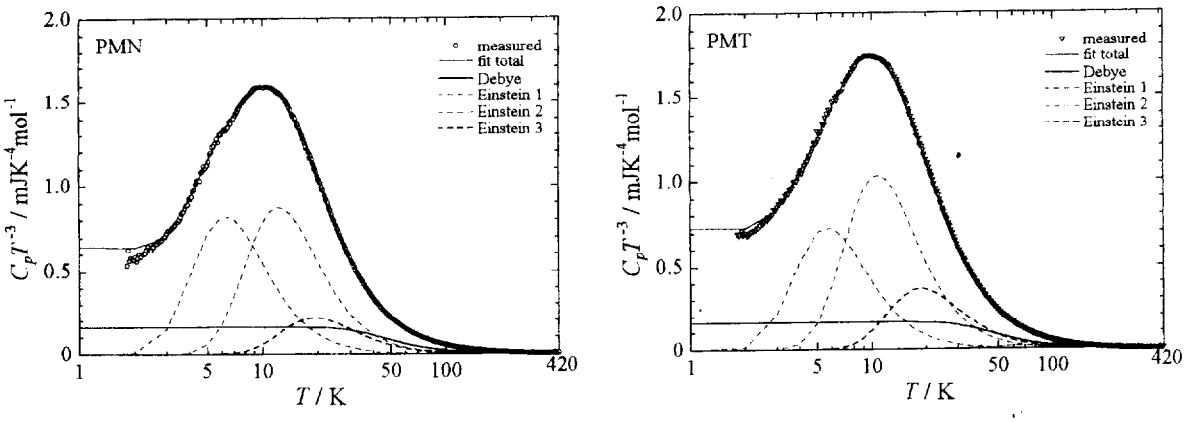

Fig. 4.13. Results of the fitting to the low temperature heat capacity data of PMN and PMT below 30 K using Debye and Einstein models for the lattice vibrations. Both show very large heat capacity value at 2 K, where the heat capacity values are about four times larger than that of Debye model (thick solid line) whose characteristic temperature was estimated from the measured values of elastic coefficient data. In order to compensate this large heat capacity in model calculations, additional density of states was given to the lowest frequency region.

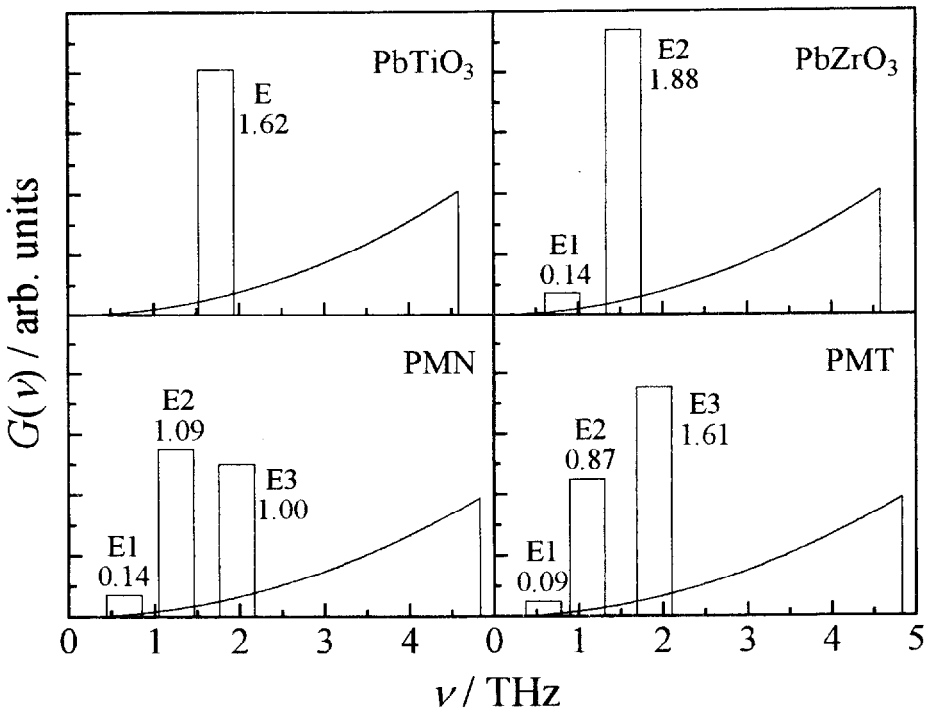

Fig. 4.14. Distribution of the lattice vibrational density of states obtained by model fitting to the low temperature heat capacity.

states (E3) around 2 THz, similar to PT (E) and PZ (E2). On the other hand, additional vibrational states (E2) exist around 1.5 THz in PMN and PMT, which do not exist in PT and PZ. In addition, there are the other additional states (E1) below 1 THz, similar to PZ (E1). To sum up, the E3 states around 2 THz can be considered as low frequency optical phonons commonly observed in the lead-based perovskite, which cause the Schottky anomaly-like heat capacity difference from BT shown in Fig.4.10(a). The E2 states around 1.5 THz are "anomalous" low frequency optical phonons, which are clearly the main constituents of the maximum in C_pT^{-3} at 10 K similar to the Boson peak in glasses. The E1 states below 1 THz have little contribution but are indispensable to describe the heat capacity in the lowest temperature region similar to E1 states in PZ. As interpreted in *Chapter 3*, these may be also anomalous low frequency optical phonons or non-phonon contribution related to dipolar interaction between antiparallel (PZ) or randomly oriented (PMN and PMT) local polarizations: such low energy excitations are not observed in normal ferroelectric BT and PT with a macroscopic spontaneous polarization within ferroelectric domains. In addition, there are glasslike low energy excitations leading to the T-linear term in the heat capacity. Like this, in PMN and PMT relaxors, there are various low energy excitations not observed in the normal perovskite (anti)ferroelectrics. What is the origin of such anomalous low energy excitations in the relaxors? It is not so easy to answer this question, but it can be said that the relaxors have two kinds of topological disorder, i.e., the two-phase coexistence of ferroelectric nanoregions and a paraelectric matrix and the partially ordered B-site cation arrangement, in spite of undoubted crystalline solids, and these topological disorder might be cause various low energy excitations mentioned above. If the thermodynamically most stable state of PMN and PMT is the ferroelectric state with completely ordered B-site cation arrangement, which might not be of relaxors any longer, the actual state of PMN and PMT should be a thermodynamically nonequilibrium frozen state, i.e., glassy state. Thus, it is not so strange to observe glasslike low energy excitations in the relaxors. To be more exact, the features considered as the characteristics of glasses may not be of glasses but of a system with some kind of disorder. However, the specific mechanisms have been still open question how the disorder causes low energy excitations, although the two-level excitation can be considered as a possible mechanism.

Recently, Gvasaliya *et al.* **[62]** analyzed the low temperature heat capacity data of PMN below 30 K obtained in the present study with the fractal formalism, which leads to the excitation of the fracton, and discussed the result of the analysis together with that of inelastic neutron scattering experiments **[57,58]**. The fracton is one of the elementary excitations and originally introduced to explain vibrational dynamics in the system with fractal structure, e.g., aerogels, polymers, and so on **[63,64]**. Thus, it can be reflected in the density of vibrational states although it is different from the phonon. They considered that the topology of the fractal

structure in PMN with the 1:1 ordered nanodomains affects the lattice dynamics and consequently the heat capacity. The density of vibrational states $G(\nu)$ of the fractons is characterized by the spectral dimension $\tilde{d}$ as

$$G(\nu) \propto \nu^{\tilde{d}-1}, \tag{4.2}$$

while that of the acoustic phonons is proportional to ν^2 :

$$G(\nu) \propto \nu^2. \tag{4.3}$$

The change in the lattice dynamics due to the difference in the structural features on various scales is characterized by the existence of a certain frequency of the crossover ν_{co} from the acoustic phonon to fracton regimes: at frequencies $\nu \geq \nu_{co}$, the density of vibrational states is described by Eq.(4.2), while at frequencies $\nu \leq \nu_{co}$, it is described by Eq.(4.3). Thus, the heat capacity is represented as

$$C_\nu = 3nR\left(\frac{T}{\Theta_D}\right)^3 \int_0^{\Theta_{co}/T} \frac{x^4 e^x}{(e^x-1)^2} dx + AT^{\tilde{d}-1} \int_{\Theta_{co}/T}^{\Theta_m/T} \frac{x^{\tilde{d}-1} e^x}{(e^x-1)^2} dx, \tag{4.4}$$

where Θ_{co} (= $h\nu_{co}/k$) is the characteristic temperature of the crossover and Θ_m (= $h\nu_m/k$) is the maximum characteristic temperature at which the fracton regime is implemented. The first and second terms of the right side of Eq.(4.4) are Debye formula and the formula for fractons, respectively. It has been found that the heat capacity of PMN below 30 K could be described by Eq.(4.4) and the obtained values of the fitting parameters, $\tilde{d}$, ν_{co}, and ν_m are in good agreement with those estimated from inelastic neutron experiments **[57,58]**. There is no difference between two fitting schemes with Einstein models and with the fracton model in the basic concept that there are anomalous lattice vibrational states in PMN. However, with Einstein model, it is possible to say there are anomalous lattice vibrational states but impossible to refer to their origin because Einstein model is a general one for the phonon, which is universal for solids. On the other hand, the fracton model is a specific one for special excitation in the system with topological disorder, and it seems to be superior in respect of referability to the origin: some topological disorder can cause the anomalous lattice vibrational states, i.e., fractons in PMN.

Taking the discussion up to this point into account, such anomalous large heat capacity might be caused by the complex nature on the *B*-site sublattice. Thus, it seems to be significant to compare PMN and PMT with another complex perovskite that is not relaxor. In this study, $Ba(Mg_{1/3}Ta_{2/3})O_3$ (BMT) was selected as such a complex perovskite. BMT is a member of the barium-based complex perovskites, which are attracted attention as materials with the low dielectric loss tangent for the microwave region **[65,66]**. The dielectric constant and the heat capacity of PMN, PMT, and BMT are shown in Figs.4.15 and 4.16, respectively.

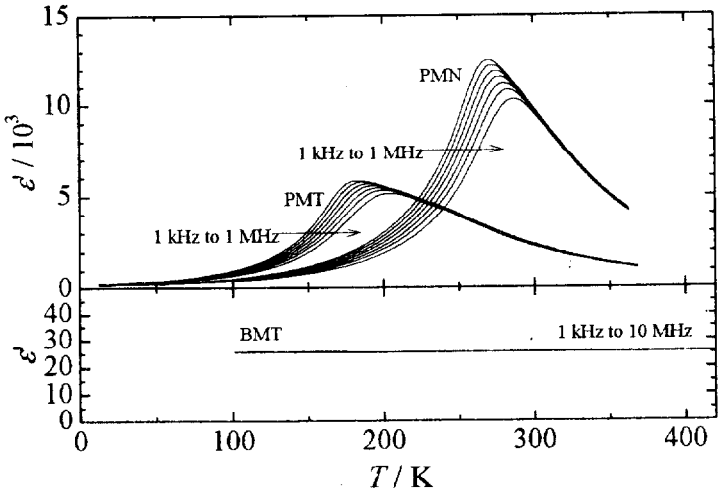

Fig. 4.15. Dielectric constant of PMN, PMT, and BMT. PMN and PMT show a large broad peak of the dielectric constant, while BMT shows almost temperature-independent value of 25.

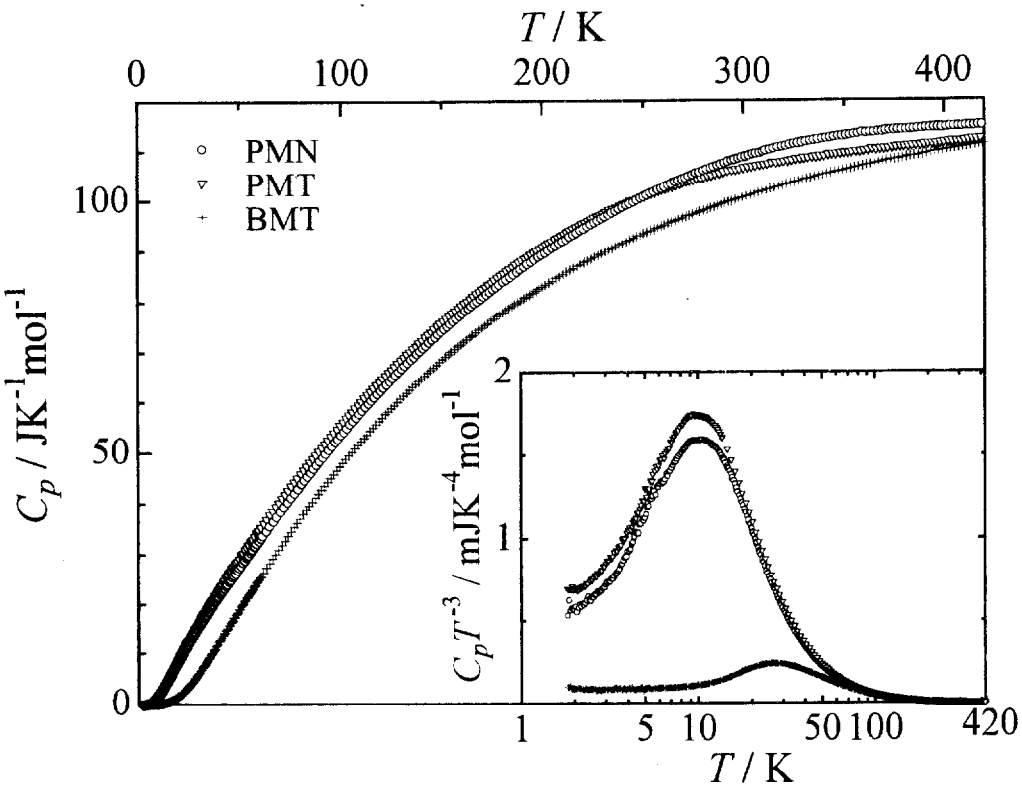

Fig. 4.16. Comparison of the heat capacity between relaxor PMN, PMT and nonrelaxor BMT. The heat capacity of BMT shows normal temperature-dependence typical of metal oxides.

The dielectric constant of PMN and PMT shows a broad peak with a large value of 10^3 ~10^4 around 300 and 200 K, respectively, while that of BMT shows a nearly temperature-independent value of 25, which agrees with the value reported previously for a ceramic sample **[65]**. On the other hand, the heat capacity of BMT is smaller than that of PMN and PMT relaxors over the whole measurement temperature range, although its value approaches that of the relaxors with increasing temperature and shows nearly the same value as PMT at 420 K. Especially, in a low temperature region, the difference between BMT and the relaxors is very large, and the heat capacity values of BMT are rather closer to that of BT than those of PMN and PMT. This obviously demonstrates that the anomalous large heat capacity of the relaxors is not caused by the complex nature on the *B*-site sublattice. However, there is a problem in this comparison. The sample of BMT used in this study is of hexagonal symmetry with the 1:2 ordered arrangement of Mg and Ta ($P\bar{3}m1$), while PMN and PMT are of cubic symmetry with macroscopically disordered arrangement of the *B*-site cations ($Pm\bar{3}m$). Thus the unit cell of BMT is a triple of the basic perovskite unit cell. It is expected that the tripling of the unit cell and the arrangement of the *B*-site cations affect the lattice vibrational states, and it is a little doubtful whether hexagonal BMT is a suitable subject for comparison with the relaxors. Actually, it has been reported **[67]** that it is possible to prepare BMT of cubic symmetry with disordered arrangement of Mg and Ta ($Pm\bar{3}m$), but unfortunately, cubic BMT could not be synthesized in this study in spite of following the same procedure as reported. In order to investigate the effect of the *B*-site cation ordering, it is necessary to perform the same measurement on cubic BMT. However, Gvasaliya *et al.* **[68]** has found from the results of inelastic neutron scattering experiments that the density of vibrational state of cubic BMT shows no anomalous feature as seen in PMN and PMT, and I believe that the anomalous large heat capacity is surely one of the singularities of the lead-based perovskite relaxors.

Heat Capacity Anomaly in a High Temperature Region

In the heat capacity difference from BT and PT (Fig.4.10), the shoulder-like difference was found around 300 K for PMN and around 200 K for PMT, which obviously indicates the existence of some heat capacity anomaly in a high temperature region. In addition, the temperature corresponds to that of the dielectric peak in each relaxor. This implies that the heat capacity anomaly is closely related to the mechanism causing the unique dielectric response in the relaxors. However, it is difficult to argue the existence of a heat capacity anomaly by comparison with other substances alone, and the feature of a substance should be characterized in itself. In some cases, a small or broad anomaly in the heat capacity can be seen more clearly in the corresponding Debye temperature, which is calculated from measured heat capacity using Debye formula. As illustrated by the phase transitions in BT, when there is

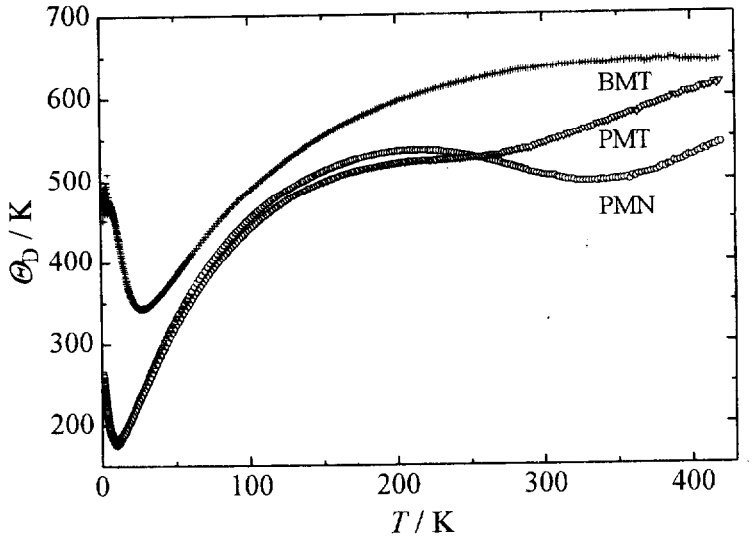

Fig. 4.17. Debye temperature calculated form the measured heat capacity of PMN and PMT assuming $15N$ degrees of freedom, where that of BMT is also shown for comparison. The Debye temperature curves of PMN and PMT obviously show a downward convex feature with a minimum at about 320 and 250 K, respectively, which clearly demonstrates the existence of a heat capacity anomaly over a very wide temperature range.

a heat capacity anomaly, the corresponding anomaly in the Debye temperature curve indicates a downward convex feature. Fig.4.17 shows the Debye temperatures of PMN and PMT calculated assuming $15N$ degrees of freedom, where that of BMT is also shown for comparison. A deep hollow in PMN and PMT around 10 K is due to the contribution of the low frequency optical phonons and the additional low energy excitations discussed above, and such a hollow is commonly observed in a variety of substances, as also seen in BMT (the same figure), BT, PT, and PZ (Fig.3.14). On the other hand, in the higher temperature region, another broad hollow is clearly seen with a minimum at about 250 K for PMT and 320 K for PMN. With increasing temperature, the Debye temperature usually approaches a constant value as the heat capacity saturates to a classical value, or gradually decreases as an anharmonic effect in the lattice vibrations becomes stronger. In either case, the Debye temperature never increases after showing a tendency to be constant or decrease. However, in PMN and PMT, the Debye temperature clearly increases after showing a tendency to be constant (around 200 K in PMT) or decrease (around 300K in PMN). As a result, a broad hollow is formed, but a hollow in such a high temperature region is quite unusual and no such an anomalous curve is found in related compounds, e.g., BMT. A downward convex feature in the Debye temperature curve

corresponds to an upward convex feature in the heat capacity curve. Therefore, the present results clearly demonstrate the existence of a heat capacity anomaly in such a high temperature region for PMN and PMT.

In dielectrics, the heat capacity consists of the lattice contribution C_{lat}, when there is no anomaly. Thus, in order to obtain the excess heat capacity ΔC_p (= $C_p - C_{lat}$) due to an anomaly, an invisible lattice contribution in the region of the anomaly must be estimated. In many cases, however, it is not so easy to estimate an invisible contribution, and the estimation inevitably involves somewhat arbitrariness depending on the philosophy of a researcher. Therefore, the estimation should be performed on firm grounds according to circumstances. Taking priority of an experimental result into account, theoretical calculation based on a simplified model does not always provide an appropriate estimation. When the lower and upper end temperatures of an anomaly, T_{low} and T_{up}, are clearly found, the data below T_{low} and above T_{up} can be usually considered as pure lattice contribution. In a first-order phase transition, a clear jump is often observed between the data below T_{low} and above T_{up}. In this case, different base lines are assumed for the data in each region, and an invisible lattice contribution can be estimated by extrapolating these base lines to the phase transition point (Fig.4.18(a)). On the other hand, when no jump is observed, it can be estimated by connecting smoothly the data below T_{low} and above T_{up} with a single base line (Fig.4.18(b)). However, in the case that an anomaly shows a very long tail, it is difficult to find out T_{low} and/or T_{up}. Especially, in PMN and PMT, the anomaly is distributed over a very wide temperature range, and it is almost impossible to find out T_{low} and T_{up}. In such cases, it is effective to employ some theoretical models. Thus, a

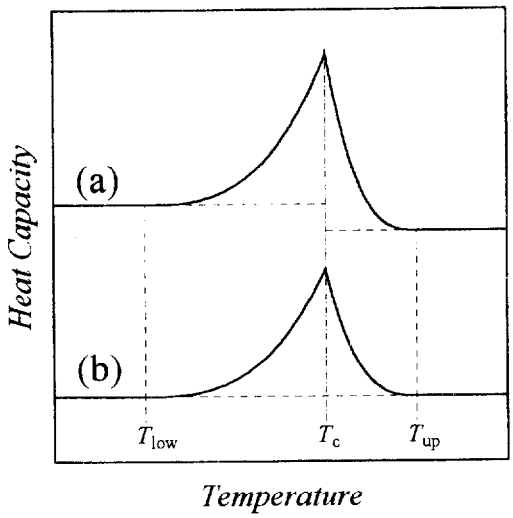

Fig. 4.18. Example of the estimation of an invisible lattice contribution in the phase transition region: (a) in the case with a jump between the lattice contribution between high and low temperature sides of an anomaly, and (b) without any jump. Actually, it is not as simple and easy as this example.

simple model for the lattice vibrations, i.e., a combination of Debye, Einstein, and modified Einstein models, was employed for the estimation. It has been already mentioned above that the heat capacity data below 50 K could be well described by the combination of a single Debye and three Einstein models, which were employed for the low frequency region below 5 THz. In addition to them, two modified Einstein models were employed for the higher frequency region above 5 THz. The estimation was performed by nonlinear least square fitting to the heat capacity data that can be considered as pure lattice contribution, where the temperature regions of the data used for the fitting were also adjusted by trial-and error. If the temperature region of the data used for the fitting is widen on the low temperature side of the anomaly, those data can be well described by clumping the density of states at lower frequencies, but the clump of the density of states at lower frequencies gives rise to excess of calculated values over measured ones on the high temperature side, and such a result is clearly overestimated. Therefore, both temperature region and fitting parameters were adjusted until a valid result was obtained. For PMT, the heat capacity data below 50 K and above 400 K were used for the

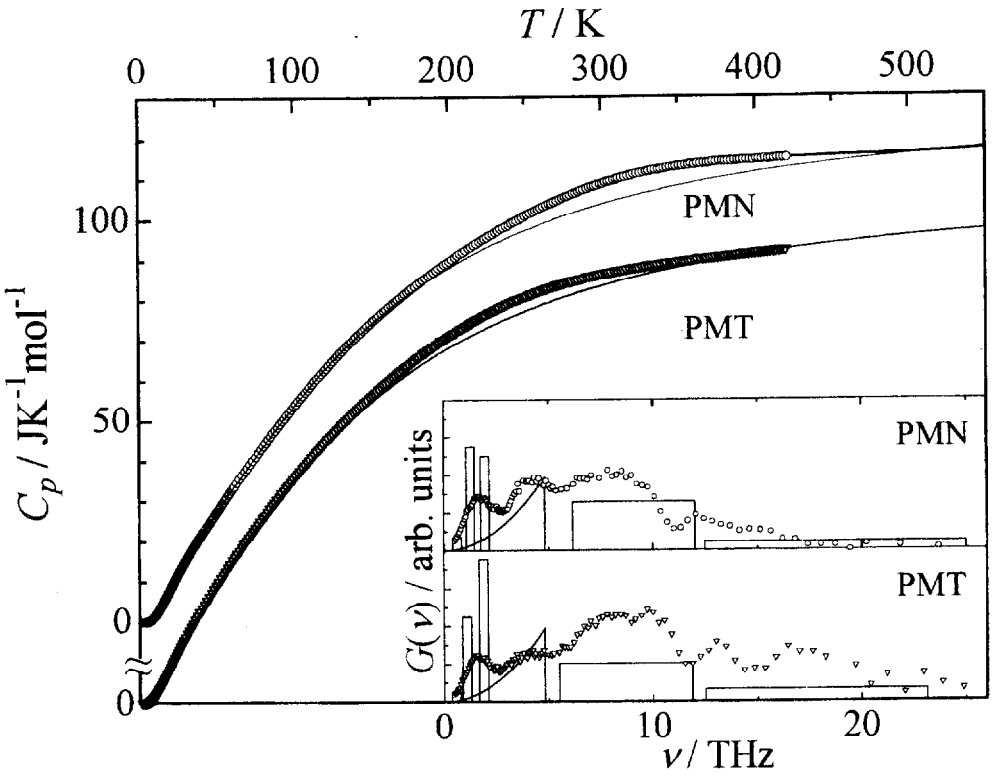

Fig. 4.19. Estimated lattice contribution (solid line) of PMN and PMT. Assuming this base line, the anomaly is clearly seen in the raw data of the heat capacity. For PMN, the heat capacity above 420 K was smoothly extrapolated using the data below 420 K. The inset shows the distribution of the density of lattice vibrational states obtained in the estimation, where that obtained from the results of inelastic neutron scattering experiments is shown for comparison. Both are in good agreement, which indicates the validity of the present estimation.

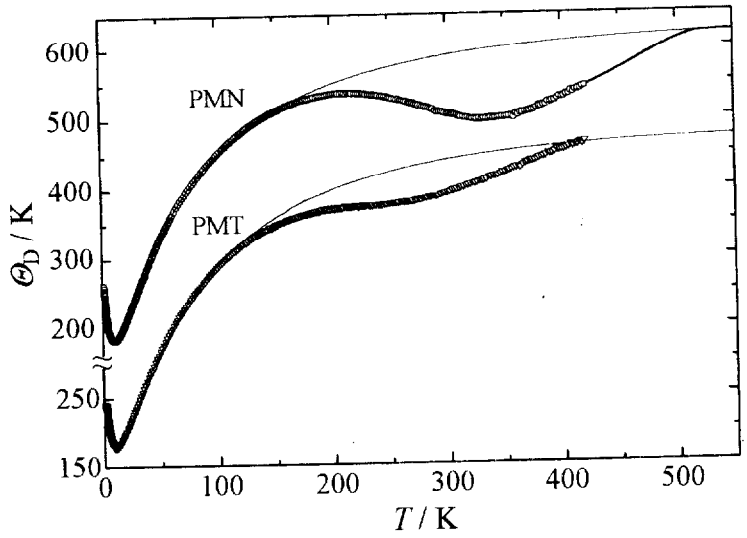

Fig. 4.20. Debye temperature of the estimated lattice contribution with that of the experimental one. In the category of the models assuming harmonic oscillation or vibration, the heat capacity definitely saturates to the classical value and the corresponding Debye temperature approaches a constant value. Thus, such base line makes the anomalous curve conspicuous.

fitting. On the other hand, in PMN, the heat capacity data in the high temperature region obviously include the extra contribution and could not be used for the fitting. Thus the estimated lattice contribution for PMT at high enough temperatures was considered as the high temperature heat capacity of PMN, as both compounds were expected to show the same heat capacity value at high temperatures. Consequently, only the data below 120 K was used for the fitting. The estimated lattice contributions and the corresponding Debye temperatures for PMN and PMT are shown as thin solid lines together with the experimental ones in Figs.4.19 and 4.20, respectively, where the heat capacity of PMN is smoothly extrapolated above 420 K as shown with a thick solid line. In the inset of Fig.4.19, the obtained distribution of the density of vibrational states is shown together with that obtained by inelastic neutron scattering experiments **[57,58,68]**. Both results are in good agreement with each other, and this agreement clearly indicates the validity of the employed model and the estimated lattice contribution. Actually, however, these lattice contributions seem to be a little overestimated, because even in PMT, the Debye temperature still shows a tendency to increase at 420 K as seen in Fig.4.19: if there is not the anomaly, the Debye temperature should be constant or decrease at such high temperatures. Nevertheless, I believe that the present results are the best at this stage. The converged values of the fitting parameters are tabulated in Table 4.2.

compound	model	characteristic frequency ν / THz (characteristic temperature Θ / K)	degrees of freedom / N
PMN	Glasslike	–	–
	Debye	4.79 (230) (fixed)	3.00 (fixed)
	Einstein 1	0.65 (31)	0.14
	Einstein 2	1.26 (60)	1.09
	Einstein 3	1.97 (94)	1.03
	modified Einstein 1	6.04 – 12.02 (296 – 577)	7.16
	modified Einstein 2	12.50 – 25.00 (600 –1200)	2.58
PMT	Glasslike	–	–
	Debye	4.79 (230) (fixed)	3.00 (fixed)
	Einstein 1	0.58 (28)	0.09
	Einstein 2	1.10 (53)	0.87
	Einstein 3	1.93 (92)	1.61
	modified Einstein 1	5.50 – 11.88 (264 – 570)	6.24
	modified Einstein 2	12.50 – 23.13 (600 – 1110)	3.26

Table 4.2. Converged values of the fitting parameters obtained by the estimation of the lattice contribution in the region of the heat capacity anomaly. The estimation was performed by nonlinear least-square fitting to the measured heat capacity data below 50 K and above 400 K for PMT, and below 120 K for PMN, using Debye, Einstein, and modified Einstein models.

The excess heat capacity ΔC_p of PMN and PMT obtained by subtracting the estimated lattice contribution from the measured heat capacity is shown in Fig.4.21. Fig.4.21(a) shows the raw ΔC_p, and its integration is the excess enthalpy ΔH, the temperature-dependence of which is shown as a solid line for PMN and a broken line for PMT. The anomaly is distributed over the very wide temperature range between 150 and 500 K in PMN and between 50 and 400 K in PMT, and the maximum temperature is at 320 K in PMN and at 250 K in PMT. On the other hand, Fig.4.21(b) shows $\Delta C_p T^{-1}$, and its integration is the excess entropy ΔS, the temperature-dependence of which is also shown as a solid line for PMN and a broken line for PMT, where Rln8 is set as the standard as explained below. As seen from the areas of ΔC_p and $\Delta C_p T^{-1}$ in Fig.4.21, it is very interesting that PMN and PMT show different values of ΔH but nearly the same value of ΔS, which seems to reflect some mechanism common to both relaxors. The values of the excess enthalpy and entropy are tabulated in Table 4.3.

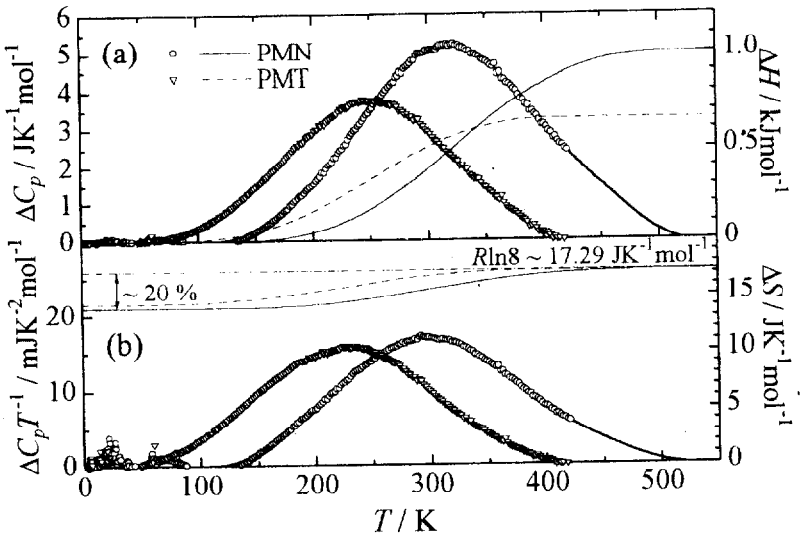

Fig. 4.21. Excess heat capacity ΔC_p obtained by subtracting the estimated lattice contribution from the measured heat capacity: (a) raw ΔC_p and the excess enthalpy ΔH, which is the integral of ΔC_p, and (b) ΔC_pT^{-1} and the excess entropy ΔS, which is the integral of ΔC_pT^{-1}.

Compound	temperature range ΔT / K	excess enthalpy ΔH / kJK^{-1}	excess entropy ΔS / JK^{-1}mol^{-1}
PMN	150 – 500	1.00	3.3
PMT	50 – 400	0.65	2.9

Table 4.3. Thermodynamic quantities related to the heat capacity anomaly of PMN and PMT.

The excess heat capacity is shown together with the complex dielectric constant in Fig.4.22. The heat capacity anomaly obviously corresponds to that of the dielectric constant, although the maximum temperature is a little different: the maximum in the dielectric constant strongly depends on the measurement frequency. However, this heat capacity anomaly obviously originates in the mechanism causing the characteristic dielectric response.

The first evidence for the nucleation of ferroelectric regions in PMN was provided as the deviation in the index of refraction from the linear temperature dependence starting around 600 K with decreasing temperature **[6]**. Later structural studies revealed **[5-8]** that the ferroelectric regions grow gradually with decreasing temperature but the growth ceases around 150 K. Consequently, these can not become macroscopic ferroelectric domains but ferroelectric nanoregions (FNR) with a size of a few 10 nm, and most of the crystal remains a cubic paraelectric phase down to liquid helium temperature. Thus two phases coexist below 600 K,

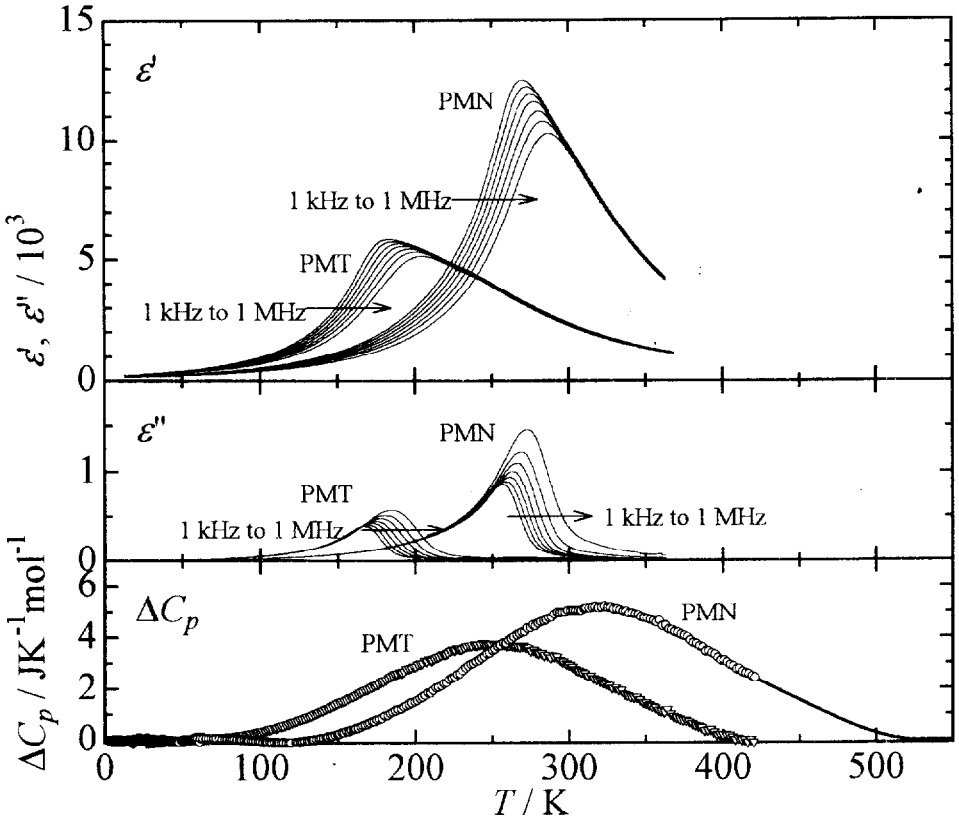

Fig. 4.22. Excess heat capacity and complex dielectric constant of PMN and PMT. It is obviously seen in this figure that the heat capacity anomaly corresponds to the peak of the dielectric constant in each relaxor.

and the phase transition as a macroscopic cooperative phenomenon does not occur after all. On the other hand, the heat capacity anomaly of PMN is found between 150 and 500 K, which coincides with the temperature region of the nucleation and the growth of FNR. The anomaly is thus likely to be caused by the formation of FNR. On the analogy of the temperature region of the anomaly, the same phenomenon should take place in PMT between 50 and 400 K. Taking account of the major premise that two phases can coexist only at a first-order phase transition point, the assertion of "domain state model" seems to be valid that "PMN is ferroelectric by nature but its phase transition is smeared", because the heat capacity anomaly of PMN and PMT forms a very broad peak and the phase transition seems to be "smeared" or "diffused" as compared with a normal first-order phase transition, where a very sharp heat capacity anomaly is usually observed. In other words, the phase transition is restricted to nanoscale, and the domain state is realized in the relaxors. In this sense, the concept of the diffuse phase transition proposed by Smolenskii [2,3] is not altogether inadequate for the description of the relaxors, but the phase transition as a macroscopic cooperative phenomenon

does not take place. The basic mechanism of the phase transition is reflected in the value of the transition entropy ΔS_{trs}, which is the excess entropy ΔS in the present case. The estimated value of ΔS for PMN and PMT is 3.3 and 2.9 $JK^{-1}mol^{-1}$, respectively, which suggests an order-disorder type of mechanism for the formation of FNR because the phase transition caused by a displacive mechanism should not have such a large value of ΔS. In the case of order-disorder phase transition, the expected value of ΔS between fully ordered and disordered states should be considered in detail, and accordingly the ordering of Pb ions at off-center positions **[5-8]** was presumed. In PMN, the polarizations of FNR resulting from the ordering of ionic shifts are randomly oriented along the eight equivalent $<111>_{cub}$ directions, and this means eight ionic positions for ordering **[69]**. Taking this into account, the expected value of ΔS is Rln8, and the experimental values are about 20 % of this value. On the other hand, the profile analyses of powder neutron diffraction peaks of PMN **[7,8]** revealed that the maximum volume ratio of FNR to the whole crystal is also about 20 %. In Fig.4.23, the temperature-dependence of the ratio of the entropy to Rln8 ($\Delta S/R$ln8) and the volume ratio of FNR to the whole crystal (V_{FNR}/V) for PMN is shown, where both are in good agreement. According to this concept, the phase transition is not completed in the crystals of PMN and PMT, which should be in a glassy state at low temperature with residual entropy of $0.8R$ln8. However, the enumeration of entropy is not so simple because individual Pb ions must be ordered at one in eight possible positions at low temperatures in addition to the ordering as FNR. Hence more detailed calculation of the entropy is needed for the individual ionic ordering and their clustering. Fig. 4.23.

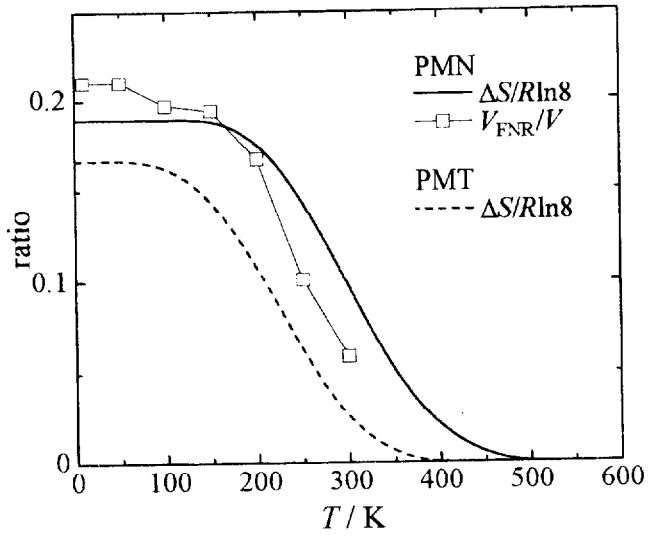

Fig. 4.23. Temperature-dependence of the ratio of the excess entropy to Rln8 ($\Delta S/R$ln8) of PMN and PMT, and the volume ratio of FNR to the whole crystal (V_{FNR}/V) of PMN obtained from the structural refinement by Uesu *et al.* **[8]**.

Some researchers believe a displacive type of mechanism for the formation of FNR because of the soft-mode theory that has been developed on the perovskite ferroelectrics [70], but this is not approved any longer in view of the value of ΔS. The order-disorder type of description concerning the Pb shifts is also supported by recent studies on the local structure of PMN employing synchrotron radiation X-ray diffraction for a single crystal sample [71] and TEM observation [72]. However, the situation over the local structural change in PMN is becoming more complicated because antiferroelectric ordering besides ferroelectric ordering is deduced for the Pb shifts [71,72], which is induced by antiphase tilting of the oxygen octahedra [72]. Unfortunately, it is quite difficult to extract selectively each contribution of these structural changes from the heat capacity, but it is undoubted that some changes leading to the large heat capacity anomaly occur around the dielectric peak temperature.

Thermodynamic Consideration on the Orientational Glasslike Nature

Although the large value of ΔS can be explained to some extent assuming an order-disorder type of mechanism for the formation of FNR, the dipolar interactions between the local polarizations of FNR should be also considered in detail, because the dipolar interactions may have some contribution to the excess heat capacity. As explained in the introduction of this chapter, in the dipolar glass model proposed by Viehland *et al.* [30-32], the dielectric relaxation process of PMN in the middle frequency range can be well described by the Vogel-Fulcher (V-F) law and the freezing temperature T_f is found to be ~ 220 K (Fig.4.3). The V-F equation is represented by

$$f = f_0 \exp\left(-\frac{E_a}{k(T - T_f)}\right). \tag{4.5}$$

Tentatively, the V-F fitting was also attempted for the present results of the dielectric constant measurements in the middle frequency range for PMN and PMT, and a similar fitting result was obtained for PMN as shown in Fig.4.24. This result suggests the strong dipolar interactions between FNR. On the other hand, if there are strong dipolar interactions between FNR, thermal hysteresis and/or anomalous thermal relaxation phenomena caused by the re-orientational relaxation of dipoles are also observed by adiabatic calorimetry around an apparent freezing temperature where the relaxation time becomes comparable to a measurement time scale [73,74]. According to the dipolar glass model [30-32], such a phenomenon should be observed around an apparent freezing temperature, i.e., 240 K for PMN and 150 K for PMT in adiabatic calorimetry because the heat input corresponds to about 10^{-3} Hz (see $1/T_{max}$ at 10^{-3} Hz in Fig.4.24). However, no hysteresis or anomalous relaxation was observed during all the heat capacity measurements. This result may indicate that the dipolar interactions are not so strong in PMN and PMT. In this case, the relaxation process should rather obey the Arrhenius law:

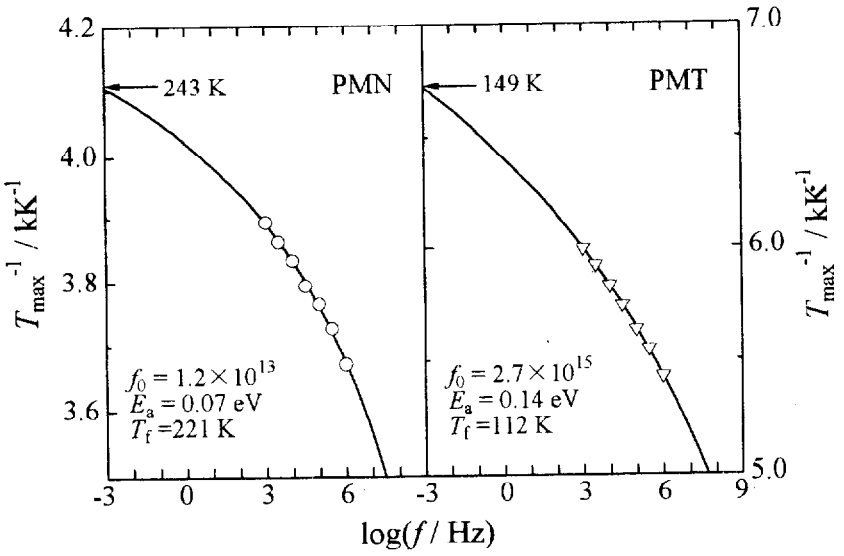

Fig. 4.24. Results of the Vogel-Fucher fitting to the present data, where T_{max} is the maximum temperature of the dielectric loss. The obtained values of the fitting parameters are in the figure, which are almost the same as the result of Viehland *et al.* **[30-32]** for PMN. The temperature pointed by an arrow corresponds to the apparent freezing temperature at 10^{-3} Hz, which corresponds to the frequency of heat input in a usual heat capacity measurement by an adiabatic method. Thus, it is expected that the characteristic phenomena of glasses are observed around this temperature in adiabatic calorimetry.

$$f = f_0 \exp\left(-\frac{E_a}{kT}\right). \tag{4.6}$$

As seen in the equations, the difference between the V-F law and the Arrhenius law is whether the system has a finite freezing temperature. In the case that interacting dipoles freeze cooperatively, the relaxation process obeys the V-F law showing critical slowing down, while in the case that each dipole behaves independently, the relaxation process is of a simple thermal activation type obeying the Arrhenius law.

On the other hand, it is known that E_a is proportional to the individual size of polar regions **[28]**, which are FNR in relaxors **[27]**. Comparing Eq.(4.5) with Eq.(4.6), the V-F law can be regarded as a modified Arrhenius law with temperature-dependent activation energy in the manner of $T/(T - T_f)$, which diverges at T_f. Therefore the V-F law seems to be valid but may not be essential if E_a converges on a finite value. In other wards, taking account of the increase of E_a due to the increase of the size of FNR, the relaxation process appears to obey the V-F law even if taking no account of growing the dipolar interactions.

Since the averaged size of FNR shows the similar temperature-dependence to V_{FNR}/V **[13,71]**, it can be also assumed for E_a. Assuming a solid line in Fig.4.25 for the temperature-

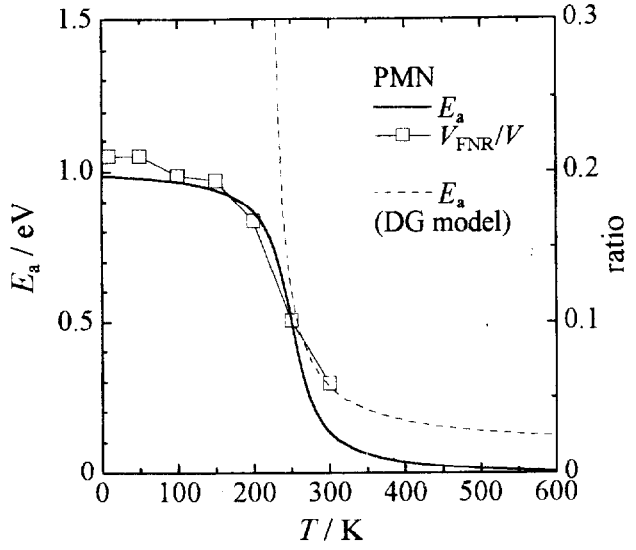

Fig. 4.25. Temperature-dependence of the activation energy E_a for PMN (solid line) assumed from the temperature-dependence of the averaged size of FNR **[13,71]**, the volume ratio of FNR **[8]**, and the ratio of the excess entropy to Rln8. For comparison, the temperature-dependence of E_a in the dipolar glass (DG) model **[30-32]** (broken line) is shown together.

dependence of E_a, where E_a of dipolar glass model is also shown as a broken line for comparison, the relationship between frequency f and the maximum temperature of the dielectric loss T_{max} for PMN was numerically calculated using Eq.(4.6). Although this is analogous to the idea proposed by Lu and Calvarin **[29]**, this model does not take into account the distribution of E_a due to the size distribution of FNR, but the change of E_a due to the change of the averaged size of FNR. The result of the calculation is shown in Fig.4.26 with the experimental data, where the data below 100 Hz were reported by Colla *et al.* **[33]**. It is found that the relaxation process of PMN can be well described by the modified Arrhenius law with pre-exponential factor $f_0 \sim 10^{11}$ Hz and temperature-dependent E_a changing from 0 eV at the high temperature limit (above 600 K) to 1 eV at the low temperature limit (below 150 K)(Fig.4.23), and these values of f_0 and E_a are also physically acceptable. In this model, the relaxation process does not show critical but continuous slowing down. Namely, it seems to be consistent with the idea of two relaxation processes, i.e., α- and β-relaxation processes proposed by Christen *et al.* **[34]**, and the takeover temperature region of these two relaxation processes just corresponds to that of the inflection point in E_a, where the relaxation process seem to be well described by the Arrhenius law (broken line in Fig.4.25), which leads to unphysical values of f_0 and E_a **[33]**. In higher and lower frequency region, a deviation from this seeming

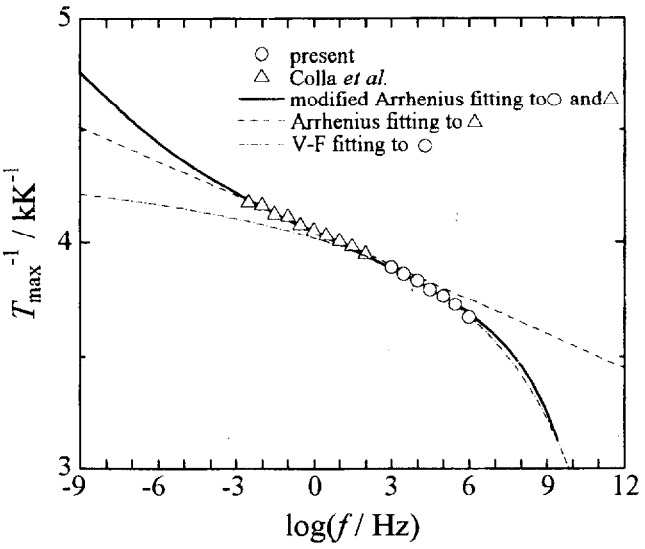

Fig. 4.26. Result of the calculation of the relaxation process in PMN with the Arrhenius equation assuming the solid line in Fig.4.25 for the temperature-dependence of the activation energy (solid line). The relaxation process of PMN can be well described by this model, where the data below 100 Hz are reported by Colla *et al.* **[33]**. The dashed dotted line represents the V-F fitting to the present data, while the broken line represents the simple Arrhenius fitting to the data reported by Colla *et al.*, which leads to the unphysical values f or both f_0 and E_a. The result from the present model is in good agreement with that from the V-F fitting in a high frequency and temperature region, but in a low frequency and temperature region, it starts to deviate from both V-F and Arrhenius fitting results, which indicates seeming two relaxation process similar to the phenomenological model reported by Christen *et al.* **[34]**. Namely, from this model it is expected to observe continuous slowing down over critical slowing down.

Arrhenius law is observed, which means two different relaxation processes with different values of E_a. This result suggests that the relaxor state of PMN in zero bias field is not the glassy state with the cooperative freezing of FNR but the domain state with FNR behaving independently, and it is considered that the actually observed phenomenon is not the signature of the freezing at a finite temperature but the blocking of the local polarizations of FNR in the domain state. In order to verify the present model, it might be necessary to perform the dielectric spectroscopy at very low frequencies below 10^{-3} Hz and detect the deviation from the seeming Arrhenius behavior in a low frequency region, but it seems to be quite difficult due to the transcendency of the time-scale of a phenomenon to the experimental time-scale.

This is a one possible interpretation for the orientational glasslike nature of the relaxors, and this is not a definitive result of this problem, because the cooperative freezing phenomenon is not always detected in the heat capacity measurements. Namely, it is possible that the thermodynamic signature of cooperative freezing is not detected if its energetic contribution is quite smaller than the total energy of the system. On the other hand, recent results of the nonlinear dielectric spectroscopy on PMN have been shown the signature of the cooperative freezing of FNR. In these measurements, however, the problem of a blocking phenomenon is inevitable because of the essential dynamic nature of the measurement. Thus, it is indispensable to estimate theoretically the energetic contribution of the freezing phenomenon if believing it actually takes place. However, it seems that the models persisting the orientational glasslike freezing have not considered this point. From the present results of the heat capacity measurements, it is at least clarified that the energetic contribution of the dipolar interactions between the local polarizations of FNR is too small to be detected in the heat capacity even if the strong correlation exists between FNR. For further understanding the orientational glasslike nature of relaxors, quantitative theoretical consideration taking the energetic contribution of the dipolar interactions into account is highly desired.

Finally, if the present or the V-F like description of the dielectric relaxation process in a high frequency region is valid (Fig.4.26), the maximum temperature of the heat capacity anomaly, i.e., 320 K for PMN and 250 K for PMT, corresponds to that of the complex dielectric constant in GHz region, where the frequencies changes from that of the lattice vibration to of relaxation. This might indicate two possibilities: the heat capacity anomaly reflects the thermal fluctuation of FNR either directly or indirectly, i.e., through the growth of FNR. Although the latter possibility is suggested in the discussions above, it is not clearly pointed out in the present study, because the heat capacity anomaly has just observed in the relaxors.

4.1. Conclusion

In this chapter, the results of the heat capacity measurements on typical relaxors $Pb(Mg_{1/3}Nb_{2/3})O_3$ (PMN) and $Pb(Mg_{1/3}Ta_{2/3})O_3$ (PMT) are considered and discussed in detail. Compared with the normal perovskite (anti)ferroelectrics, $BaTiO_3$ (BT), $PbTiO_3$ (PT), and $PbZrO_3$ (PZ), two remarkable singularities are found in the heat capacity of the relaxors, i.e., the anomalous large heat capacity in the low temperature region below 30 K and the existence of a heat capacity anomaly in a higher temperature region. The anomalous large low temperature heat capacity of the relaxors implies the existence of additional low energy excitations that are not observed in the normal perovskite (anti)ferroelectrics. There are two or three types of

these low energy excitations: the quantum mechanical two-level-like excitation leading to a T-linear term in the heat capacity and the excitations of Boson peak-like anomalous vibrational states, which have been considered as the characteristics of structural glasses. In addition, another low energy excitation characterized by the vibrational states below 1 THz obtained by fitting to the heat capacity data using simple models for the lattice vibration are found in the relaxors, while interestingly, it is also found in the antiferroelectric PZ. In PZ, the local polarizations due to shifts of Pb ions are arranged in anti-parallel manner, while those in the relaxors are randomly oriented along eight equivalent $<111>_{cub}$ directions. Thus, these additional low energy excitations might be caused by anti-paralleled or randomly oriented local polarizations because these are not found in BT and PT where a spontaneous polarization is formed within macroscopic ferroelectric domains, or anomalous low frequency optical phonons related to the structural feature in each kind of compounds. The existence of these low energy excitations clearly indicates some glasslike disorder in the relaxors in spite of their complete crystallization. Taking it into account, the heat capacity of PMN measured in the present study was analyzed by Gvasaliya *et al.* using a fractal description with respect to some topological disorder, which might originates from the partially ordered arrangement of the B-site cations or hetero-structure composed of ferroelectric nanoregions (FNR) formed in the paraelectric matrix, and it was found that the measured data below 30 K are well described by this model, where involved fitting parameters show a good agreement with those expected from inelastic neutron scattering experiments. On the other hand, this anomalous large heat capacity might be originate from the complex nature on the B-site sublattice. In order to check this possibility, nonrelaxor complex perovskite $Ba(Mg_{1/3}Ta_{2/3})O_3$ (BMT) was also investigated and confirmed that the anomalous large heat capacity is a characteristic of the relaxors.

In a higher temperature region, some heat capacity anomaly obviously exists in the relaxors as shown by the anomalous temperature-dependence of the Debye temperature calculated from the measured heat capacity. From the correspondence with the peak temperature region of the dielectric constant, this heat capacity anomaly has the same origin as the dielectric maximum, i.e., the formation of FNR. The anomaly was found in a very wide temperature region over a few hundred Kelvin, which coincides with the temperature region of the nucleation and the growth of FNR reported for PMN. The excess entropy ΔS estimated from the excess heat capacity ΔC_p, which is obtained by subtracting the estimated lattice contribution from the measured heat capacity, is about 3 $JK^{-1}mol^{-1}$ in both PMN and PMT, which suggests an order-disorder type of the formation mechanism of FNR, because such a large value of the entropy can not be explained by a displacive mechanism of phase transition. Assuming the ordering of the ionic shifts of Pb from the ideal crystallographic sites, which is expected to have eight possible positions along $<111>_{cub}$ direction, the expected value of ΔS

between the fully ordered and disordered states is Rln8, and the estimated value of ΔS is about 20 % of Rln8, which is consistent with the volume ratio of FNR to the whole crystal estimated by the structural refinements for PMN. Thus, the formation of FNR is considered due to the local ordering of the ionic shifts of Pb from a thermodynamic point of view.

From the structural and thermodynamic points of view, the formation of FNR seems to be characterized by a standstill of the growth of ferroelectric regions in a first-order ferroelectric phase transition process. Thus, the same situation can be assumed for the activation energy E_a for the thermal fluctuation of FNR with local polarizations, because it is known that E_a is proportional to the individual size of polar regions. Thus, taking it into account, the dielectric relaxation process was calculated using a modified Arrhenius low whose E_a increases with decreasing temperature but converged on a finite value below 150 K, and it was found that the actual relaxation process of PMN can be well described by this model without cooperative freezing of the polarizations of FNR at a finite temperature argued in the dipolar glass model. Totally, the present results seem to support the description of the ferroelectric nanodomain state rather than that of the orientational glass state.

Summarizing these results, the glasslike nature in PMN can be classified into two categories, i.e., structural glasslike nature and orientational glasslike nature, and these two glasslike natures should not be confused because the latter is considered as the secondary nature caused by the former and it might not result in a glassy state with cooperative freezing but a superparaelectric state. In addition, the former can be also classified into two categories, i.e., partial order of the ionic shifts of Pb, which lead to the formation of FNR in the paraelectric matrix, and partial order on the B-site cation arrangement or the existence of the random layer, which is considered to cause the former structural glasslike nature. However, it is quite difficult to estimate the residual entropy due to each category, because ΔS between the fully ordered and disordered states should be estimated, and some theoretical background is required. Especially concerning the B-site cation order, as far as the thermodynamic order-disorder phase transition can not be clearly observed in the PMN-family due to restriction of kinetics, it is impossible to determine the value of entropy experimentally. Thus, in order to investigate the effects of the B-site cation order, it seems to be effective to study the lead-based complex perovskites showing clear variation of the B-site cation ordering with suitable thermal treatments. I believe that every piece of information that can be extracted from the heat capacity of PMN and PMT has been already extracted in this study. However, what each piece of the information indicates has been clarified yet. Further studies, especially theoretical consideration, are required.

References

[1] G. A. Smolenskii and V. A. Isupov, *Sov. J. Tech. Phys.* **24**, 1375 (1957).

[2] G. A. Smolenskii, V. A. Isupov, A. I. Agranovskaya and S. N. Popov, *Sov. Phys. Solid State* **2**, 2584 (1961).

[3] G. A. Smolenskii, *J. Phys. Soc. Jpn.* (*Proc. 2nd Int. Meeting on Ferroelectricity*) **28**, S26 (1970); *Ferroelectrics* **53**, 129 (1984).

[4] G. Burns and F. H. Dacol, *Solid State Commun.* **48**, 853 (1983); *Phys. Rev.* **B28**, 2527 (1983); *Ferroelectrics* **104**, 25 (1990).

[5] P. Bonneau, P. Garnier, E. Husson and A. Morell, *Mater. Res. Bull.* **24**, 201 (1989).

[6] P. Bonneau, P. Garnier, G. Calvarin, E. Husson, J. Gavarri, A. W. Hewat, and A. Morell, *J. Solid State Chem.* **91**, 350 (1991).

[7] N. de Mathan, E. Husson, G. Calvarin, J. R. Gavarri, A. W. Hewat, and A. Morell, *J. Phys.: Condens. Matter* **3**, 8159 (1991).

[8] Y. Uesu, H. Tazawa, K. Fujishiro, and Y. Yamada, *J. Korean. Phys. Soc.* **29**, S703 (1996).

[9] K. Fujishiro, Y. Uesu, Y. Yamada, B. Dkhil, J. M. Kiat, and Y. Yamashita, *J. Korean. Phys. Soc.* **32**, S964 (1998).

[10] A. D. Hilton, C. A. Randoll, D. J. Barber, and T. R. Shrout, *Ferroelectrics* **93**, 379 (1989).

[11] A. D. Hilton, D. J. Barber, C. A. Randoll, and T. R. Shrout, *J. Mater. Sci.* **25**, 3461 (1990).

[12] L. A. Bursill, H. Qian, J. L. Peng, and X. D. Fan, *Physica* **B216**, 1 (1995).

[13] M. Yoshida, S. Mori, N. Yamamoto, Y. Uesu, and J. M. Kiat, *Ferroelectrics* **217**, 327 (1998); *J. Korean Phys. Soc.* **32**, S993 (1998).

[14] E. Husson, L. Abello, and A. Morell, *Mat. Res. Bull.* **23**, 357 (1988).

[15] J. Chen, H. M. Chan, and P. Harmer, *J. Am. Ceram. Soc.* **72**, 593 (1989).

[16] T. R. Schrout, W. Huebner, and C. A. Randall, *J. Mat. Sci.* **25**, 3461 (1990).

[17] C. Boulesteix, F. Varnier, A. Llebaria, and E. Husson, *J. Solid State Chem.* **108**, 141 (1994).

[18] R. E. Newnham, *NIST Spec. Publ. 804, Chem. of Electronic Ceram. Materials, Proc. Inter. Conf.* 39 (1991).

[19] V. Westphal, W. Kleemann, and M. D. Glinchuk, *Phys. Rev. Lett.* **68**, 847 (1992).

[20] N. de Mathan, E. Husson, P. Gaucher, and A. Morell, *Mat. Res. Bull.* **25**, 427 (1990).

[21] C. G. F. Stenger and A. J. Burggraaf, *Phys. Status Solidi* **A61**, 653 (1980).

[22] M. A. Akbas and P. K. Davies, *J. Mat. Res.* **12**, 2617 (1997); *J. Am. Ceram. Soc.* **83**, 119 (2000).

[23] P. K. Davies and M. A. Akbas, **221**, 27 (1999); *J. Phys. Chem. Solids* **61**, 159 (2000).

[24] J. K. Montgomery, M. A. Akbas, and P. K. Davies, *J. Am. Ceram. Soc.* **82**, 3481 (1999).

[25] Y. Yan, S. J. Pennycook, Z. Xu, and D. Viehland, *Appl. Phys. Lett.* **72**, 3145 (1998).

[26] B. P. Burton, *Phys. Rev.* **B59**, 6087 (1999); *J. Phys. Chem. Solids* **61**, 327 (2000).

[27] L. E. Cross, *Ferroelectrics* **76**, 241 (1987); *ibid* **151**, 305 (1987)

[28] L. Néel, *C. R. Acad. Sci. Paris* **228**, 664 (1949).

[29] Z. G. Lu and G. Calvarin, *Phys. Rev.* **B51**, 2694 (1995).

[30] D. Viehland, S. J. Jang, L. E.Cross, and M. Wuttig, *J. Appl. Phys.* **68**, 2946 (1990).

[31] D. Viehland, J. F. Li, S. J. Jang, L. E. Cross and M. Wuttig, *Phys. Rev.* **B43**, 8316 (1991).

[32] D. Viehland, M. Wuttng, L .E. Cross, Ferroelectrics, **120**, 71 (1991).

[33] E. V. Colla, E. Yu Koroleva, N. M. Okuneva, and S. B. Vakhrushev, *J. Phys.: Condens. Matter* **4**, 3671 (1992); *Phys. Rev. Lett.* **74**, 1681(1995).

[34] H. M. Christen, R. Sommer, N. K. Yushin, and J. J. van der Klink, *J. Phys.: Condens. Matter* **6**, 2631 (1994).

[35] R. Blinc, J. Dolinšek, A. Gregorovic, B. Zalar, C. Filipic, Z. Kutnjak, A. Levstik, and R. Pirc, *Phys. Rev. Lett.* **83**, 424 (1999); *J. Phys. Chem. Solids* **61**, 177 (2000).

[36] R. Pirc and R. Blinc, *Phys. Rev.* **B60**, 13470 (1999).

[37] A. Levstik, Z. Kutnjak, C. Filipic, and R. Pirc, *Phys. Rev.* **B57**, 11204 (1998).

[38] V. Bobnar, Z. Kutnjak, R. Pirc, R. Blinc, and A. Levstik, *Phys. Rev. Lett.* 84, 5892 (2000).

[39] A. E. Glazounov and A. K. Tagantsev, *Phys. Rev. Lett.* **85**, 2192 (2000).

[40] R. Pirc, R. Blinc, and Z. Kutnjak, *Phys. Rev.* **B65**, 214101 (2002).

[41] Z.-G. Ye and H. Schmid, *Ferroelectrics* **145**, 83 (1993).

[42] G. Calvarin, E. Husson, and Z.-G. Ye, *Ferroelectrics* **165**, 349 (1995).

[43] H. Mamiya, I. Nakatani, and T. Furubayashi, *Phys. Rev. Lett.* **80**, 177(1998).

[44] B. A. Strukov, E. L. Sorkin, V. M. Rizak, N. K. Yushin, and L. M. Sapozhnikova, *Sov. Phys. – Solid State* **31**, 1719 (1989).

[45] A. Fouskova, V. Kohl, N. N. Krainik and I. E. Mylnikova, *Ferroelectrics* **24**, 119 (1981).

[46] J. H. Choy, J. S. Yoo, S. G. Kang, S. T. Hong, and D. J. Kim, *Mat. Res. Bull.* **25**, 283 (1990).

[47] S. L. Swartz and T. R. Shrout, *Mat. Res. Bull.* **17**, 1245 (1982).

[48] W. N. Lawless, T. Nakamura, M. Takashige, and S. L. Swartz, *J. Phys. Soc. Jpn.* **52**, 207 (1983).

[49] C. -S. Tu, V. H. Schmidt, and I. G. Siny, *J. Appl. Phys.* **78**, 5665 (1995).

[50] G. A. Smolenskii, N. K. Yushin, S. I. Smirnov, and G. Gulyamov, *Sov. Phys. – Solid State* **28**, 522 (1986).

[51] A. Y. Wu and R. J. Sladek, *Phys. Rev.* **B27**, 2089 (1983).

[52] D. A. Ackerman, D. Moy, R. C. Potter, A. C. Anderson, and W. N. Lawless, *Phys. Rev.* **B23**, 3886 (1981).

[53] P. W. Anderson, B. I. Helperin, and C. M. Varma, *Philos. Mag.* **25**, 1 (1972).

[54] W. A. Phillips, *J. Low Temp. Phys.* 7, 351 (1972).

[55] R. C. Zeller and R. O. Pohl, *Phys. Rev.* **B4**, 2029 (1971).

[56] U. Buchenau, N. Nucker, and A.-J. Dianoux, *Phys. Rev. Lett.* **53**, 2316 (1984).

[57] S. G. Lushnikov, S. N. Gvasaliya, and I. G. Siny, *Physica* **B263-264**, 286 (1999).

[58] S. N. Gvasaliya, S. G. Lushnikov, I. L. Sashin, and I. G. Siny, *Crystallogr. Rep.* **44**, 284 (1999).

[59] F. M. Jiang and S. Kojima, *Appl. Phys. Lett.* **77**, 1271 (2000); *Phys. Rev.* **B62**, 8572 (2000).

[60] F. Jiang, S. Kojima, C. Zhao, and C. Feng, *J. Appl. Phys.* **88**, 3608 (2000).

[61] L. Gil, M. A. Ramos, A. Bringer, and U. Buchenau, *Phys. Rev. Lett.* **70**, 182 (1993).

[62] S. N. Gvasaliya, S. G. Lushnikov, Y. Moriya, H. Kawaji, and T. Atake, *Physica* **B305**, 90 (2001); *Crystallogr. Rep.* **46**, 1025 (2001).

[63] V. Mazzacurati, M. Montagna, O. Pilla, G Viliani, G. Ruocco, and G. Signorelli, *Phys. Rev.* **B45**, 2126 (1992).

[64] A. Bernasconi, T. Sleator, D. Posselt, J. K. Kjems, and H. R. Ott, *Phys. Rev.* **B45**, 10363 (1992).

[65] S. Nomura, K. Toyama, and K. Kaneda, *J. Phys. Soc. Jpn.* **21**, L624 (1982).

[66] S. Kawashima, M. Nishida, I. Ueda, and H. Ouchi, *J. Am. Ceram. Soc.* **66**, 421 (1983).

[67] J. Srinivas, E. D. Dias, and G. S. Murthy, *Bull. Mat. Sci.* **20**, 23 (1997).

[68] S. N. Gvasaliya, S. G. Lushnikov, and I. L. Sashin, Private Communication.

[69] H. D. Rosenfeld and T. Egami, *Ferroelectrics* **158**, 351 (1994); *ibid*, **164**, 133 (1995).

[70] W. Cochran, *Phys. Rev Lett.* **3**, 412 (1959).

[71] V. Gosula, A. Tkachuk, K. Chung, and H. Chen, *J. Phys. Chem. Solids* **61**, 221 (2000).

[72] S. Miao, J. Zhu, X. Zhang, and Z.-Y. Cheng, *Phys. Rev.* **B65**, 52101 (2002).

[73] H. Suga and S. Seki, *Faraday Discussions of Roy. Soc. Chem.* **69**, 221 (1980).

[74] K. Moriya, T. Matsuo, and H. Suga, *J. Phys. Chem. Solids* **44**, 1103 (1983).

Chapter 5

$Pb(Sc_{1/2}Ta_{1/2})O_3$

Perovskite Variable from Ferroelectric to Relaxor

— Preliminary Investigation on the Correlation between the Ferroelectric Phase Transition Behavior and the Degree of *B*-Site Cation Ordering

5.1. Introduction

As explained in *Chapter 4*, $Pb(B'_{1/3}B''_{2/3})O_3$-type lead-based complex perovskite oxides, where $B' = B^{2+}$ and $B'' = B^{5+}$, show the tendency to form the 1:1 *B*-site cation order regardless of the 1:2 occupancy of *B'* and *B''*. For example, in $Pb(Mg_{1/3}Nb_{2/3})O_3$ (PMN) and $Pb(Mg_{1/3}Ta_{2/3})O_3$ (PMT), which are typical relaxors, the 1:1 *B*-site cation ordered nanodomains with a size of ~ 2 nm are formed in the disordered matrix **[1-4]**. For the actual composition in these ordered domains $Pb(B^{I}_{1/2}B^{II}_{1/2})O_3$, where B^{I} and B^{II} are the alternate positions on the *B*-site sublattice, two models have been proposed, i.e., the space charge model $[Pb(B'_{1/2}B''_{1/2})O_3]^{1/2-}$ and the random layer model $Pb[(B'_{2/3}B''_{1/3})_{1/2}B''_{1/2}]O_3$ **[1]**. In the former model, the domain growth is strongly inhibited by the minimization of electrostatic energy and the 1:2 occupancy of *B'* and *B''*, while in the latter model, it is expected to occur under a kinetically active condition if the ordered state is thermodynamically stable. In fact, no domain growth has been observed in PMN even if a sample is subjected to thermal treatments under various conditions **[1,2,5,6]**, while the domains growth to a size of ~ 5 nm has been observed in PMT annealed at 1325 °C for 48 h **[4]**. This result on PMT strongly supports the random layer model and suggests the existence of an order-disorder phase transition on the *B*-site cation arrangement, while the absence of domain growth in PMN has been attributed to the existence of an order-disorder phase transition point in the temperature region where the ionic movement is kinetically inactive **[4]**. From the standpoint of the random layer model, the formation of the 1:1 *B*-site cation order results in the formation of the random layers occupied by the random distribution of *B'* and *B''* in the ratio of 2:1, and the existence of *B''* ions in the random layers gives rise to the local lattice strain field, which is considered as the primary factor preventing the evolution of ferroelectric ordering **[4]**. Consequently, the size of the ferroelectric regions is restricted to nanoscale and most of the crystal remains a paraelectric matrix.

On the other hand, in the case of $Pb(B'_{1/2}B''_{1/2})O_3$-type perovskites, it is naturally expected that the 1:1 *B*-site cation order is formed because of the 1:1 occupancy of *B'* and *B''*. In this case, assuming B^{I} and B^{II}-positions should be exclusively occupied by *B'* and *B''* ions, respectively, namely the number of *B'*(*B''*) ions at B^{I}(B^{II})-positions $N_{B'}^{B^{I}}$ ($N_{B''}^{B^{II}}$) is always more than or equals to that of *B'*(*B''*) ions at B^{II}(B^{I})-positions $N_{B'}^{B^{II}}$ ($N_{B''}^{B^{I}}$), the degree of ordering σ can be defined by

$$\sigma = \frac{N_{B'}^{B^{I}} - N_{B'}^{B^{II}}}{N_{B'}} = \frac{N_{B''}^{B^{II}} - N_{B''}^{B^{I}}}{N_{B''}} \quad (0 \le \sigma \le 1), \tag{5.1}$$

where $N_{B'}$ and $N_{B''}$ are the total number of the *B'* and *B''* ions, respectively, and $N_{B'} = N_{B''}$. When the B^{I} and B^{II}-positions are exclusively occupied by *B'* and *B''* ions, respectively, i.e., $N_{B'}^{B^{I}}$ ($N_{B''}^{B^{II}}$) = $N_{B'}$ ($N_{B''}$) and $N_{B'}^{B^{II}}$ ($N_{B''}^{B^{I}}$) = 0, σ becomes 1, which means the complete order. As the arrangement of *B'* and *B''* becomes random, the value of σ decreases. When the B^{I} and B^{II}-positions are occupied by the same number of *B'*(*B''*) ions, i.e., $N_{B'}^{B^{I}}$ ($N_{B''}^{B^{II}}$) = $N_{B'}^{B^{II}}$ ($N_{B''}^{B^{I}}$), σ equals to 0, which means disorder. It is considered that the *B*-site cation ordering is driven by the difference in ionic radius rather than valence between *B'* and *B''* **[4]**. Thus, all of $Pb(B'_{1/2}B''_{1/2})O_3$-type perovskites do not always form the 1:1 *B*-site cation ordered arrangement. For example, in $Pb(Fe_{1/2}Nb_{1/2})O_3$ (PFN) and $Pb(Fe_{1/2}Nb_{1/2})O_3$ (PFT), the *B*-site cation disordered arrangement, i.e., the state with $\sigma = 0$, is always realized, and these are ferroelectrics (and also antiferromagnets because of the existence of magnetic Fe^{3+} ions) **[7]**. On the other hand, in $Pb(Mg_{1/2}W_{1/2})O_3$ (PMW), the complete 1:1 *B*-site cation ordered arrangement, i.e., the state with $\sigma = 1$ is always realized, and this is antiferroelectric **[7]**. Thus, $Pb(B'_{1/2}B''_{1/2})O_3$-type perovskites with $\sigma = 0$ or 1 show (anti)ferroelectric behavior.

In addition to these complete 1:1 *B*-site cation ordered and disordered $Pb(B'_{1/2}B''_{1/2})O_3$-type perovskites, there is another group of $Pb(B'_{1/2}B''_{1/2})O_3$-type perovskites whose degree of ordering σ can be controlled by suitable thermal treatments **[7]**. Lead scandium tantalate, $Pb(Sc_{1/2}Ta_{1/2})O_3$ (PST), is one of this type of compounds. In PST, the value of σ is decreased by quenching from a high temperature (~ 1600 °C) and increased by annealing at a relatively low temperature (~ 1000 °C). Although PST with $\sigma \sim 1$ is normal ferroelectric, it approaches relaxor with decreasing σ. In normal ferroelectrics, ferroelectric long-range order is established below a ferroelectric phase transition point, while in relaxors, the ferroelectric order is restricted to very short-range. Therefore, it is expected that in PST, ferroelectric domain size can be controlled from macroscale to nanoscale by controlling σ through thermal treatments. Feasibility of controlling σ is conducted by the competition between the thermodynamic stability and the kinetics, and it implies the existence of an order-disorder phase transition on the *B*-site cation arrangements in PST similar to PMT. Actually; however, the existence of an order-disorder phase transition has not been confirmed because the expected transition point is

at a very high temperature, probably above 1600 °C, and the compound is decomposed at such a high temperature. Therefore, the disordered state, i.e., the state with $\sigma = 0$, in PST has not been reported so far. Taking this hypothetical order-disorder phase transition into account, there are two types of phase transitions in PST: a ferroelectric phase transition and an order-disorder phase transition on the *B*-site cation arrangements, and it seems that both transitions are closely related to each other.

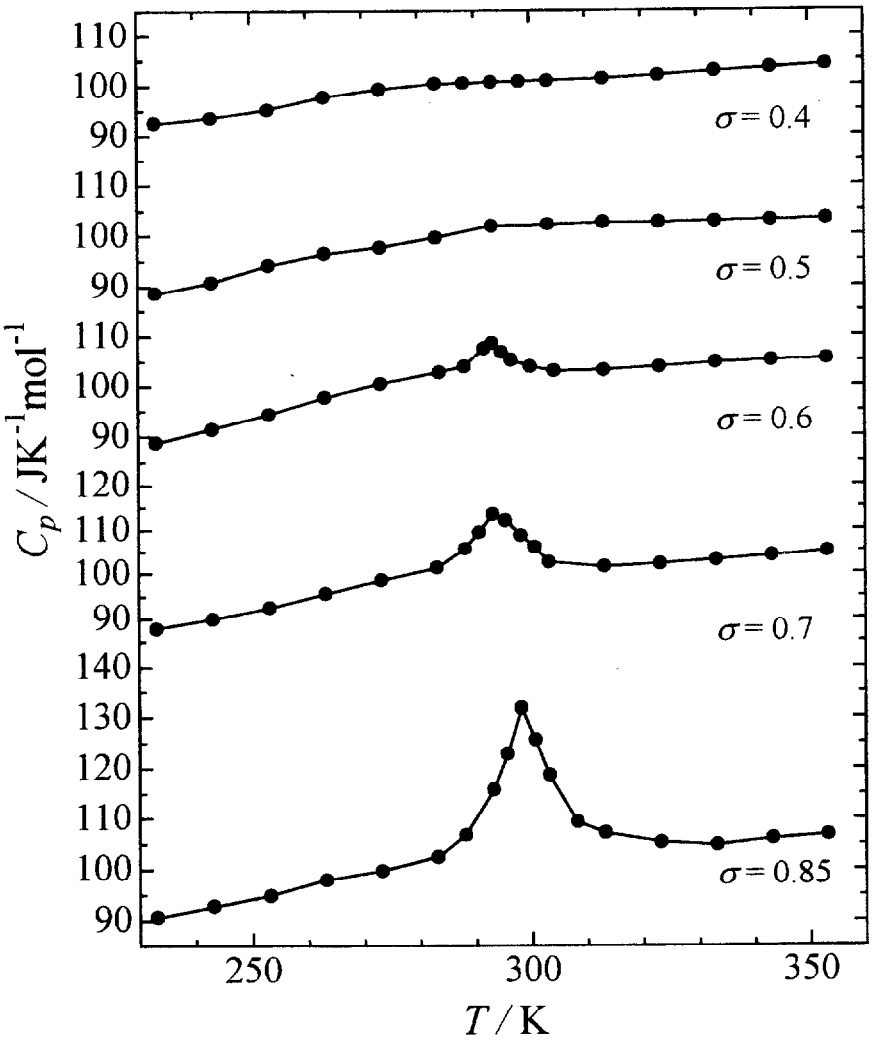

Fig.5.1. Heat capacity of PST ceramic samples with various degree of *B*-site cation ordering measured by Setter and Cross [9] using DSC.

PST was for the first time synthesized by the research group of Smolenskii in late 1950's but the variation of the dielectric property with respect to the *B*-site cation ordering has been investigated by Setter *et al.* [8-10] and Stenger *et al.* [11,12] since 1979. Setter and Cross

investigated the properties of PST ceramic samples subjected to thermal treatments under various conditions by dielectric constant measurements, X-ray diffractometry [8], DSC [9], and Raman scattering [10], and found that the dielectric property of PST changed from normal ferroelectric to relaxor with decreasing σ. However, it is difficult to approach the mechanism of a phase transition only by simple methods as used by them. PST has not been studied so much as PMN, and the systematical study on the ferroelectric phase transition behavior with respect to the variation of the degree of ordering has not been made yet from both structural and thermodynamic aspects. In fact, Setter and Cross [9] also measured the heat capacity of PST with various values of σ using DSC around the ferroelectric phase transition and reported that the heat capacity anomaly become smaller and finally vanished at $\sigma = 0.5$ with decreasing σ (Fig.5.1), but the ferroelectric phase transition behavior does not seem to be so simple. On the analogy of PMN and PMT, it is expected that the heat capacity anomaly of PST does not vanish but broaden out over a wide temperature range with decreasing σ. In addition, it is very interesting how the lattice contribution, especially the anomalous large low temperature heat capacity observed in PMN and PMT relaxors, changes with σ, but the heat capacity reported previously was measured only around the ferroelectric phase transition and DSC itself is not suitable for a heat capacity measurement. Thus, it is required to provide the definitive heat capacity data of PST in order to elucidate the phase transition behavior.

In this chapter, the preliminary study is made on the variation of the ferroelectric phase transition behavior of PST by heat capacity measurements using a thermal relaxation technique for single crystals subjected to thermal treatments under various conditions.

5.2. Experimental

5.2.1. Sample Preparation

Synthesis

PST was for the first time synthesized by the research group of Smolenskii as a ceramic sample in late 1950's. After that, Setter and Cross [13] for the first time succeeded to synthesize the single crystal of PST in 1980. In the present study, single crystals of PST were synthesized mainly according to the procedure reported by Setter and Cross [13]. Prior to the synthesis of the single crystals, it is necessary to synthesize a powder sample of PST.

Powder sample of PST was synthesized by a solid phase reaction technique to be used as seeds of the single crystals and the sacrificial powder in thermal treatments for the single crystals. Since PST also includes five-valence cation, i.e., Ta ion, similar to PMN and PMT, a

pyrochlore impurity is easily formed with the perovskite. Although Setter and Cross [13] synthesized a powder sample of PST by mixing starting powder materials of PbO, Sc_2O_3, and Ta_2O_5 directly in stoichiometric proportions, the small traces of the pyrochlore impurity was confirmed by powder X-ray diffraction. To avoid the formation of the pyrochlore impurity, the wolframite precursor $ScTaO_4$ was synthesized in advance. Powder materials of Sc_2O_3 (Rare Metallic Co., Ltd., 99.9 %) and Ta_2O_5 (Hikotaro Shudzui Co., Ltd., 99.9 %) were mixed in stoichiometric proportions using an ethanol medium for 1 h. This powder mixture was put in an alumina crucible and then placed in a furnace. The powder mixture was heated in air at 1400 °C for 12 h. The heated powder was reground and then reheated at 1400 °C for 24 h. The resultant powder was identified to be a single phase of the wolframite structure by powder X-ray diffraction. The precursor and PbO (Rare Metallic Co., Ltd., 99.99 %) were mixed in the same manner. At that time, 3 mol% excess PbO were added taking account of lead loss at a high temperature. This powder mixture was dried in an oven and then put into an alumina Tamman crucible. The Tamman crucible plugged with kaolinite wool was placed in the furnace. The powder mixture was heated at 900 °C for 12 h, and reheated at 1300 °C for 1 h with intermediate grinding. The resultant powder was identified to be a single phase of the cubic perovskite ($Fm\bar{3}m$) by powder X-ray diffraction. This powder sample is denoted as P-as grown.

The single crystals of PST were synthesized by a flux method. The PST powder and flux powders of PbO, PbF_2 (Rare Metallic Co., Ltd., 99.99 %), and B_2O_3 (do., 99.999 %) were mixed in the mass ratio of 3:8:8:1, respectively. The powder mixture was put in a platinum crucible covered with a platinum lid. The crucible was placed in the furnace and then rapidly heated up to 1250 °C under the oxygen atmosphere. After soaking at this temperature for 4 h, the crucible was slowly cooled down to 1000 °C at the rate of 3 °C/h and then down to 900 °C at the rate of 5 °C/h. At 900 °C, the furnace was turned off, and the crucible was brought to room temperature. The flux was dissolved with 30 % hot nitric acid and the products with a single crystal form were isolated. There were two types of single crystals in the products: one had a rectangular parallelepiped shape and a yellow color, while the other had a polyhedral shape and an orange color. The former and latter crystals were identified to be perovskite and pyrochlore phases, respectively, by powder X-ray diffraction. Therefore, the crystals with a yellow color could be considered as PST and its crystal structure was identified to be the cubic perovskite ($Fm\bar{3}m$) at room temperature (Fig.5.2), but weak diffraction lines of the largest and second largest ones of the pyrochlore phase were also observed (marked with dots). In fact, unfortunately, a small amount of the pyrochlore crystals were contained inside of or clung tightly on the surface of most obtained PST crystals, which were excluded under an optical microscope. Thus, only a few PST single crystals of good quality were obtained, and these

good crystals were used for measurements. The maximum size of the obtained PST single crystals is about 2 mm on edge. These single crystals are denoted as SC-as grown.

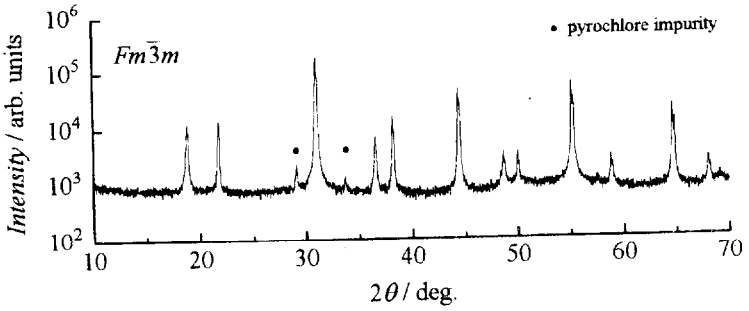

Fig.5.2. Powder X-ray diffraction pattern of PST as grown single crystal.

Thermal Treatments

In order to prepare the PST single crystals with various σ values, the synthesized single crystals were subjected to thermal treatments under various conditions. Several crystals were treated at the same time under the same condition. When the crystals were heated, these were put in a platinum crucible with a large amount of sacrificial powder of PST in order to protect them from the formation of deficiencies or complete decomposition. If there is no sacrificial powder, the perovskite is completely decomposed at a high temperature near 1600 °C. The crucible covered with a platinum lid was placed in a vertical tube furnace and then heated in air. The single crystals were (1) annealed at 950 °C for 110 h (SC-950), (2) quenched to liquid nitrogen temperature after annealed at 1400 °C for 1 h (SC-1400), and (3) quenched to liquid nitrogen temperature after annealed at 1560 °C for 20 min (SC-1560). In addition, one of the SC-1400 crystals was reannealed at 950 °C for 110 h after the heat capacity measurement in order to check the reversibility of the phase transition behavior. This crystal is denoted as SC-1400-950. After the thermal treatments, there was no apparent change in the crystals, while the color of the sacrificial powder in the vicinity of the surface changed from light to deep yellow. This part was identified to be the pyrochlore phase by powder X-ray diffraction. However, there was also no change in the inner part, which touched the crystals directly, and it was confirmed that the perovskite phase survived. Since the surviving sacrificial powder was used for some analyses, these powder samples were denoted as P-950, P-1400, and P-1560, treated with SC-950, SC-1400, and SC-1560, respectively.

Determination of Degree of Ordering σ

The 1:1 *B*-site cations ordered arrangement, i.e., NaCl structure on the *B*-site sublattice, forms the superlattice structure with the double period of the basic perovskite unit cell. Thus, the superlattice reflections due to the unit cell doubling are observed in the diffraction pattern besides the basic perovskite reflections. The intensities of these superlattice reflections increase with increasing the degree of ordering σ. Thus, the value of σ can be roughly estimated by the relative intensities of the superlattice reflections to basic reflections, and the nearest basic reflection to a superlattice reflection is usually selected for the estimation. In the case of space group $Fm\bar{3}m$, the [200] and [222] basic reflections can be used for the [111] and [311] superlattice reflections, respectively, and the value of σ is determined by

$$\sigma = \sqrt{\left(\frac{I_{111}}{I_{200}}\right)_{\text{observed}} \Big/ \left(\frac{I_{111}}{I_{200}}\right)_{\text{calculated } \sigma=1}} \quad \text{or} \quad \sigma = \sqrt{\left(\frac{I_{311}}{I_{222}}\right)_{\text{observed}} \Big/ \left(\frac{I_{311}}{I_{222}}\right)_{\text{calculated } \sigma=1}} \tag{5.2}$$

In the present study, since the amount of the single crystals was very small and insufficient to estimate the value of σ using a laboratory X-ray diffractometer, the estimation was performed only for the powder samples of P-as grown, P-950, P-1400, and P-1560 in order to confirm the variation of σ through thermal treatments.

5.2.2. Heat Capacity Measurements

All heat capacity measurements were performed between 2 K and 300 K by a thermal relaxation technique because the amount of the single crystals was too small to be measured by an adiabatic method.

SC-as grown

The mass of the single crystal used for the measurement was 25.41 mg (6.902 μmol). The contribution of the sample to the total heat capacity was 86, 92, 84, 69, 53 and 48 % at 5, 10, 50, 100, 200, and 300 K, respectively.

SC-950

The mass of the single crystal used for the measurement was 19.50 mg (5.297 μmol). The contribution of the sample to the total heat capacity was 83, 91, 80, 63, 46, and 42 % at 5, 10, 50, 100, 200, 300 K, respectively.

SC-1400

The mass of the single crystal used for the measurement was 14.85 mg (4.034 μmol). The contribution of the sample to the total heat capacity was 78, 87, 75, 57, 40, and 34 % at 5, 10, 50, 100, 200, 300 K, respectively.

SC-1560

The mass of the single crystal used for the measurement was 11.93 mg (3.241 μmol). The contribution of the sample to the total heat capacity was 71, 82, 69, 50, 34, and 28 % at 5, 10, 50, 100, 200, 300 K, respectively.

SC-1400-950

The mass of the single crystal used for the measurement was 14.69 mg (3.990 μmol). The contribution of the sample to the total heat capacity was 71, 82, 71, 55, 39, and 34 %at 5, 10, 50, 100, 200, 300 K, respectively.

5.2.3. Dielectric Constant Measurements

The dielectric constant and loss were measured between 100 K and 350 K with frequencies of 1, 3, 10, 30, 100, 300, and 1000 kHz. The same single crystals as used for the heat capacity measurements were used. The single crystals were polished with rough sandpaper to be a parallel-plate shape. Both surfaces of the parallel plates were polished with fine sandpaper. After that, gold was spattered on both surfaces to be electrodes of a parallel-plate capacitor. Gold wires with the diameter of 0.05 mm were connected to each electrode with silver paste (Engelhard K.K.). The measurements were carried out in both cooling and heating directions with the rate of 1 K/min.

SC-as grown

The thickness and the square of the sample were 0.50 mm and 2.3 mm^2, respectively. The effective voltage of the measurement AC field was 1 V_{rms}, and so the field strength was 20 V_{rms}/cm, which was weak enough to obtain normal dielectric response.

SC-950

The thickness and the square of the sample were 0.70 mm and 2.1 mm^2, respectively. The effective voltage of the measurement AC field was 1 V_{rms}, and so the field strength was 14 V_{rms}/cm, which was also weak enough.

SC-1400

The thickness and the square of the sample were 0.54 mm and 4.5 mm^2, respectively. The effective voltage of the measurement AC field was 1 V_{rms}, and so the field strength was 19 V_{rms}/cm, which was also weak enough.

SC-1560

The thickness and the square of the sample were 0.39 mm and 1.4 mm^2, respectively. The effective voltage of the measurement AC field was 1 V_{rms}, and so the field strength was 26 V_{rms}/cm, which was also weak enough.

5.2.4. Differential Thermal Analysis

In order to investigate the phase transition behavior of the powder samples of PST, differential thermal analyses were carried out around the phase transition using a homemade differential thermal analyzer in both cooling and heating directions with the rate of 1 ~ 2 K/min. The samples were put in a glass tube, which has another tube to insert the one edge of a thermocouple at the center. The tube was evacuated and then sealed after introducing a small amount of helium gas (4 kPa at room temperature) for thermal exchange. The sample and the reference (α-Al_2O_3 powder) tubes were inserted to a large thermal bath of copper in a cryostat. The temperature of the thermal bath and the temperature difference between the sample and the reference were traced with type-E thermocouples, the signals of which were measured using digital multimeters.

5.3. Result and Discussion

First of all, it was confirmed whether thermal treatments affect the degree of ordering σ on the *B*-site cation arrangement. Fig.5.3 shows the results of powder X-ray diffraction for P-950, P-as grown, P-1400, and P-1560 around the [111] superlattice reflection, where the intensities of the two lines are normalized by the intensity of [200] basic perovskite reflection. As seen in this figure, the intensity of the [111] superlattice reflection is increased by annealing at a relatively low temperature for a long time and decreased by quenching from a high temperature. Thus, the degree of ordering σ is surely changed by a suitable thermal treatment. The σ value of each sample was estimated using Eq.(5.2) to be 0.95, 0.80, 0.70, and 0.50 for P-950, P-as grown, P-1400, and P-1560, respectively. It should be noted that these values of σ were

estimated for the powder samples treated simultaneously with the single crystals. Thus, although these are not exact values for the single crystals used for the heat capacity and dielectric constant measurements, it is expected that σ decreases in order of SC-950, SC-as grown, SC-1400, and SC-1560, and this order is assumed hereafter.

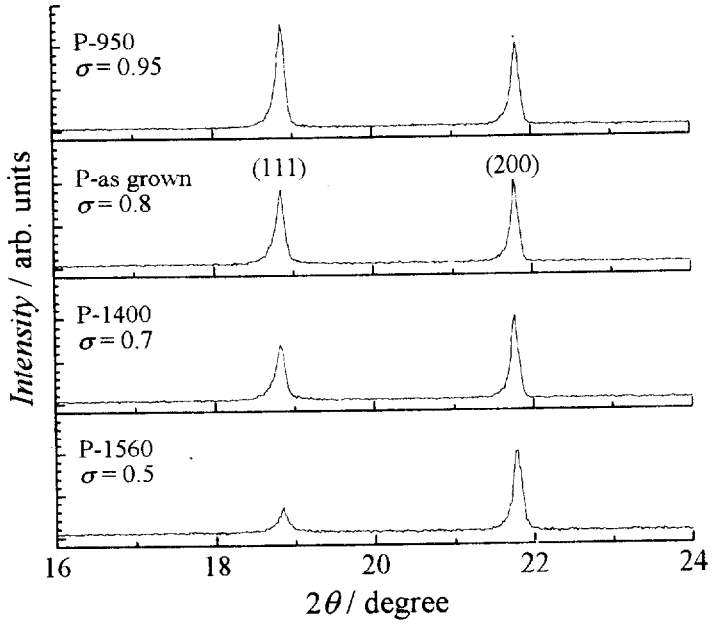

Fig.5.3. Variation of the intensity of the [111] superlattice reflection with respect to thermal treatments. The diffraction lines are obtained from the powder samples using Cu$K\alpha$ radiation X-ray with the wavelength of 0.1541 nm, where P-950 was annealed at 950 °C for 110 h, P-1400 was quenched to liquid nitrogen temperature after annealed at 1400 °C for 1 h, and P-1560 was quenched to liquid nitrogen temperature after annealed at 1560 °C for 20 min. The results are arranged in order of the degree of ordering σ, i.e., P-950, P-as grown, P-1400, and P-1560, from the top to bottom. Since the powder samples were subjected to thermal treatments simultaneously with the corresponding single crystal of SC-950, SC-as grown, SC-1400, and SC-1560, the expected values of σ for the single crystals can be arranged in the same order as the powder samples.

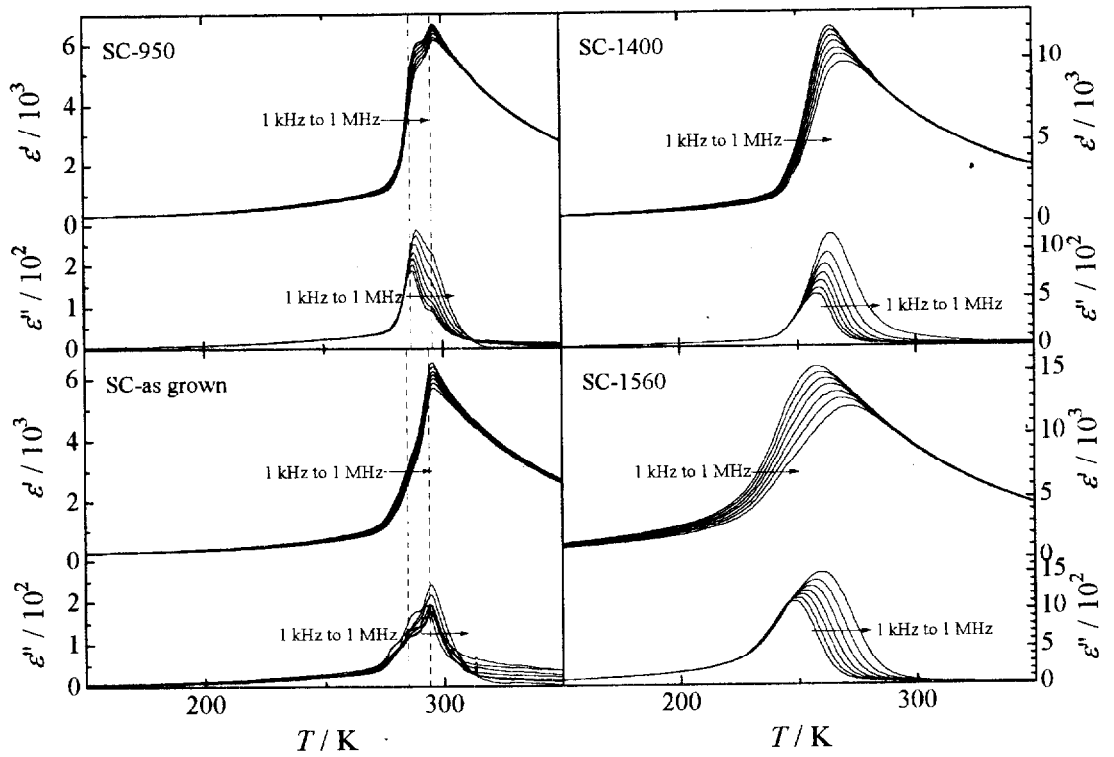

Fig.5.4. Complex dielectric constant of PST single crystals measured on heating, where SC-950 was annealed at 950 °C for 110 h, SC-1400 was quenched to liquid nitrogen temperature after annealed at 1400 °C for 1 h, and SC-1560 was quenched to liquid nitrogen temperature after annealed at 1560 °C for 20 min.

The complex dielectric constant measured on heating is shown in Fig.5.4. This figure clearly indicates that the dielectric property changes from ferroelectric to relaxor with decreasing σ. In SC-950, the dielectric constant shows an abrupt rise at about 275 K, which is a typical ferroelectric behavior, and forms a shoulder at 290 K and a peak at 296 K with increasing temperature. Namely, there are two dielectric anomalies in PST with high σ. A similar behavior has been observed in a single crystal synthesized by Raevskii *et al.* **[14]**, but has not been observed in a single crystal synthesized by Setter and Cross **[8,13]**. There is dispersion in the ferroelectric phase transition region between 290 and 310 K and the temperature of the shoulder slightly increases with increasing frequency, while that of the peak does not change. This behavior is more clearly seen in the dielectric loss, which shows a peak at 287 K and a shoulder at 295 K, contrary to the dielectric constant, and these temperatures correspond to the inflection points of the dielectric constant. In SC-as grown, the dielectric constant also rises up abruptly at about 275 K and shows a broad shoulder at 288 K and a peak

at 296 K with increasing temperature. Besides clear dispersion around the peak, there is also weak dispersion up to 350 K. The similar behavior is seen in the dielectric loss, which shows a shoulder at 285 K, a peak at 294 K, and strong dispersion above the peak temperature, where the dielectric loss increases with decreasing frequency contrary to below the peak temperature. In addition, both temperatures of the shoulder and the peak do not show frequency-dependence. Both SC-950 and SC-as grown surely show a ferroelectric behavior, which is suggested by the abrupt change of the dielectric constant, but the behavior of the shoulder at a lower temperature and the dispersion above the peak temperature are different. These results imply that the ferroelectric phase transition of PST with relatively high σ is not so simple as "normal" ferroelectric perovskites, e.g., $BaTiO_3$ and $PbTiO_3$. On the other hand, in SC-1400, the dielectric constant shows an abrupt rise at about 240 K, which seems to indicate a typical ferroelectric behavior, but relaxor-like broad peak and strong dispersion are observed around 265 K with increasing temperature, where a maximum value of the dielectric constant (~ 12000) becomes as twice as that of SC-950 and SC-as grown (~ 6500). Thus, SC-1400 shows an intermediate dielectric property between ferroelectric and relaxor. In addition, the starting temperature of the abrupt rise decreases by 35 K as compared with that of SC-950 and SC-as grown, which indicates that the ferroelectric phase transition point remarkably decreases with decreasing σ. Finally, in SC-1560, an abrupt rise of the dielectric constant is not observed with increasing temperature, while strong dispersion is observed even below a broad peak, which indicates a relaxor behavior as observed in PMN. However, a slight bending is seen around 240 K, which might indicate the occurrence of some phase transition and the incompleteness of changing into relaxor.

The difference between the dielectric constant measured at 1 kHz on heating and on cooling is shown in Fig.5.5. In SC-950, SC-as grown, and SC-1400, a thermal hysteresis phenomenon typical of a first-order phase transition is clearly observed between both runs where the peak temperature on cooling is lower than that on heating. This indicates the occurrence of a ferroelectric phase transition and the peak temperature can be usually considered as a phase transition point. On the other hand, in SC-1560, a peculiar thermal hysteresis phenomenon is observed below the peak temperature and the peak temperature does not change between both runs. In fact, the dielectric constant of SC-1560 measured on cooling is almost the same as that of PMN and there is no signature of a ferroelectric phase transition as shown in Fig.5.6. However the dielectric constant of PMN does not show a thermal hysteresis phenomenon between heating and cooling runs, while that of SC-1560 measured on heating goes through different route from that measured on cooling between 165 and 245 K. This result suggests a more complicated mechanism of PST, which seems to be closely related to the *B*-site cation ordering, but its details can not be clarified here.

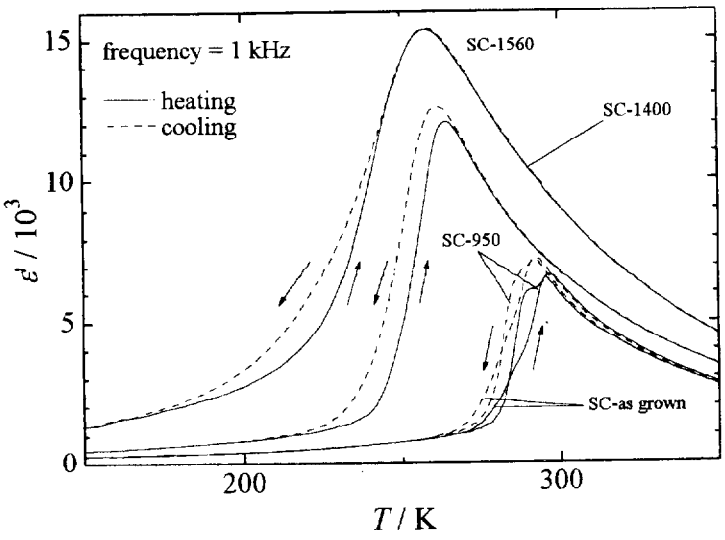

Fig.5.5. Difference between the dielectric constant of PST single crystals measured at 1 kHz on heating and on cooling. A thermal hysteresis phenomenon typical of a first-order phase transition is clearly observed in SC-950, SC-as grown, and SC-1400, while a peculiar one is observed below the peak temperature in SC-1560.

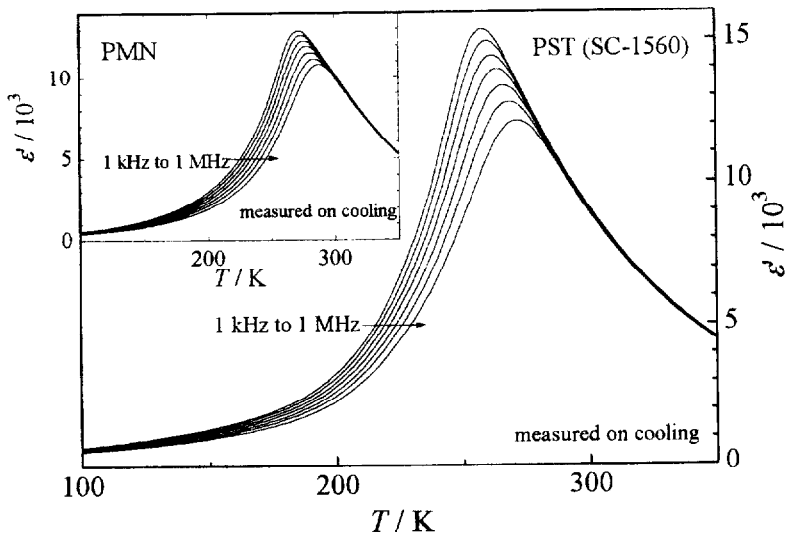

Fig.5.6. Dielectric constant of relaxor-like PST (SC-1560) measured on cooling and that of PMN is also shown in the inset for comparison.

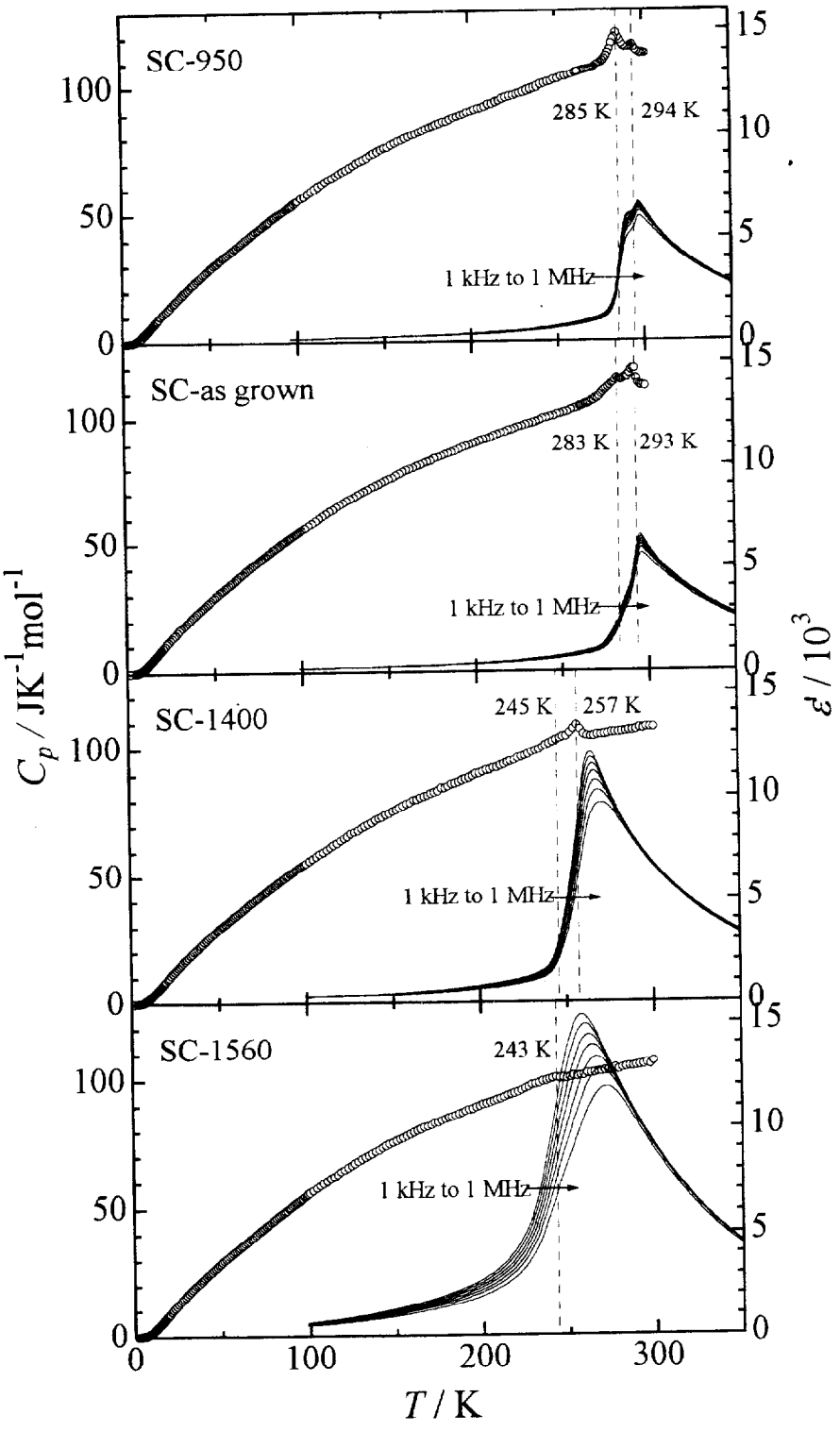

Fig.5.7. Heat capacity measured by a thermal relaxation method and dielectric constant measured on heating of PST single crystals, where the results are arranged in order of the expected degree of ordering, i.e., SC-950, SC-as grown, SC-1400, and SC-1500, from the top to bottom.

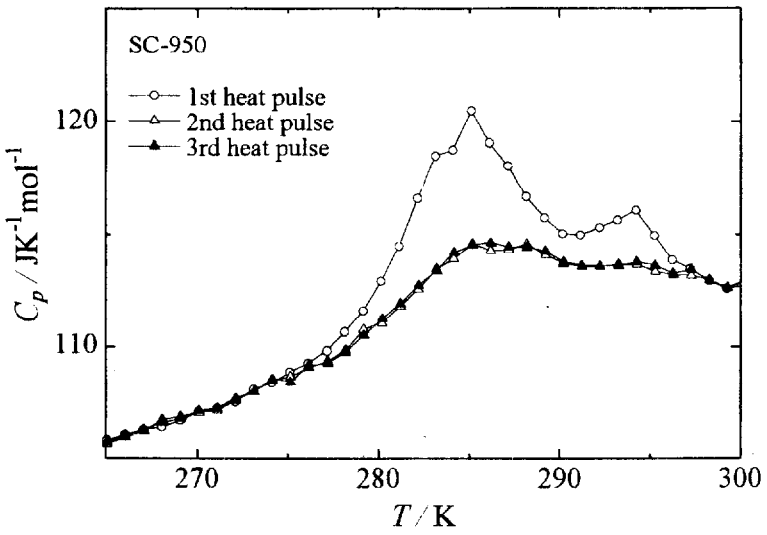

Fig.5.8. Thermal hysteresis phenomenon observed around the ferroelectric phase transition in the heat capacity measurements on SC-950 by a thermal relaxation method, where open circles denote the heat capacity data measured by a first heat pulse while open and closed triangles denote that measured by second and third heat pulses, respectively, at the same temperatures as the measurement by a first heat pulse after the system is considered to reach a thermal equilibrium state by an automatic measurement program.

The heat capacity of PST single crystals are shown in Fig.5.7 together with the dielectric constant measured on heating, where the results are arranged in order of the expected degree of ordering, i.e., SC-950, SC-as grown, SC-1400, and SC-1560, from the top to bottom. In SC-950, SC-as grown, and SC-1400, a remarkable heat capacity anomaly caused by the ferroelectric phase transition is observed but the data in the ferroelectric phase transition region do not show the true heat capacity because the ferroelectric phase transition of PST is of first-order as confirmed by the thermal hysteresis phenomenon in the dielectric constant. As explained in *Chapter 2*, it is impossible in principle to measure the heat capacity at a first-order phase transition by a thermal relaxation method, and of course it is also impossible to estimate the transition enthalpy and entropy. Fig.5.8 shows a thermal hysteresis phenomenon observed around the ferroelectric phase transition in the heat capacity measurements on SC-950 by a thermal relaxation method, where clear difference is seen between the data measured by a first heat pulse (open circles) and those measured by second and third heat pulses (open and closed triangles, respectively). However, there is no large difference between the data measured by second and third heat pulses at each temperature because these data show the heat capacity of a phase supercooled in a cooling process after the application of a first heat pulse. Thus, it can

be said that the data measured by a first heat pulse is much closer to the true value of the heat capacity, but even these data are quite different from the true values of the heat capacity because in a cooling process after the application of a heat pulse, an anomalous thermal relaxation phenomenon occurs due to a supercooling phenomenon, and consequently, a heat capacity value calculated on the basis of this relaxation process becomes incorrect. Thus, the heat capacity data in the phase transition region obtained in the present study can not be evaluated quantitatively but can be done qualitatively.

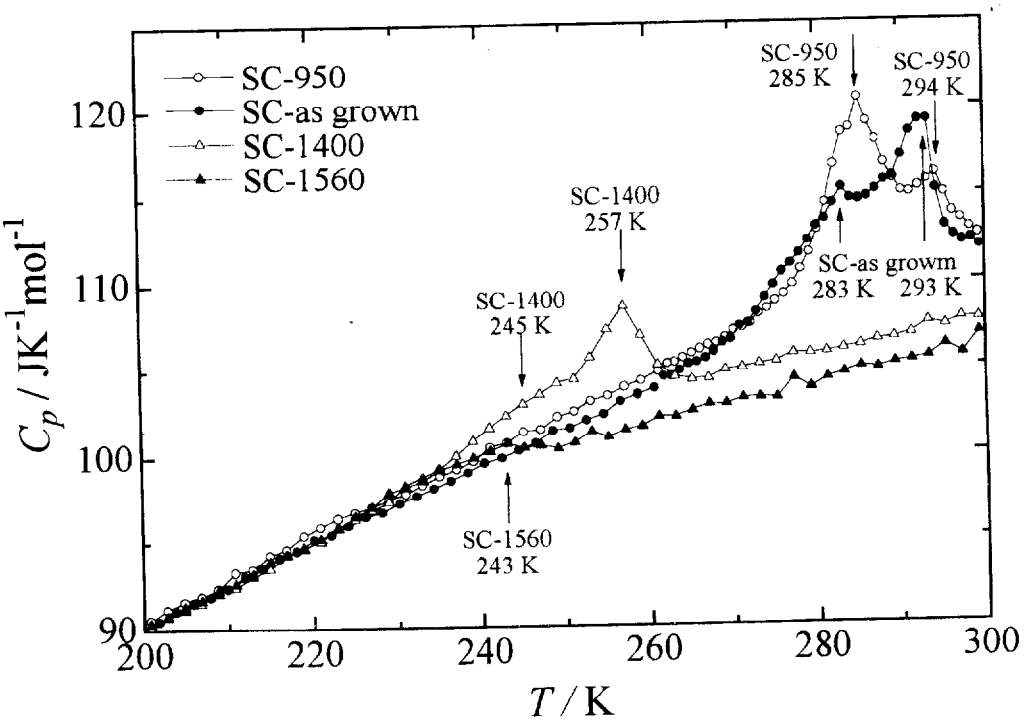

Fig.5.9. Heat capacity of PST single crystals measured by a thermal relaxation method around the phase transition region.

The heat capacity of PST single crystals measured by a thermal relaxation method around the ferroelectric phase transition is shown in Fig.5.9. In SC-950, a remarkable heat capacity is observed above about 270 K and the tail of the anomaly on the high temperature side is not caught even at 300 K, which is very broad in spite of first-order: in a normal first-order ferroelectric phase transition as seen in $BaTiO_3$, a sharp heat capacity is observed at a phase transition point. In addition, the anomaly has two peaks at 285 and 294 K, which seem to indicate two successive phase transitions and the existence of an intermediate phase between the high temperature paraelectric and low temperature ferroelectric phases. The peak temperatures

correspond to the inflection points of the dielectric constant, i.e., the peak and shoulder temperatures of the dielectric loss. This result is obtained for the first time in the present study, indicating that the ferroelectric phase transition is not "simple" and "normal". Also in SC-as grown, two heat capacity anomalies are observed at 283 and 293 K but the size of the lower anomaly becomes smaller than that of the higher anomaly as compared with SC-950, which corresponds to the broadening of the shoulder in the dielectric constant. In SC-1400, a remarkable heat capacity is observed at 257 K, while a broad one is also found around 245 K. Thus, there are also two anomalies in SC-1400. The temperatures of the higher and lower anomaly correspond to those of the inflection point and abrupt rise of the dielectric constant, respectively, which are extremely decrease by about 35 K relative to SC-950 and SC-as grown. In addition, the size of the anomaly seems to be smaller than that of SC-950 and SC-as grown, although the maximum value of the dielectric constant becomes larger. This suggests a striking change is induced to the ferroelectric phase transition behavior in PST crystals between SC-as grown and SC-1400 by the variation of σ through thermal treatments. Finally, in SC-1560, there is no remarkable heat capacity anomaly but a broad one is barely observed around 243 K, which corresponds to the bending in the dielectric constant curve measured on heating. Thus, the ferroelectric phase transition behavior of PST strongly depends on σ and the dielectric behavior surely changes from ferroelectric to relaxor with decreasing σ. Especially dielectric behavior strikingly changes between SC-as grown and SC-1400, and if the values of σ estimated from the powder samples correspond to those of the single crystal samples*, this change is induced around $\sigma = 0.7$. In addition, SC-950 and SC-as grown show a ferroelectric behavior but it is not a "normal" one such as observed in $BaTiO_3$ and $PbTiO_3$, which is indicated by the broad heat capacity anomaly with two peaks regardless of first-order. However, this particular phase transition behavior might be caused by the inhomogeneity or some impurity in the synthesized single crystals: the materials that are not components of PST were used as flux in the synthesis of PST, i.e., PbF_2 and B_2O_3, which remind of the change in the phase transition behavior in $PbZrO_3$ mentioned in *Chapters 1* and *2*, but it is impossible to synthesize PST single crystal without these kinds of flux. Taking this possibility into account, the phase transition behavior of the powder samples was checked using differential thermal analysis (DTA) because the powder sample was synthesized from the component oxides alone. The DTA traces on heating of P-950, P-as grown, and P-1400, are shown in Fig.5.10. In P-950, two endothermic peaks are clearly observed, while in P-as grown and P-1400, two peaks are also observed although one peak is a little unclear. Thus, the two peaks of the heat capacity anomaly can be considered as the nature of PST with high σ.

* The degrees of ordering σ of P-as grown and SC-as grown are expected to be different because both samples were synthesized in different ways and were not subjected to a thermal treatment unlike other samples.

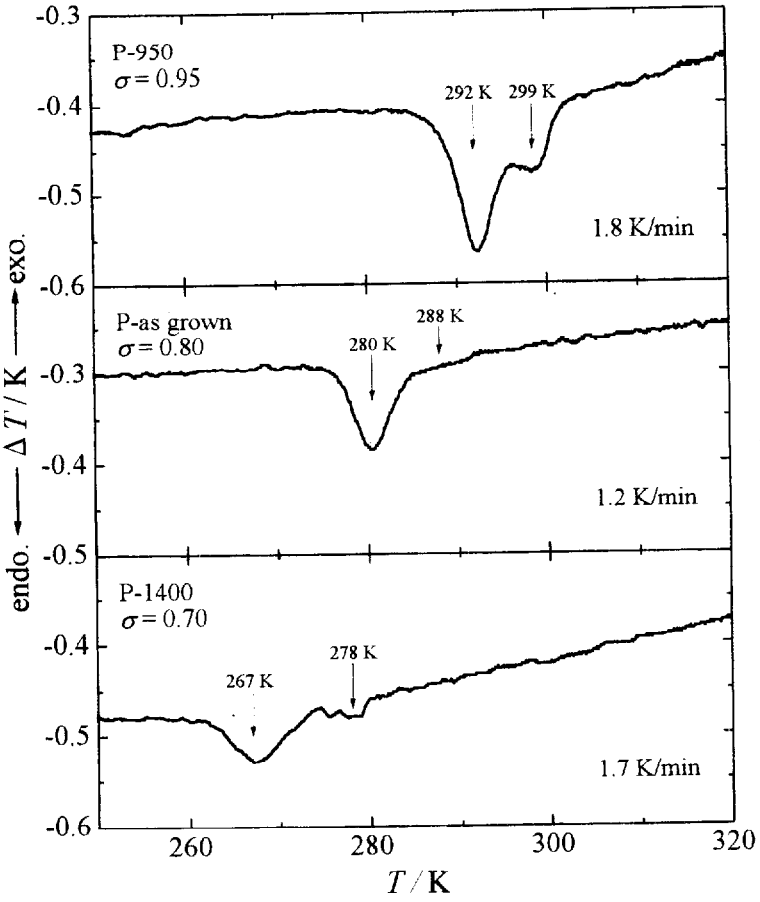

Fig.5.10. DTA traces of PST powder samples on heating.

On the other hand, there is no significant change in the heat capacity of PST single crystals except for the phase transition region, which seems to indicate the lattice contribution is not affected so much by the variation of σ and the consequent change in the ferroelectric phase transition behavior. Fig.5.11 shows the C_pT^{-3} *vs.* log$T$ plot of PST single crystals, where the comparison of PST (SC-as grown) with PMN and PMT relaxors is shown in the inset. As explained in *Chapter 4*, since the anomalous large heat capacity observed in PMN and PMT relaxors is the characteristic of relaxors with some topological disorder, it was expected that the heat capacity of PST at low temperatures remarkably decreased with changing the dielectric property from relaxor to ferroelectric. However, in fact, there is no significant change in the heat capacity. Besides, even the heat capacity of PST showing ferroelectric behavior, i.e., SC-950 and SC-as grown, is larger than that of PMN as shown in the inset of Fig.5.11. In addition, all of the lead-based complex perovskites shows a peak of C_pT^{-3} at 10 K and the maximum value increases with increasing the averaged mass of B-site cations: $Mg_{1/3}Ta_{2/3}$ = 133

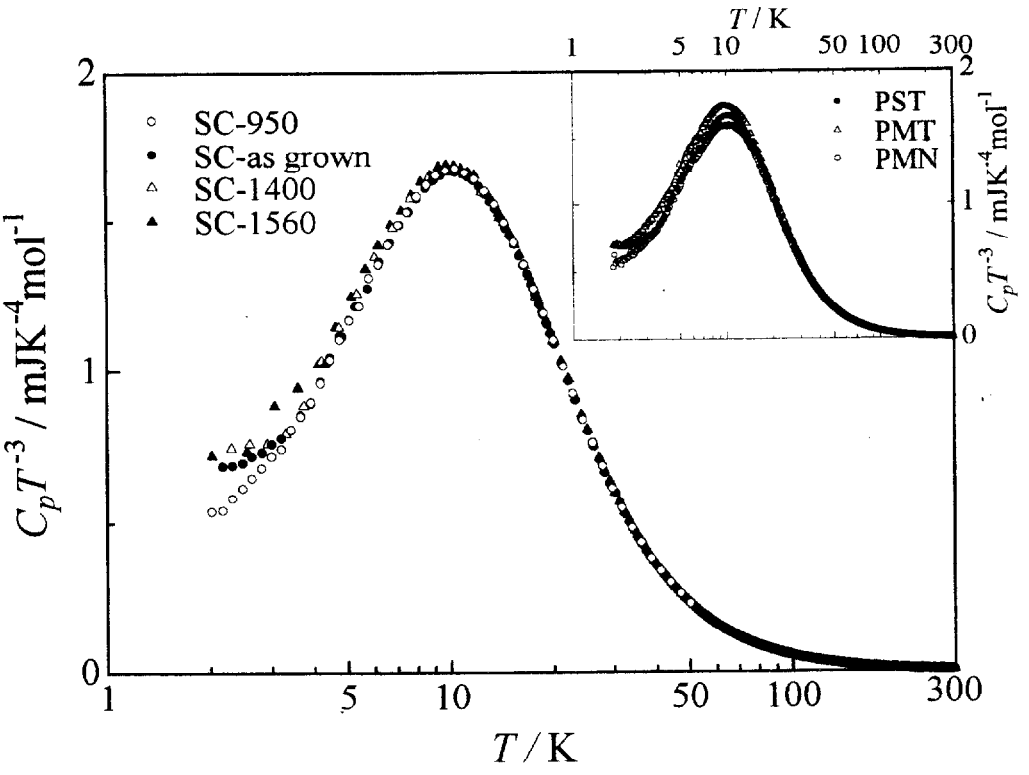

Fig.5.11. C_pT^{-3} *vs.* log$T$ plot of PST single crystals. The inset shows a comparison of PST (SC-as grown) with PMN and PMT relaxors.

in PMT, $Sc_{1/2}Ta_{1/2}$ = 113 in PST, and $Mg_{1/3}Nb_{2/3}$ = 74 in PMN. This result suggests that the additional low energy excitations found in PMN and PMT, e.g., the anomalous low frequency optical phonons similar to Boson peak, also exist in PST showing not only relaxor but also ferroelectric behavior. On the analogy of PMN and PMT, the low temperature phase of PST showing relaxor behavior should have the hetero-structure composed of ferroelectric nanoregions formed in a paraelectric matrix, while that of PST showing ferroelectric behavior should have a long-range ferroelectric ordered structure and there should not be topological disorder causing the anomalous large low temperature heat capacity because the long-range order should be formed on both the *B*-site cation arrangement and the lattice distortion producing spontaneous polarizations. Nevertheless, the heat capacity in the low temperature phase of PST does not change with the variation of σ. This result is very strange but seems to indicate a singularity of PST, or lead-based complex perovskites. Here, it can be only said that PST showing ferroelectric behavior is also "anomalous" as compared with "normal" perovskite ferroelectrics.

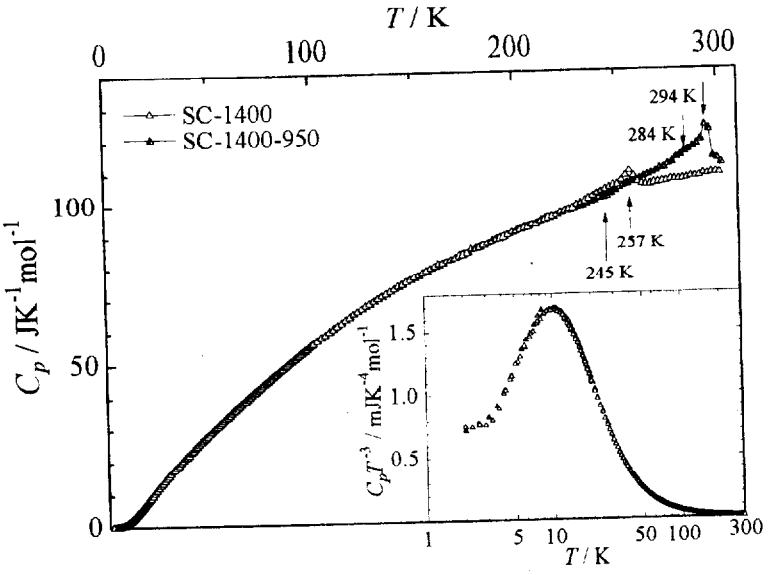

Fig.5.12. Heat capacity of PST single crystal quenched to liquid nitrogen temperature after annealed at 1400 °C for 1 h (SC-1400) and reannealed at 950 °C for 110 h after the former thermal treatment (SC-1400-950). The inset shows the C_pT^{-3} *vs.* log$T$ plot for clarity of the difference at low temperatures.

Finally, the result of checking the reversibility of the ferroelectric phase transition behavior with respect to thermal treatments, i.e., the variation of σ, is shown in Fig.5.12. The ferroelectric phase transition behavior of SC-as grown changes into that of SC-1400 by quenching to liquid nitrogen temperature after annealed at 1400 °C for 1 h, while that of SC-1400 can return to that of SC-950 by reannealing at 950 °C for 110 h although the size relation between the lower and higher anomalies is different from that in SC-950. Thus, the reversibility is surely confirmed in this experiment, and it makes clear that the *B*-site cation arrangement dominates the ferroelectric transition behavior.

5.4. Conclusion

In this chapter, the systematic investigations on the correlation between the ferroelectric phase transition behavior and the degree of *B*-site cation ordering σ on PST single crystals were carried out mainly by heat capacity measurements using a thermal relaxation method, and various singularities of PST were become clear. Especially, the ferroelectric behavior of PST with high σ has been considered as "normal" one, but in fact, it is quite "anomalous" as compared with "normal" perovskite ferroelectrics such as $BaTiO_3$ and $PbTiO_3$. Its singularities were confirmed by the broad heat capacity anomaly with two peaks regardless of first-order and the unchanged large low temperature heat capacity. On the analogy of PMN and PMT relaxors and normal ferroelectric $PbTiO_3$, PST single crystals with different values of σ should have different structures of the low temperature phase, and the low temperature heat capacity should change according to the change in the structure. Unfortunately, however, there have not been detailed and systematic structural studies on PST unlike PMN, and it is unclear what actually takes place in the structure of PST crystals. It is difficult to investigate it by a heat capacity measurement alone, especially using a thermal relaxation method: the accuracy of the data measured by a thermal relaxation method becomes lower with increasing temperature besides impossibility of a quantitative measurement of the heat capacity at a first-order phase transition. Thus, heat capacity measurements by an adiabatic method and systematic structural study on PST are highly desired for further understanding.

References

[1] J. Chen, H. M. Chan, and P. Harmer, *J. Am. Ceram. Soc.* **72**, 593 (1989).

[2] A. D. Hilton, D. J. Barber, C. A. Randoll, and T. R. Shrout, *J. Mater. Sci.* **25**, 3461 (1990).

[3] C. Boulesteix, F. Varnier, A. Llebaria, and E. Husson, *J. Solid State Chem.* **108**, 141 (1994).

[4] M. A. Akbas and P. K. Davies, *J. Mat. Res.* **12**, 2617 (1997); *J. Am. Ceram. Soc.* **83**, 119 (2000).

[5] N. de Mathan, E. Husson, P. Gaucher, and A. Morell, *Mat. Res. Bull.* **25**, 427 (1990).

[6] C. G. F. Stenger and A. J. Burggraaf, *Physica Stat. Sol.* **A61**, 653 (1980).

[7] C. A. Randall and A. S. Bhalla, *J. Appl. Phys.* **29**, 327 (1990).

[8] N. Setter and L. E. Cross, *J. Appl. Phys.* **51**, 4356 (1980).

[9] N. Setter and L. E. Cross, *J. Mater. Sci.* **15**, 2478 (1980).

[10] N. Setter and L. E. Cross, *Ferroelectrics* **37**, 551 (1981).

[11] C. G. F. Stenger, F. L. Scholten, and A. J. Burggraaf, *Solid State Commun.* **32**, 989 (1979).

[12] C. G. F. Stenger and A. J. Burggraaf, *Physica Stat. Sol.* **A61**, 275 (1980); *ibid.* **A61**, 653 (1980).

[13] N. Setter and L. E. Cross, *J. Cryst. Growth* **50**, 555 (1980).

[14] I. P. Raevskii, V. G. Smotrakov, A. A. Bokov, S. M. Zaitsev, and V. P. Filippenko, *Inorg. Mater.* 709 (1987).

Chapter 6

Summary

In the present study, typical lead-based complex perovskite relaxors $Pb(Mg_{1/3}Nb_{2/3})O_3$ (PMN) and $Pb(Mg_{1/3}Ta_{2/3})O_3$ (PMT) were investigated mainly by means of the heat capacity measurements in order to thermodynamically characterize the relaxor state in zero bias field and verify the validity of the physical models proposed to explain the relaxor behavior so far. The greatest objective of the present study was to detect the thermodynamic signature of the characteristic dielectric response in the relaxors. At the beginning, it was expected that there is a heat capacity anomaly corresponding to the dielectric anomaly in PMN over a very wide temperature range because the dielectric constant shows a very broad peak over a wide temperature range around 300 K. Thus, it was necessary to construct a new adiabatic calorimeter that enabled to measure the heat capacity above room temperature.

In *Chapter 2*, the detailed explanation was given for the adiabatic calorimeter newly constructed in the present study. It became possible to measure the heat capacity above room temperature with relatively high accuracy of ~ 0.3 % using this calorimeter. Besides this calorimeter, simple explanations were given for the experimental apparatuses and techniques utilized in the present study.

In *Chapter 3*, the normal perovskite ferroelectrics $BaTiO_3$ (BT), $PbTiO_3$ (PT), and antiferroelectric $PbZrO_3$ (PZ) were investigated and the features in their heat capacity were specified because it was expected that the singularities in the heat capacity of the relaxors could be extracted effectively by comparison with the typical perovskite (anti)ferroelectrics. From the results of the nonlinear least-square fitting to the heat capacity data using a combination of simple models for the lattice vibration, i.e., Debye, Einstein, and modified Einstein models, the following features were specified:

- There are specific lattice vibrational states at a low frequency below 5 THz common to these perovskites and their frequencies are effectively modulated by the ionic substitution. Namely, the frequency of the specific lattice vibrational mode shifts down to lower frequencies by the atomic mass effect due to the substitution of Ba by heavier Pb. On the other hand, the mass effect of the *B*-site cation between PT and PZ is reflected in a higher frequency region, because in the present case the mass of the *B*-site cations is smaller than

that of the *A*-site cations.

- In PZ, there is additional low energy excitation, which is characterized by the vibratinal states below 1 THz in the estimated distribution of the density of lattice vibrational states. If this can be attributed to the phonon, it results in anomalous low frequency optical phonons. On the other hand, it can be also considered due to another excitation, which is related to the antiferroelectricity of PZ, because such a low energy excitation was not found in the normal ferroelectric BT and PT.

- The heat capacity of BT and PT in the whole measurement temperature range between 2 and 420 K can be well described by a combination of the simple models, and the temperature-dependence of the heat capacity of these perovskites are quite normal as expected for metal oxides. On the other hand, PZ shows a significant discrepancy of the measured from the calculated values of the heat capacity above ~ 200 K, and the heat capacity shows a remarkable tendency to increase with increasing temperature even at 420 K. This result indicates the precursor phenomenon toward the antiferroelectric phase transition at about 500 K is observed even around room temperature.

In *Chapter 4*, typical lead-based perovskite relaxors PMN and PMT were investigated. At a glance, PMN and PMT showed no remarkable feature in the heat capacity as expected. However, compared with the normal perovskite (anti)ferroelectrics, the singularities in their heat capacity can be clearly extracted. Namely, PMN and PMT show anomalous large heat capacity below 30 K and the existence of a heat capacity anomaly in a higher temperature region. In this chapter, the origin of these singularities was discussed in detail. For the anomalous large low temperature heat capacity, the following points were clarified:

- The heat capacity value of PMN and PMT at 2 K is about four times larger than that calculated from Debye model whose characteristic temperature is estimated from the elastic data reported for PMN. This suggests the existence of low energy excitations associated with glasslike quantum mechanical two-level excitation.

- The maximum of C_pT^{-3} in PMN and PMT can be well described by three Einstein models. The highest frequency one around 2 THz corresponds to low frequency optical phonons, which are commonly found in the perovskites. The middle one around 1.5 THz is the main constituent of the maximum of C_pT^{-3} at 10 K and indicates the existence of anomalous low frequency optical phonons very similar to Boson peak in structural glasses.

The lowest one might also correspond to anomalous low frequency optical phonons, but it can be some low energy excitation related to the randomly oriented local polarizations because similar low energy excitation is also found in PZ, where the local polarizations are arranged in a anti-parallel manner. These additional low energy excitations can be regarded as the characteristics of the relaxors.

- The low temperature heat capacity of PMN below 30 K can be well described by fractal model. Thus, it can be concluded that some topological disorder in the relaxors strongly affects the lattice dynamics and result in the anomalous large low temperature heat capacity.

On the other hand, for the heat capacity anomaly in a higher frequency region, it was succeeded to obtain the excess heat capacity by estimating the lattice contribution using the simple models, and the following points were clarified.

- The heat capacity anomaly is found to be corresponding to the peak of the dielectric constant. Thus the anomaly originates from the same mechanism as the dielectric anomaly, i.e., the formation of the ferroelectric nanoregions (FNR).

- The estimated value of the excess entropy ΔS is ~ 3 $JK^{-1}mol^{-1}$ for both PMN and PMT. This large value of ΔS strongly suggests an order-disorder type of the formation mechanism of FNR. Assuming the expected value of ΔS between the fully ordered and disordered states is $R\ln 8$, the ratio of estimated ΔS to $R\ln 8$ ($\Delta S/R\ln 8$) is 20 %, which coincides with the volume ratio of FNR to the whole crystal (V_{FNR}/V) estimated by the structural refinements for PMN.

Based on the present results, the orientational glasslike nature of relaxors was also investigated. Assuming similar temperature dependence for the activation energy E_a for the thermal fluctuation of FNR with local polarizations to $\Delta S/R\ln 8$ and V_{FNR}/V, the dielectric relaxation process of PMN can be explained by a modified Arrhenius law with the temperature-dependent E_a, without cooperative freezing of dipoles at a finite temperature. The present results strongly support the "domain state model" rather than the "dipolar glass model" for the possible description of the relaxors.

In *Chapter 5*, the ferroelectric phase transition behavior of a characteristic lead-based complex perovskite $Pb(Sc_{1/2}Ta_{1/2})O_3$ (PST), the dielectric property of which changes from

ferroelectric into relaxor with decreasing the degree of *B*-site cation ordering σ, was investigated with respect to the change in σ. From the results of dielectric constant measurements and heat capacity measurements by a thermal relaxation method on the PST single crystals subjected to thermal treatments under different conditions, the following points were clarified.

- PST with high σ surely shows ferroelectric behavior but it is not "normal" but "singular" one, which is indicated by two anomalies in the complex dielectric constant and the heat capacity. Especially, the heat capacity anomaly is broad relative to the normal perovskite ferroelectrics such as BT and PT, regardless of first-order. This result suggests a complex mechanism of the ferroelectric phase transition in PST, where successive phase transition might takes place in a narrow temperature region over about 30 K.

- The dielectric behavior of PST changes from ferroelectric to relaxor with decreasing σ. The heat capacity anomaly shifts to lower temperatures and its size becomes smaller. However, it does not distinguish but broaden out over a wide temperature range like PMN and PMT.

I have studied thermodynamic properties of the lead complex perovskite relaxors, PMN, PMT and PST, and intended to complete this study with heat capacity measurements on ferroelectric and relaxor PST by an adiabatic method and the comparison of the results with those of PMN and PMT, because it is impossible to measure the heat capacity at a first-order phase transition by a thermal relaxation technique. However, it was very difficult to prepare an enough amount of the single crystals of PST with high quality to be measured by an adiabatic method. In addition, thermal treatments at high temperatures might cause the formation of lead deficiencies in PST crystals, and it is also difficult to prepare a large amount of the single crystals with a small value of σ. It can be only said here that the ferroelectric phase transition behavior of PST is quite unusual, and this seems to indicate the complicated mechanism. Further detailed investigation is obviously needed for PST.

On the other hand, there is not marked sample-dependence in the dielectric behavior of PMN and PMT: the maximum value and temperature of the dielectric constant do not depend on difference of samples so much. However, in the case of PST, the maximum value and temperature of the dielectric constant of as grown single crystals are different from samples. This seems to show a slight difference in σ caused by slight difference in the synthesis condition. In general, however, as grown single crystals of PST show a ferroelectric behavior: the value of σ of as grown single crystals should become large, because in a flux method temperature is

slowly decreased in order to promote crystallization, and therefore the increase of the value of σ is also promoted according to the thermodynamic stability under a kinetically active condition. Thus, in order to decrease the value of σ, it is necessary to quench a sample from a very high temperature. As already mentioned, however, annealing at a high temperature cause the formation of lead deficiencies, and it has been reported that the lead deficiencies strongly affect the dielectric properties of PST: these promote a sample to be relaxor. Thus, the dielectric behavior of PST quenched from a high temperature might be affected by two different factors, i.e., the decrease of the value of σ and the formation of lead deficiencies. However, in the present study, it seems that lead deficiencies are not formed in the samples because it was at least confirmed that the color of the samples did not change through thermal treatments: in the case that lead deficiencies are formed, the color of sample becomes darker. In general, it is necessary to take special care of a sample when the effects of thermal treatments on the dielectric properties of PST are investigated. On the other hand, recently, it has been reported that an as grown single crystals of PST shows relaxor behavior although the procedure and the conditions of the synthesis are the same as those in the present study. It is very strange because of the reason mentioned above. Dr. Lushnikov, who is my collaborator and one of the authors reporting the relaxor behavior of as grown PST, told me that he did not know the reason and "a sample synthesis is art!".

On the whole, PST is a very complex material and its properties seem to be strongly affected by some slight change in a sample. Thus, in order to investigate the properties of PST, it is necessary to take care of a sample, e.g., conditions of the synthesis and composition. There are still many questions in the properties and the structure of PST, and it might be caused by the quality of a sample. Further detailed investigations on PST are highly desired, and heat capacity measurements by an adiabatic method should be also performed using a good sample of PST.

There are also many questions in not only PST but also lead-based complex perovskite relaxors although some important points were clarified in this study. I think that relaxors are one of the group of materials providing a field of studies on the complex system and nanoscale science. Although it seems to be difficult to elucidate the mechanism causing the anomalous properties of lead-based complex perovskite relaxors, I believe that the investigations on these materials surely produce fruitful results for the development of science.

Acknowledgments

I was able to accomplish this study thanks to many people's help. First of all, I would like to express my gratitude to my supervisor, Professor Tooru Atake. He guided me into this study and has given me his knowledge generously. Especially, he taught me that it was very important for an experimental scientist to observe carefully and doubt everything. He reproved me when it was necessary and encouraged me when I really needed it. I really appreciate his instruction.

I would also like to express my gratitude to Associate Professor Hitoshi Kawaji, who has practically been my instructor. He has instructed me in everything related to this study, such as basic physics of relaxors, sample synthesis, calorimetry, design and construction of the adiabatic calorimeter, and so on. I could not accomplish this study without his instruction.

I would like to thank Research Associate Dr. Takeo Tojo for his advice on this study and instruction in operation of apparatuses. In addition, he often helped me when I was in some trouble. For example, he offered a personal computer and its peripherals when I was looking for a reasonable one. I was really helped by his kindness.

I would also like to thank Ms. Nobuko Kaga for her secretarial help and advice. She always took care of my situation and encouraged me. I really appreciate her kindness.

I am thankful to Dr. Jadwiga T. Sipowska at University of Michigan, U. S. A., for a great deal of encouragement and advice. In addition, she instructed me in English conversation when she was a guest professor at this laboratory. I would also like to thank her on this regard.

I have benefited greatly from useful conversations with other researchers interested in relaxors. Dr. Makoto Iwata at Nagoya Institute of Technology is one of such researchers. I would like to thank him for fruitful discussions on relaxors, especially on their orientational glasslike nature.

I would also like to thank my collaborators, Dr. Sergey Lushnikov and Dr. Severian Gvasaliya at A. F. Ioffe Physical Technical Institute, St. Petersburg, Russia, for useful discussions especially on the low temperature heat capacity of PMN, PMT, and BMT. In addition, they offered the data of inelastic neutron scattering experiments on PMN, PMT, and BMT. I am very grateful for their generosity.

I was much stimulated by my colleagues during the course of this study. I thank my colleague, Isao Yamashita. We often discussed about our studies and it was a great experience for me. In addition, he often helped me when I was in some trouble. I am also thankful on

this regard.

I also thank my junior colleague, Makoto Tachibana for his help and discussions. I want to work with him again someday.

I also thank all members of Atake-Kawaji Research Group who spent a good time together in this laboratory.

I would like to express my gratitude to Professor Kazunari Domen, Professor Ryoji Kanno, and Associate Professor Nobuo Ishizawa at Tokyo Institute of Technology for their review of this thesis.

This study has also been supported by people not directly related to this study. Dr. Kazuo Nagoshi is one of such people. He often listened to me and gave me good advice. I would like to thank him on this regard.

The heat capacity data up to 420 K were obtained by the adiabatic calorimeter newly constructed in the present study. It was not easy to construct and operate routinely an apparatus, and I often faced various problems. I would like to thank Ms. Yuko Takano for her encouragement and support during the construction of the adiabatic calorimeter.

I would like to express my gratitude to my uncle, Iwao Hayashida. He has taken my father's place and supported my family since my father died in 1986. If there had not been his support and help, I could not have been at my present situation.

Finally, I want to express my greatest gratitude to my mother and younger sister. My mother has constantly supported me and showed an understanding although she has not been in good condition. On the other hand, my sister has supported my family financially because I have not been able to earn enough money to support my family. Without their understanding and support, I could not have accomplished this study. I am really grateful to them.

March 2003